Master of Science

Development of a Predicting System for Calculating Residual Stress and Deformation in 3D Printed Parts

Graduate School of the University of Ulsan

School of Mechanical Engineering

ANSARI MD JONAET

Development of a Predicting System for Calculating Residual Stress and Deformation in 3D Printed Parts

Supervisor: Professor **Lee Chang Myung**

A Thesis

Submitted to

the graduate school of University of Ulsan in

partial fulfillment of the requirements for the

degree of

Master of Science

in Mechanical Engineering

By

Ansari Md Jonaet

School of Mechanical Engineering

University of Ulsan, Ulsan, South Korea.

November 2019

Development of a Predicting System for Calculating Residual Stress and Deformation in 3D Printed Parts

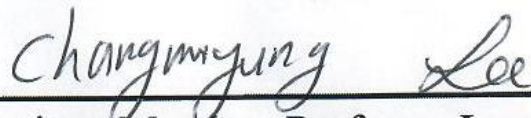This certifies that the Master's thesis of

Ansari Md Jonaet

has been approved by the following committee personnel

_____

Committee Chair, Professor Ocktaeck Lim

_____

Committee Member, Professor Doo-Man Chun

_____

Committee Member, Professor Lee Chang Myung

School of Mechanical Engineering

University of Ulsan, Ulsan, South Korea

November 2019

Acknowledgement

All praise and gratitude belong to the Almighty Allah (SWT). Without His blessings nothing would be possible so far.

I would like to express my sincere thanks and appreciation to my advisor Professor Lee Chang Myung and Professor Hong Seok Park (of School of Mechanical Engineering at University of Ulsan) for their kind guidance, continuous support, supervision and persistent motivation throughout the duration of my graduate study and research. Furthermore, their open-minded attitude towards research, amiability and flexibility also assisted me to broaden the horizon of my thinking and to do creative works without much hindrance. Along with my advisors, I am also very thankful to the thesis committee members: Professor Ocktaeck Lim, Professor Doo-Man Chun for their valuable comments, insightful suggestion and encouragement to improve the quality of my research considering broader prospects.

My following sincere gratefulness goes to University of Ulsan for providing me with a very wonderful environment to pursue my academic study and research. The diverse community of this university also has unlocked a greater scope for me to know, communicate and work with people of different nationalities from all around the world. This will help me to suit myself with different environment either in academic research or in professional career in the upcoming future. Moreover, my heartiest thanks to the course instructors of this university, who not only delivered their lecture in the best way possible but also their direction and crucial discussion on educative contents have imparted me with an insight to think and work efficiently.

Last but not least, my special gratitude goes to my parents, who worked really hard to raise me up and sacrificed a lot in their life to help me achieve everything whatever I have gained so far. Particularly, I am thankful to my mother who worked and is still working as a lifelong mentor and guide for me. Her support, affection and dedication worked as an impetus for me to aim for the best in life and to come this far. I also would like to thank my other family members for their continuous support and blessings.

Ansari Md Jonaet

University of Ulsan

November 2019

Abstract

Selective laser melting (SLM) is an additive manufacturing (AM) technique that has the potential to produce almost any three-dimensional (3D) metallic part, even those with complicated shapes. Throughout the SLM process, the heat transfer characteristics of the metal powder plays a significant role in maintaining the product quality during 3D printing. Furthermore, due to high heating and cooling rates within the selective laser melting (SLM) process, a high-temperature gradient forms in the heat affected zone, which generates significant residual stresses within the fabricated parts. A precise prediction of residual stresses and deformation is essential to ensure dimensional accuracy and prevent premature fatigue failure, delamination and buckling of 3D printed parts. Therefore, it is crucial for 3D-printing manufacturers to determine the thermal and mechanical behavior over the SLM process. However, it is a significant challenge to accurately determine the large temperature gradient, melt pool size, residual stress build up, and deformation using only experiments. Therefore, the use of both experimental investigations and numerical analysis can provide a better pathway in characterizing the temperature gradients and residual stress development in the SLM process in a more effective manner.

The aim of this research is to develop a three-dimensional (3D) thermo-mechanical coupling model to simulate a multi-track multi-layer SLM process utilizing the finite element method for analyzing the thermal behavior, residual stress, and deformation during selective laser melting (SLM) of Ti6Al4V. Moving heat source and temperature dependent material properties were used to the heat transfer model for getting well founded prediction results. In the experiments, a TELOPS FAST-IR (M350) thermal imager was applied to determine the temperature profile of the melting pool and powder bed along the scanning direction during the SLM fabrication using Ti6Al4V powder. Through the simulation, an effective prediction method for investigating the

1

effects of process parameters such as the laser power and scanning speed on the temperature distribution, residual stress, and deformation was established. The numerically calculated results were compared with the experimentally determined temperature distribution. The comparison showed that the calculated peak temperature for single- and multi-track by the developed thermal model was in good agreement with the experiment results. Secondly, the developed model was verified by comparing the melting pool size for various laser powers and scanning speeds with the experimentally measured melting pool size from the published literature. The developed model could predict the melt pool width (with 2–5% error) and melt pool depth (with 5–6% error). The findings showed that the development of residual stress on the fabricated parts gradually increased throughout the SLM process, produced by a heat accumulation effect. Moreover, the model was capable of accurately predicting the trends in deformation for varying the SLM process parameters.

This work demonstrates a unique way to understand the effect of SLM process parameters on the temperature evolution, underlying phenomenon of residual stress development as well as deformation behavior within the SLM process.

Contents

List of Figures

9

List of Tables

Chapter 1

Introduction

This very chapter is focused on illustrating the background, objectives of this thesis, significance and novelty of the research and the organization of this full thesis work.

1.1   Background

Additive manufacturing (AM), widely familiar as 3D printing, is rapidly emerging as a new and disruptive manufacturing technology that offers the opportunity to manufacture complex, freeform three-dimensional (3D) metal parts with a 3D computer-aided design (CAD) design, and an AM printing machine [1]. Currently, AM has received increased attention from the aerospace, automotive, biomedical, and energy industries due to its benefits compared with conventional forming techniques. This technology acts an essential role in Industry 4.0 as the dominant technology that permits the cost-effective realization of the Internet of Things across various industrial applications. In recent years, various alloys such as stainless steel, titanium, aluminum, and nickel-based alloys are preferable for use in additive manufacturing technology [2–5].

Throughout the SLM process, the metal powder is continuously melted and fused by a high-intensity laser beam to fabricate high density, complicated metallic parts from a CAD model [6]. As a result, cross-sections of a certain zone are melted in layers, which are built up continuously to fabricate entire 3D products. Due to its unique process behaviors, SLM can be used to fabricate any intricate and high precision shape for metal parts, including elements with complicated porous shapes, which would be hard to produce with traditional manufacturing technologies [7,8]. Due to the continuous flow of energy through heat transfer in successive layers of the part, large temperature gradients are generated in the fabricated part. Consequently, it is essential to

understand the inherent characteristics related to SLM processes (such as the temperature gradient and the melting pool size) before performing the actual printing process. This is because these characteristics influence the mechanical and physical properties as well as the overall quality of printed products. Moreover, the quality of the final SLM parts significantly depends on the appropriate selection of process parameters including laser power, scan speed, laser spot size, hatch distance, scanning pattern, and layer thickness. For that reason, it is always crucial to find out the optimal process parameters [9]. Yet, the manufacture of structural metal parts utilizing this technology until now has numerous challenges outstanding for both industry and researchers. Critically, the reliable and consistent production of components is yet to determined, which is crucial for acquiring production at bigger sizes. These difficulties rise as of uncertainties in the process, which want additional understanding and justification. A demanding fear is systemic build failure throughout the manufacturing process produced by the build-up of excess residual stresses producing part deformation or failure. This problem enhances large uncertainty to the whole construction process. The build-up of residual stresses is integral to thermal manufacturing processes such as SLM. However, owing to the complicated interactions in the process, experimental measurements offer tiny prospect to realize the thermo-mechanical process that rule the generation of stresses within a complex part. The prediction of residual stress in welding has been long recognized, utilizing analytical and computational models. This indicates that modelling can deliver a vision into the generation of residual stresses in SLM and form a basis of a computational framework for predicting and mitigating residual stresses.

Therefore, it is essential to develop a tool that can determine the temperature profile, melt pool size, residuals stresses and distortion from both industrial and technical perspectives for optimizing the manufacturing processes and to control the consistent quality of the printed products.

12

1.2   Objectives of the research

On this research, we have proposed an effective 3D finite element model of SLM, in order to analyze the thermal behavior, generation of residual stresses, and deformation created within a typical part. The variation of thermal behavior, and the developed melt pool size were investigated by applying various SLM process parameters. Furthermore, the computational model should offer a vision into the mechanisms of residual stress formation across a part and provide guidance for the design of parts and optimize the process parameters. In the end, this would assist to reduce the possibility of part distortion, which is crucial for enlightening the acceptance of SLM by industry. The objectives of this study include the following-

➢ Investigating the computational models for accurately predicting the thermo-mechanical behavior in SLM process.

➢ Development of an efficient computational model to predict the thermo-mechanical behavior of a small part

➢ Utilizing the developed model, carry out a series of studies to understand the effects of the process parameters inputs on the temperature distribution and the developed melt pool size is a multi-track multi-layer pattern during the SLM process.

➢ Utilizing the developed model, carry out a series of studies to understand the effects of the process parameters inputs on the development of residual stresses and distortion with the fabricated parts.

➢ Finally, the corresponding experimental works will perform to validate the predicted results.

1.3   Significance and novelty of the research

The study of the thermo-mechanical behavior in SLM is challenging, owing to the time and length scales involved in this process. Carrying out experiments to examine the thermo-physical phenomena in the process area, and specifically the build-up of residual stresses in the selective laser melting process remnants limited owing to the resolution presented by measurement techniques available, and the resources required.

In this work, a thermo-mechanical finite element model of the selective laser melting process has been demonstrated to accomplish numerical investigations on the temperature distribution and generation of residual stress. This work is significant because it has contributed greater understanding of the mechanisms of thermal behavior and development of residual stresses in SLM. Additionally, the work has investigated the effects of laser process parameters, such as laser power and laser scanning speed on the creation of temperature gradient and residual stresses in macro-scale parts, which was not available in the literature.

In this work, a moving volumetric Goldak heat source was used with consideration of the temperature-dependent material properties and the phase transition of the Ti6Al4V alloy, which will help to explore the optimum processing conditions and parameters to produce high quality parts through the SLM process not previously available.

Furthermore, this work presents a multi-scale method for predicting temperature distribution, residual stress and distortion in macro-scale areas, which may potentially be utilized for industrially sized parts.

1.4   Organization of Thesis

This thesis has been organized according the theoretical investigation and experimental findings conducted by the author. The theoretical representation includes the physical description of heat

transfer mechanism in SLM, thermal modelling, heat source modelling, and the fundamentals of thermal stress analysis to explain everything in a prudent way. Further justification has been made by several SLM experiments. The author has tried to demonstrate that how the SLM process parameters affects the thermal and mechanical behavior during the SLM process. The organization has been made as follows:

- Chapter 1: Introduction

     This chapter introduces the need, purpose and summary of this whole work in brief for proper comprehension of the following chapters.

- Chapter 2: Literature Review Part

     In this chapter, a literature review has been done to recognize the relevant prior investigation in fields associated to powder bed fusion processes, in precise selective laser melting. Initially, background study of additive manufacturing techniques for the fabrication of metal parts is presented, followed by an overview of state-of-art of the selective laser melting process. To date knowledge of thermal behavior, residual stresses, and deformation along with other issues related with the process, and efforts by research to optimize the process have been explained in detail.

     Furthermore, a literature survey of techniques established for modelling the SLM and powder-bed fusion processes has been described. The SLM process is inherently multi-scale and includes the existence of various physical phenomena at the individual scale needed to be expressed by the models. The modelling methods have been divided into the (micro, meso and macro) scales come upon in this process. Finally, analytical methods have been illustrated along with state-of-the-art techniques for upgrading the simulation performance and capability of simulation.

Chapter 3: Thermo-mechanical finite element modelling

In this section, a set of studies has been achieved by means of the thermo-mechanical model established in this work. Firstly, the finite element formulation and the methods for solving systems of equations has been introduced. Then, the thermo-mechanical finite element modelling of selective laser melting has been presented. Finally, the adaptive mesh scheme created in this work has been benchmarked.

Chapter 4: Materials and Experimental Methods

In this section, the experimental methodology that has been used in this research presented in detail. The thermal imager and 3D printer have been introduced at the beginning, followed by the description of the used material, temperature dependent thermal and mechanical properties have been tabulated for reference in the modelling work. The deformation measuring methods are presented at the end.

Chapter 5: Results and Discussion

In this chapter, Analysis of the obtained numerical results have been explained here with logical reasoning and validated with the appropriate experimental findings of the as prepared SLM printed samples.

Chapter 7: Conclusion and future work direction

Outcome of this research has been stated in a nutshell. Moreover, some suggestions have been made based on reasonable assumptions to improve the predicting system of this proposed finite element modelling. In addition, publications and references have been put at the end of this chapter.

Chapter 2

Literature Review

2.1 Additive Manufacturing

2.1.1 What is additive manufacturing?

Additive Manufacturing (AM) is a unit of manufacturing technologies which can fabricate 3D products by combining successive layers of material. Components are produced in an additive manner, layer by layer; and the geometric data can be brought from a CAD model directly [10,11]. The most innovative feature of AM is the capability of quickly fabricating complex geometries without the use of tooling, permitting for more design freedom. The other advantages include the reduction in manufacturing steps and use of materials; therefore, causing reduction in fabricating cost [12].

Additive Manufacturing can return to the late 1980's, early 1990's. In 1991, CIRP's STC-E allocated a first keynote paper on a review of additive manufacturing, which reviews one decade of invention in AM [16]. Although most methods were previously known in 1991, most of them were even in a pre-commercial arena, with several of them achieving the commercialization phase terribly. The first effective procedure, Stereolithography from 3D systems, invented out in 1991. Pursued by other industries, there is a clear revolution in 1994 in AM at which time machinery trades took off exponentially [17]. Nowadays, many AM techniques enable to process materials for instance polymers, metals, ceramics and composites.

2.1.2 Classification

The category of AM technologies can be established on the raw material utilized in the process [18], which divide up these technologies into three distinct types: Liquid-based processes, Powder-based processes and Solid based processes. Fig. 1 presents a family tree of AM technologies. It may not include all recent technologies, but it indicates the classification of most important AM methods.
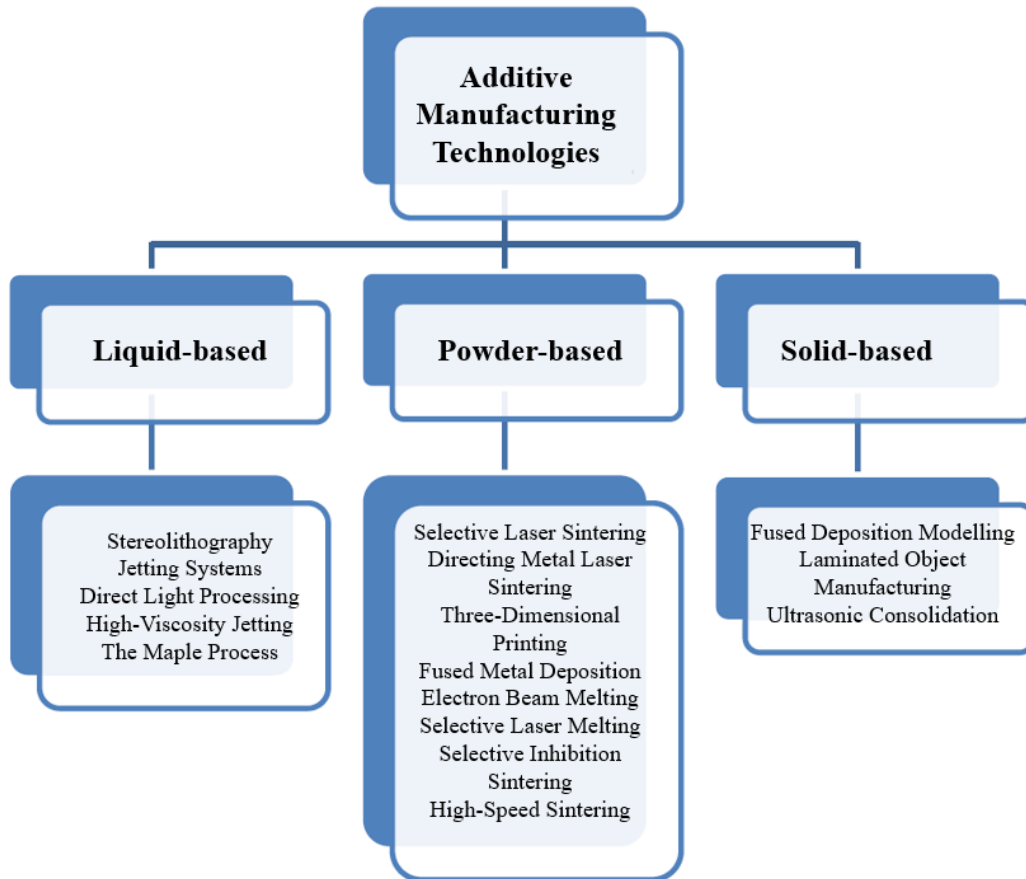
Fig. 1: Family tree of Additive Manufacturing Technologies

2.1.2.1 Powder-based processes

Powder-based additive manufacturing technologies offer a wide range of material possibilities such as polymers, metals and ceramics. Parts can be built with similar material properties and stability compared with solid material. These technologies can be divided into two main types: powder feed deposition and powder bed deposition. Based on powder feed deposition, a few processes have been developed, such as Three-Dimensional Laser Cladding (3D LC) which is also called Laser Engineered Net Shaping (LENS) [22]. In the process, the powder is delivered in a gas jet through nozzles, coaxially with the laser beam. The powder in the melt pool created by the laser can form a cladding line and then cool to form a solid structure when the laser moves away. It is important to melt the powders and homogenize the melt pool for successful building [4]. Fully dense parts can be achieved by this technique. Three-Dimensional Printing (3DP) developed at MIT is the basis of a number of technologies that use the application of a binder to a powder layer to construct parts. In the process, a thin powder layer is selectively bonded by ink-jet droplets of adhesive binder. A range of materials can be used in this technique, including metals. But the parts fabricated by this technique usually have high surface roughness and need further post processing operations to obtain final properties [23,24].

Selective Laser Sintering (SLS) is an important additive manufacturing technique widely used today, which is referred to as powder bed deposition. It was first invented in 1979 by Ross Householder and commercialized in the late 1980s by the University of Texas at Austin, when the first machine came out in 1992 developed by DTM Corporation. The process is in many ways like Stereolithography; but can process a variety of materials including polymers, metals and ceramics. The powdered raw material is sintered or partially melted by a laser which selectively scans the surface of the powder bed to create a two-dimensional solid shape, and then a fresh layer of powder

is added to the top of the bed to form another solid layer which can be traced by the laser bonding it to the layer below. It is basically a one-step process and you can get the final parts directly from a CAD model. To minimize the required laser output energy and to reduce thermal stresses, the powder is normally maintained at an elevated temperature, just below its fusing point. To avoid oxidation problem during the process, it usually operates in an inert protect gas environment [25,26].

Electron Beam Melting (EBM) is a process very similar to SLS but replaces the laser with an electron beam. It was developed by Arcam in Gothenburg Sweden in 1997. The electron beam is stationary and there is no need for scanning mirrors as the beam can be directed by changing an electromagnetic field, which allows for high scanning speed and fast build rates. The technique offers the ability to fully melt a wide range of metal powders due to the high power developed by the electron beam. However, the process is limited to conductive materials and surfaces [27].

Selective Laser Melting (SLM) is also a process very similar to SLS, but it uses a higher energy density to enable full melting of the powder. This technique can build fine details such as thin vertical walls, complex lattice structures and fine cylindrical struts. SLM can process many standard metal materials like Stainless Steel, Inconel, Titanium alloys and Aluminium alloys [1]. Due to the high temperature involved in processing metals, the use of a protecting gas is important to avoid oxidation. It can also enhance the wet ability of the molten material and reduce the porosity caused by oxidation [28]. However, due to full melting process and high temperature, there can be big thermal stresses and large shrinkage after solidification, which need to be improved.

2.1.3 Applications of Additive Manufacturing Technology

The following review is on AM applications in different fields such as aerospace, automobile, biomedical, electrical and other energy fields.

- **Aerospace Industry:** Usually, aerospace components have complex geometries and are made from advanced materials, such as nickel superalloys, titanium alloys, special steels which are costly, time consuming and difficult to manufacture. Most of the industrial applications lie in the production of jet engines, turbine engine cases, engine blades [16].
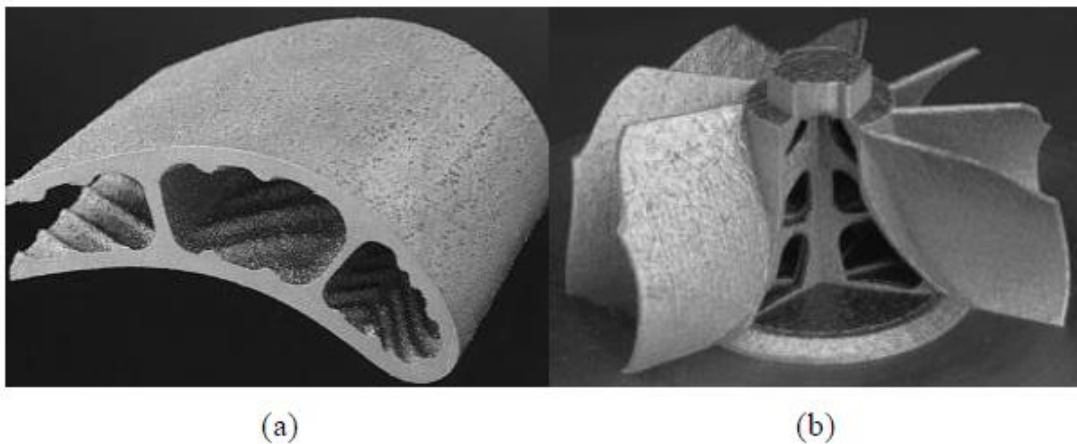
Fig. 2: Aerospace elements manufactured by AM technology [16]: (a) Turbine blade, and (b) Blade integrated.
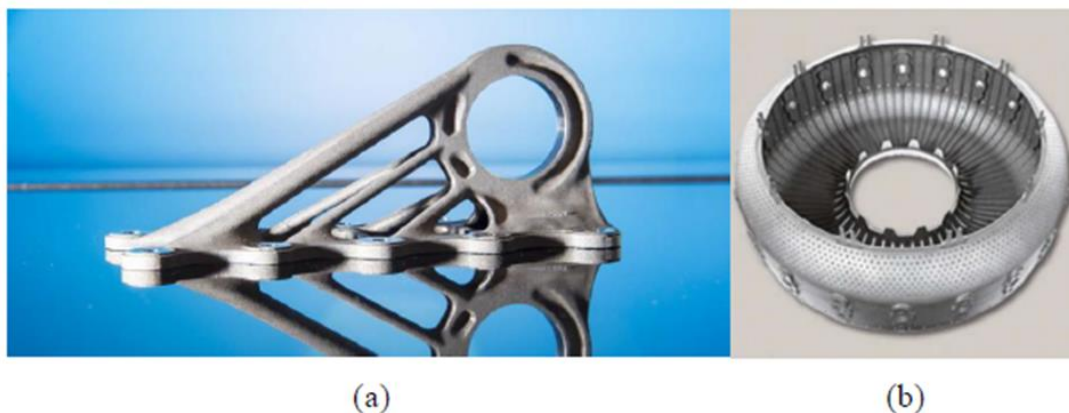
Fig. 3: Aerospace elements manufactured by AM technology: (a) The flight crew rest compartment bracket [17], and (b) Engine housing produced by SLM [29].

21

- **Automotive Industry:** New product developments are critical for the automotive industry and developing new products are often a very costly and time-consuming process. The automotive industry has been using AM technology as an essential tool in the design and development of automotive components and structural and functional parts, such as drive shafts, gearbox components, engine exhausts, pistons, wheels and drive shafts for vehicles [16].

(a)   (b)   (c)
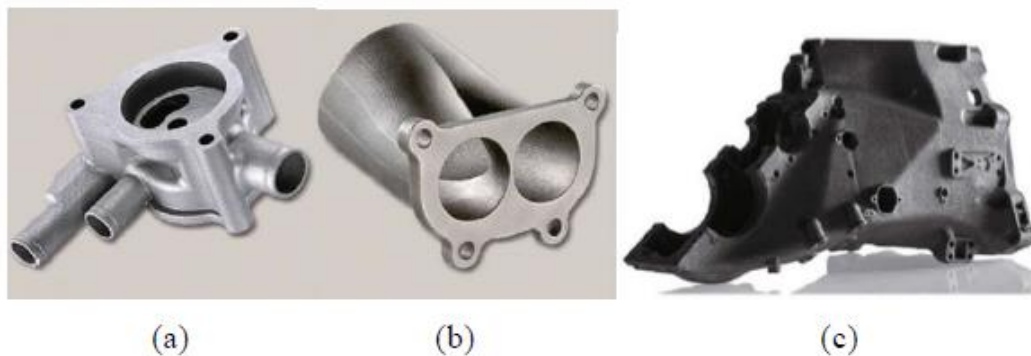
Fig. 4: Automotive elements manufactured by AM technology [16]: (a) Oil pump housing produced by electron beam melting (EBM), (b) Race car gearbox produced by EBM, and (c) Exhaust manifold produced by SLM

.

- **Biomedical Applications:** AM comes as a life-saving process in the medical sector. Recent developments in biomaterials, biomedicine, and biologic sciences have expanded the application of AM techniques in the biomedical field to such products substantially as orthopedic implants, dental applications, artificial organs, tissue scaffolds, medical devices, artificial bladders, bio-printing, painted organs, microvasculature networks and biologic chips [15].

2.1.4 Selective Laser Melting

Selective laser melting (SLM) is one of the new additive manufacturing (AM) techniques that emerged in the late 1980s and 1990s and continuously developing through vigorous in-house and university-based research. A schematic overview of a typical SLM machine and its main components is depicted in Fig. 5. The module consists of a build platform, on which a baseplate is mounted. The baseplate is a plate where the final part will be built upon. The build platform moves down during production, in steps equal to the thickness of one layer. Next to the build platform, a feed container moves upward during processing. The feed container is filled with base powder material and it provides the powder for every new layer. A coater system which can be a roller or a scraper, spreads the powder supplied by the feed container in a thin layer over the baseplate. Then, a laser scans the predefined scan pattern on the powder bed. For the processing of metals, a laser with a wavelength approaching 1064 nm is used, because it has the highest absorptivity for metals.
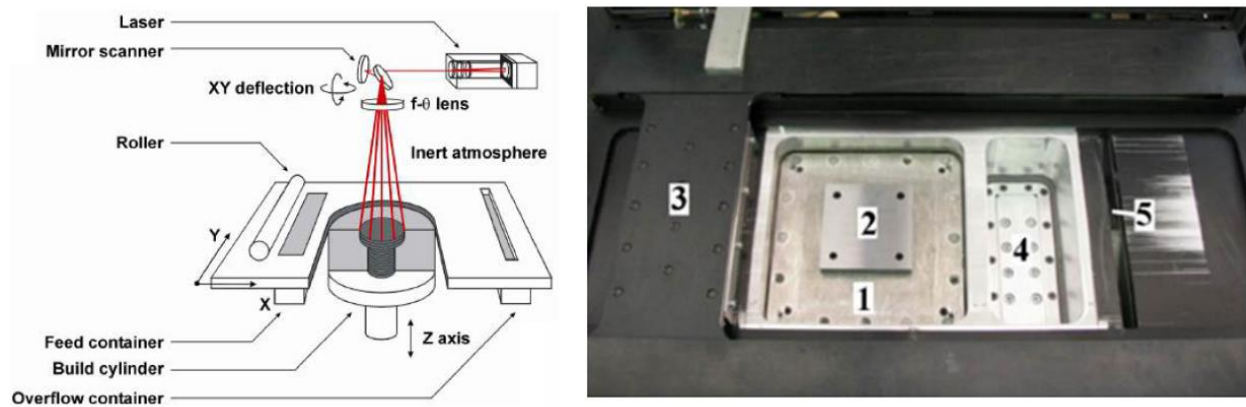
Fig. 5: A schematic overview of the SLM machine and its main components (left). The build module consisting of a build platform (1) with a baseplate (2), a coating system (3) a feed container (4) and an overflow container (5) (right).

The laser beam passes through an f-theta lens, which adjusts the focus of the laser beam, according to the scanning angle theta in order to obtain a horizontal (flat) focus plane coinciding with the powder bed surface. The laser light is deflected onto the powder bed through a galvano scanner which consists of two galvano mirrors for the X- and Y-direction of the laser path. The entire build module operates under a protective atmosphere of Argon or Nitrogen gas, to avoid reactions with the hot solidified melt pool.

The entire Selective Laser Melting process includes the following steps:

1. A 3-dimensional CAD drawing is created. The orientation of the part can be changed for better process conditions or reduced production time, and support structures can be added to enhance the production of downfacing areas.

2. This 3-dimensional model is sliced into 2-dimensional layers with a certain layer thickness. For SLM, this layer thickness generally ranges between 20 and 100 µm.

3. Scan vectors are generated that fill the 2D slices. This defines the path that the laser will follow in each layer. The scan vectors can be generated in different scanning patterns like zigzag, unidirectional, spiral, meander, etc. (Fig. 6).

4. The SLM machine is prepared for production. This includes mounting a baseplate in the build platform, putting powder in the feed container and allocating parameters to the different scan vectors in the machine software.

5. During production, a powder layer is deposited: the feed container moves up, the build platform moves down over the height of one layer and the coater spreads a thin layer of powder on the baseplate.

6. The laser beam is directed across the powder bed, according to the defined scanning pattern and parameters, creating a melt pool on its path. After interaction with the laser beam, the melt pool cools down and the material solidifies.

7. Steps 5. and 6. are repeated until part completion.

8. After complete cooldown to room temperature, the part attached to the baseplate is removed from the machine. The powder is sieved before re-use.

9. The parts are cut from the baseplate typically by Wire Electrical Discharge machining (WEDM).

10. Some post-processing steps might be necessary to meet the dimensional or qualitative requirements. This might include sandblasting, milling or a heat treatment to induce precipitation or eliminate residual stresses.

A great complexity and uniqueness of the process is caused by the laser-metal physical interaction. The final properties of the laser processed material are significantly affected by the laser-metal interaction, while typical processing issues like porosity, balling and residual stresses result from this stage. During SLM, the short interaction of the laser and the powder bed leads to rapid heating and cooling. Most of the laser beam energy is absorbed, while some heat is lost by radiation, convection and evaporation. Surplus, while the melt pool is in the fluid state, the material can interact with the atmosphere, for instance by dissolution of remaining oxygen or nitrogen [30].

Because of the rapid movement of the laser, and the relatively large mass of colder material surrounding the melt pool, the cooling rates are very high, and solidification happens fast. Metallurgically, this leads to metastable phases, a very fine microstructure and thermal stresses.

To avoid these thermal stresses which can lead to the layer curling up, parts in the SLM process are always built on a metal substrate, a baseplate.
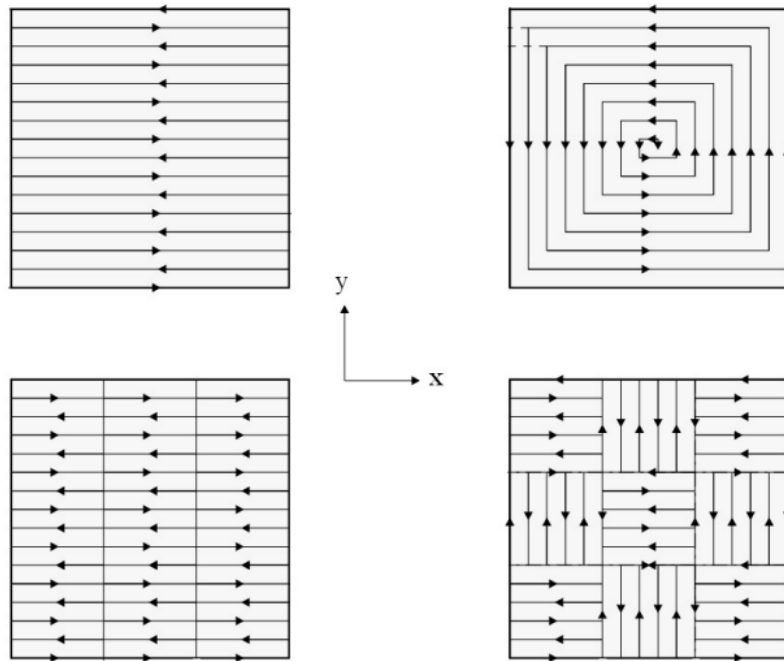
Fig. 6: Different scan strategies that can be applied to fill a 2D surface with scan lines, from left to right, top to bottom: zig-zag scanning; spiral scanning; paintbrush scanning and island scanning [31]

2.1.4.1 Process Parameters

In additive manufacturing technology, many parameters influence the correctness of SLM process (Fig. 7 and Fig. 8). By proper analysis of those parameters, one can understand the occurring mechanisms in an appropriate way to design the process. SLM is a complex process where many parameters can influence the quality of the final part. In SLM, the main process parameters are laser power, laser beam diameter/spot size, scan speed, scanning pattern, hatch spacing, powder

properties, layer thickness and the temperature inside the chamber [32,33]. The various process

parameters in different aspects are as follows:
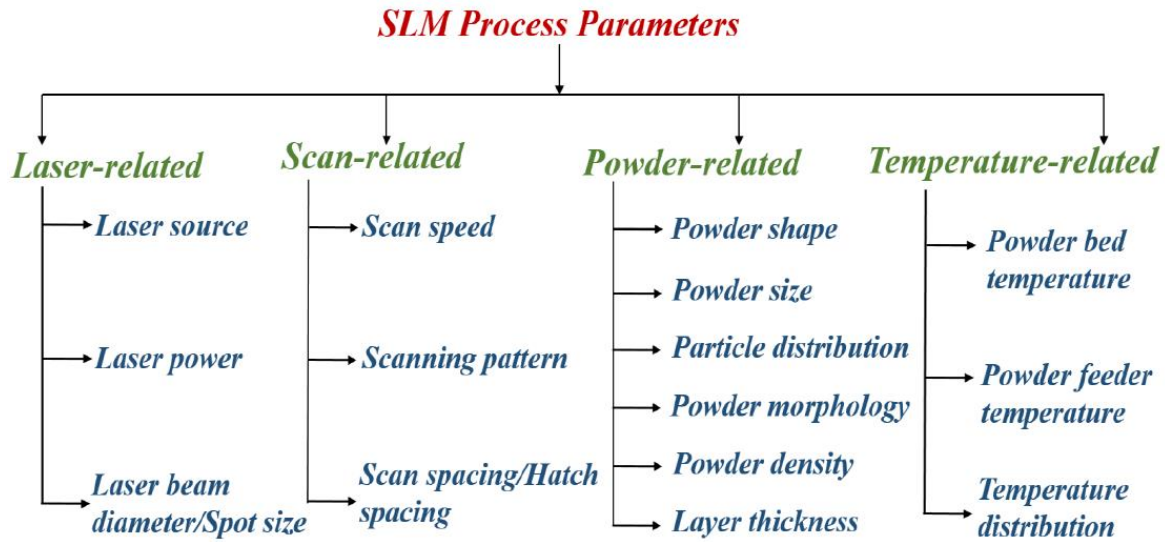
Fig. 7: Process parameters in SLM process.
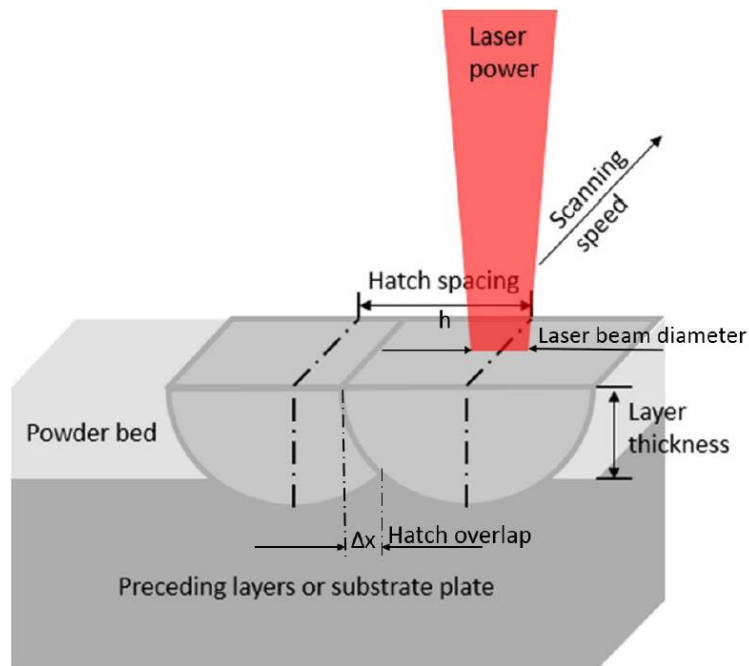
Fig. 8: Schematic diagram of SLM process parameters: laser power, scanning speed, hatch

spacing, and layer thickness.

2.2 Thermo-physical phenomena in the SLM Process

Owing to the nature of powder bed fusion processes such as SLM, a multitude of complex thermo-physical phenomena occur at a variety of different spatial and temporal time scales. Within this section, a review of the literature which analyses and discusses the underlying physics present during the manufacturing process using experiments and numerical simulations is reported.

2.2.1 Laser interaction with the powder bed

During the SLM process, the powder bed is irradiated by a laser focused onto the powder bed. Absorption of photons on the surface of the powder causes a transformation into thermal energy. Typical focused laser spot diameters range from 25 - 100 µm with a layer thickness varying between 25 - 50 µm depending on the powder morphology and the build material [29]. Two different types of irradiation sources are conventionally used for SLM: CO_2 and neodymium-doped yttrium aluminum garnet (Nd:YAG) with respective wavelengths of 10.6 µm and 1064 nm. The choice of laser depends on the absorptivity of the material, driven by the absorption mechanism [39]. Insulating materials, such as polymers, ceramics, and metal oxides, tend to favor the use of CO_2 lasers, whereas absorption with the Nd:YAG is better with metals, as shown in Table 1.

Table 1: Absorption of wavelengths of a selection of materials taken from experiments
performed by Tolochko et al. [39]

Materials	Absorption A	
	$\lambda= 1064$ nm (Nd:YAG)	$\lambda= 10.6$ μm (CO_2)
Cu	0.59	0.26
Fe	0.64	0.45
Sn	0.66	0.23
Ti6Al4V	0.77	0.59
Al_2O_3	0.03	0.96
SiO_2	0.04	0.96
NaCl	0.17	0.60
PTEF	0.05	0.73

2.2.2 Thermo-fluid physics

Upon the formation of a melt pool, the high thermal gradients and energy input create a highly
complex set of thermo- fluid physical phenomena, providing a great challenge for researchers to
identify and understand. The melt pool is subject to a variety of forces acting upon it including
buoyancy, gravity, surface tension and capillary forces. The fluid flow in the melt pool is largely
dominated by surface tension effects, rather than buoyancy and gravity.

The surface tension has a significant influence on the formation of the melt pool. The high surface
tension and wettability of molten metals facilitate the formation of smooth surfaces under
favorable conditions, permitting the creation of continuous elongated cylindrical tracks, as shown

29

in Fig. 9. Yadroitsev et al. showed experimentally that elongated melt pools with high aspect ratios were susceptible to instability, due to capillary forces [42].
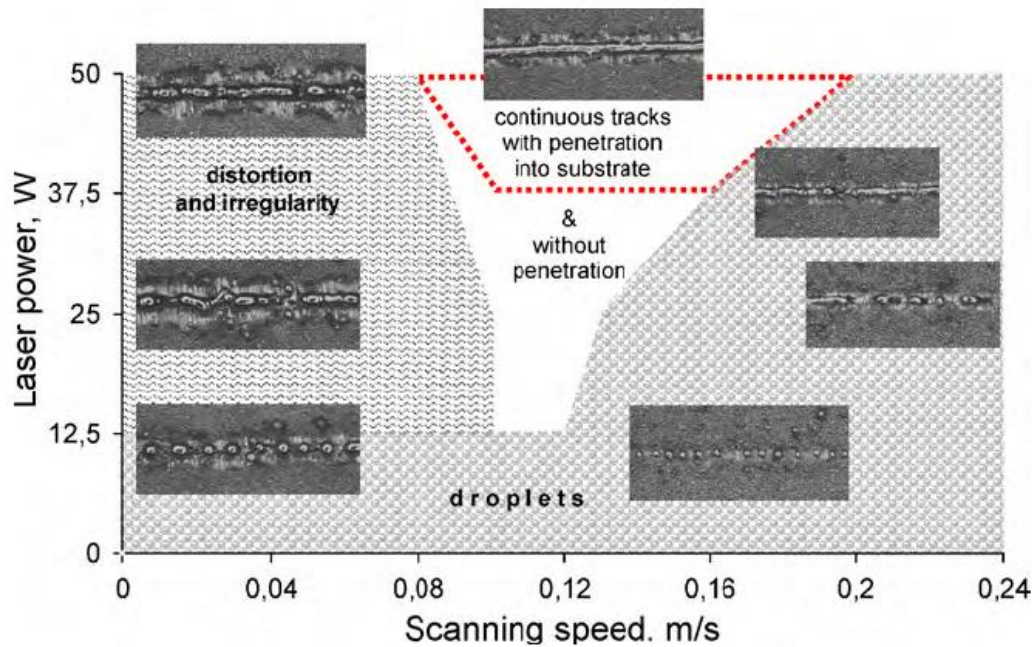
Fig. 9: Single track process map of Stainless Steel 316L with a layer thickness of 50 µm taken from a study performed by Yadroitsev and Gusarov [42].

Understanding the previous behaviour would further explain the balling phenomenon discussed by Gusarov et al. [43]. Fundamentally, surface tension drives the melt pool to minimise the surface energy towards its lowest energy state - a sphere. During this deformation, the track melt pool begins to recede from the substrate, as shown in Fig. 10.
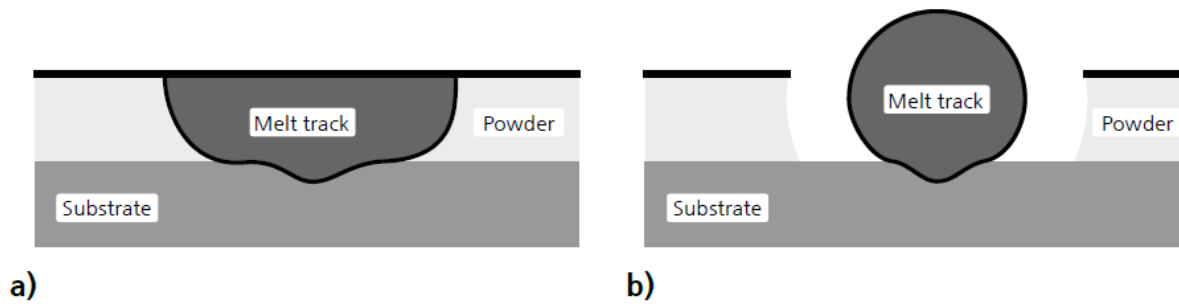
Fig. 10: Illustration showing the role of surface tension affecting the track geometry upon consolidation when a) just melted and b) after minimizing the surface energy of the melt track surface.

The balling effect occurs with high aspect ratio melt pool geometry; i.e. the melt pool becomes larger than equivalent sphere of the same volume, which is observed typically with high aspect ratio melt pools. Tolocko et al. investigated the mechanisms for the balling effect, and showed this instability is dependent on the laser parameters chosen. The balling affect can be avoided by limiting excess power into the powder and controlling the laser scan speeds to ensure a stable melt pool shape is achieved [44]. A study by Yadroitsev and Gusarov intuitively found the penetration into the substrate was linearly dependent on the scanning velocity, therefore the contact angle and aspect ratio of the melt pool could be controlled [42]. Their investigation resulted in a process map shown in Fig. 9, and it was highlighted that re-melting of the substrate was crucial for obtaining stability during the process. Instability at higher powers was attributed to fluidic effects created by Marangoni flow, and the key-hole phenomena both further discussed in Sections 2.2.3 and 2.2.4.

2.2.3 The effects of Marangoni flow

The second consequence of surface tension forces are within the melt pool itself, namely surface tension driven Marangoni convectional flow. Marangoni flow is induced by a shear force τ acting parallel to the melt pool's free surface, created by a surface tension gradient $\partial \gamma / dT$ induced by the temperature gradient. Marangoni forces dominate the flow in the melt pool and have a strong effect on the melt pool dimensions and surface temperature depending on the flow direction and magnitude of the convection. The shear force may be derived using the chain rule assuming a radial coordinate system around the melt pool centre [45],

$$\tau = -\mu \frac{\partial u}{\partial z} = -\mu \frac{\partial \gamma}{\partial T} \frac{\partial T}{\partial r} \tag{1}$$

where μ is the dynamic viscosity of the molten metal. Characteristic melt pool shapes as a result of Marangoni flow are shown in Fig. 11. A negative surface tension gradient $(\partial \gamma / dT < 0)$ results in a shallow melt pool and a positive surface tension gradient $(\partial \gamma / dT > 0)$ results in narrow deeper melt pool with.

a)　　$\partial \gamma / \partial T < 0$　　b)　　$\partial \gamma / \partial T > 0$
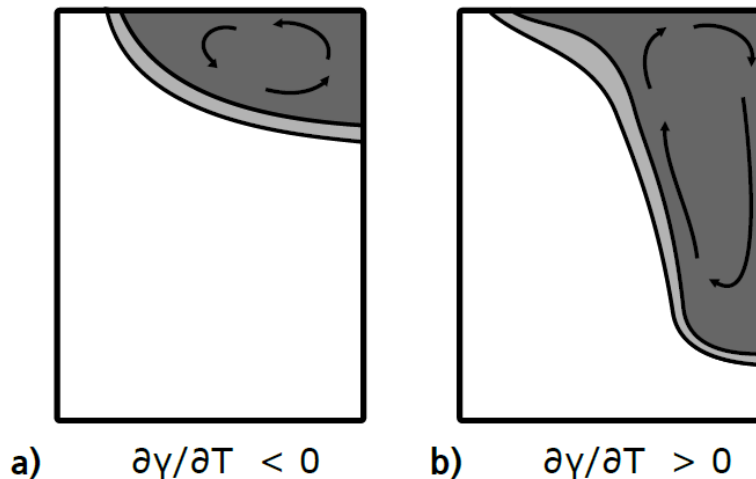
Fig. 11: Illustration showing the effect of the surface tension gradient on the shape of the melt pool: a) a negative gradient forms a shallow profile and b) a positive gradient produces a narrow deep depression.

2.2.3 Identifying the process window

Careful choice of laser power, point exposure time and point distance effectively control the rate of consolidation (build speed), part density, and together directly impact on build quality. Typically, process optimization begins with the stable formation of single tracks and thin walls [42]. Accomplishing this across a parameter space, produces process maps, as illustrated in Fig. 12.
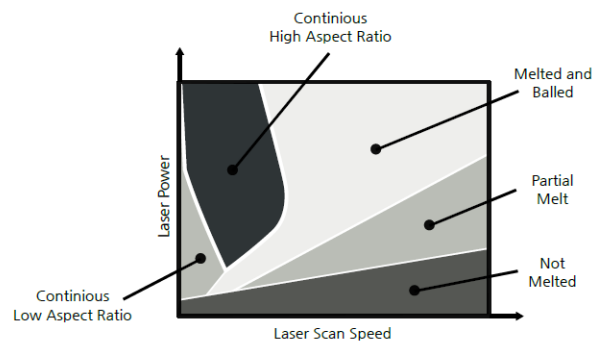
Fig. 12: Process map of a tool steel experiment adapted from [50].

These are created through experimental methods, as shown in Fig. 13, to identify a satisfactory operating window [50].
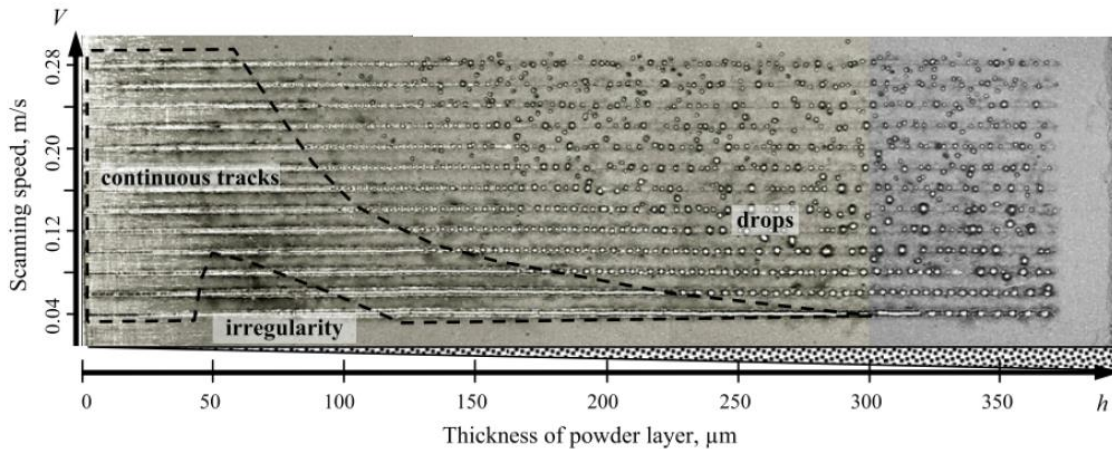
Fig. 13: Process map performed by Yadroitsev et al. [50] showing melt pool formation and stability of a single track with varying scan speed and layer thickness.

These process maps provide a guide to identify parameters where there is stable formation of the melt pool, and its solidification forms stable continuous tracks with low aspect ratios. Typical experimental methods are exhaustive trial and error approaches, since the parameter space is large, and this further reduces the understanding of process.

The optimal laser parameters are highly dependent on the material, the powder morphology and the capabilities of the machine, which are currently problematic for standardization and certification of the process. Therefore, care must be taken when comparing research owing to the difference in known stated parameters and those unknown within the sub-process.

2.3 Temperature Distribution and Melt pool formation in the SLM Process

2.3.1 Influence of Process parameters

In an SLM process, a very steep temperature gradient is generated due to the rapid heating of the upper surface by laser and slow heat conduction of underlying layers. Many works, either through experiment or simulation, have been done to investigate the relationship between the different process parameters and the temperature distribution and melt pool size the SLM process. A relatively low laser power results in increased voids and about 50% decrease in the material strength for stainless steel 316 L [51], while high laser power increases the warping trend for overhanging surface [52]. A relatively lower scanning speed will improve the surface quality of a single layer while higher scanning speed will improve the surface quality of multi-layers [53]. Extensive modeling effort has gone into the formation of the melt pool, and the temperature field around it [9,54–60]. Increasing the scan speed elongates the melt pool and lowers the maximum temperature of the melt. Increasing the laser power causes the melt pool size to grow and increases

the maximum temperature [9,54–60] . The experimentally measured temperature distribution along a line from the center of the melt pool towards its tail in Fig. 14 shows a plateau at the tail where solidification takes place, both for SLM [56]. Furthermore, Yadroitse et al. also reported that laser power has a more pronounced effect on the maximum temperature than exposure time. Lowering the laser power reduces the maximum temperature of a melt pool and leads to a smaller melt pool, which results in higher cooling rates [56].

Most models show the melt pool as a hot zone on a flat FE model, where the individual elements are given properties based on the type of material they represent (powder, solid or liquid). Evaporation is often not considered. It has been considered, together with numerous other effects such as melt flow and individual powder particles, in the work performed at Lawrence Livermore National Laboratory (LLNL) [55]. This extremely detailed model, of which a resulting side-view cross section of the melt pool is shown in Fig. 15, shows that the laser penetrates deeply into the material, almost forming a keyhole weld type melt pool. The melt is pushed back by the recoil pressure due to evaporation, and surface tension causes the melt bead to rise above the level of the
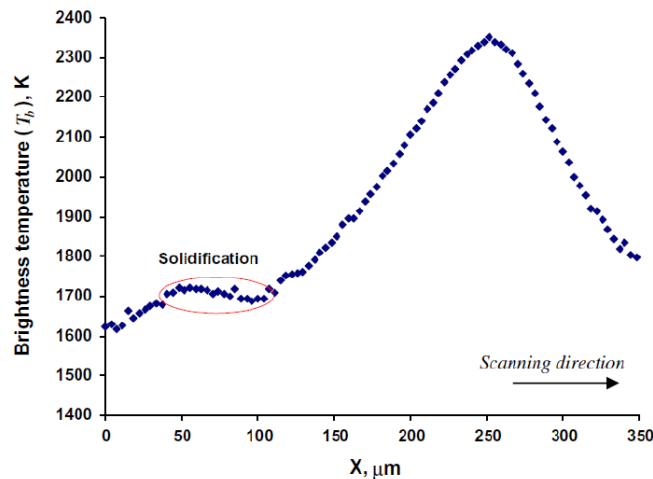
Fig. 14: Experimentally measured temperature distribution along the central line spanning from behind the tail of the melt pool (X=0) towards just in front of the melt pool (X=350). A plateau in temperature near the tail indicates the zone in which solidification takes place [56]).

35

layer below. The model was detailed enough to show the effect of individual powder particles being drawn into the melt pool and the instabilities this created.
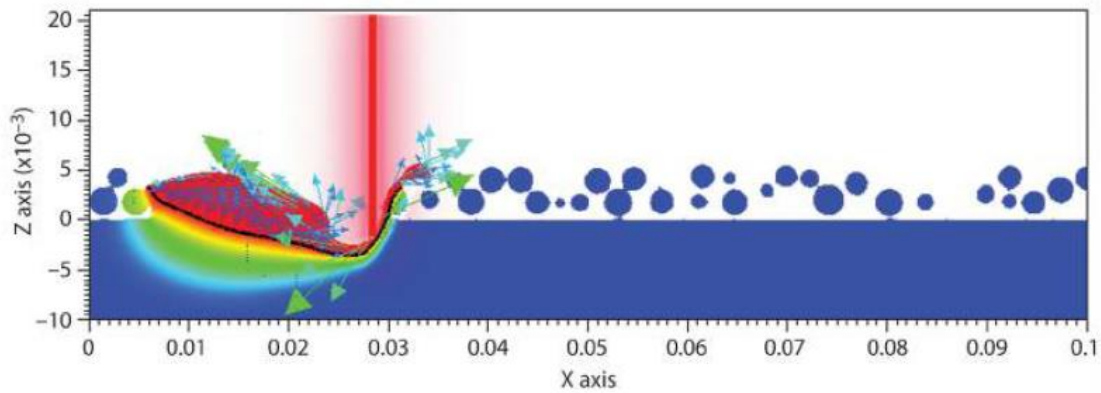
Fig. 15: Realistic modeling of the melt pool shape, melt flow and formation of the scan track [55].

2.4 Residual stress in selective laser melting

Probably the most significant concern to industry in the use of SLM for structural parts is the ability to predict and mitigate the residual stresses generated in parts during manufacture. These are the primary cause of build failure, and indirectly, they impose severe design restrictions and reduce the reliability of components, driving up costs, which impede the adoption of SLM in industry.

2.4.1 Mechanisms for the generation of residual stress

Laser based manufacturing processes are extremely susceptible to the generation of residual stresses owing to the highly localised heating. The primary mechanism for the creation of residual stress is the temperature gradient mechanism (TGM) [59]. As shown in Fig. 16, when laser beam hits the top surface, the expansion of the heated layer is restricted by the surrounding area; therefore, a compressive stress is generated on the top surface. When the yield stress of the material
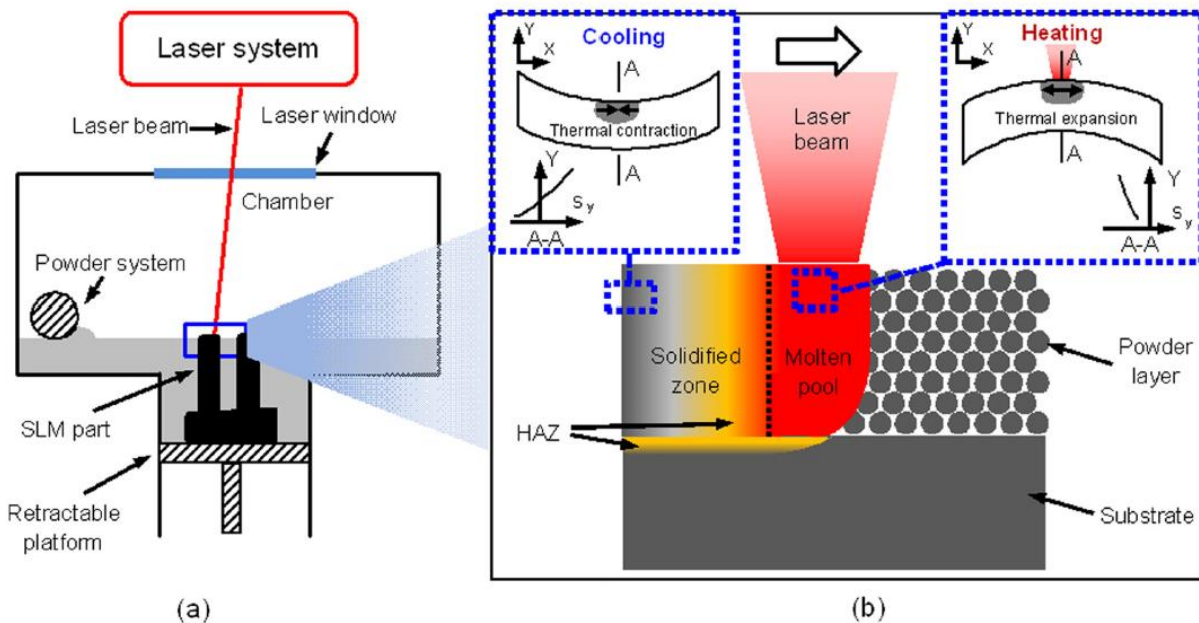
Fig. 16: (a) SLM experimental setup and (b) process principle

is reached, plastic distortion occurs. As the laser moves away, cooling takes place; the contraction of the top layer is then restricted by the surrounding area, leading to a tensile residual stress on the top surface. The tensile residual stress will accumulate during each laser scan, which can cause delamination or cracks. Also, the cooling and shrinkage will create shorter top layers than the bottom layers; thus, the component is distorted by bending toward the laser beam.

In details, according to the temperature gradient mechanism [59], a compressive stress strain condition builds up in the irradiated material due to partial inhibition of the thermal expansion (εth) of irradiated material by surrounding colder material as shown in Fig. 17 left (a). Partially elastic (εel) and partially plastic (εpl) compressive strain will occur in the irradiated zone if the compressive stress is greater than the compressive yield stress ($\sigma yield$) as shown in Fig. left 17 (b). During cooling, plastic deformation (εpl) partially inhibits the shrinkage of the material in the irradiated zone resulting in the buildup of residual tensile stress ($\sigma tens$) in the irradiated region as shown in Fig. 17 right (a). Force and momentum balance in the part results in the buildup of

compressive residual stress ($\sigma comp$) in the region surrounding the irradiated zone as shown in Fig. 17 right (b).
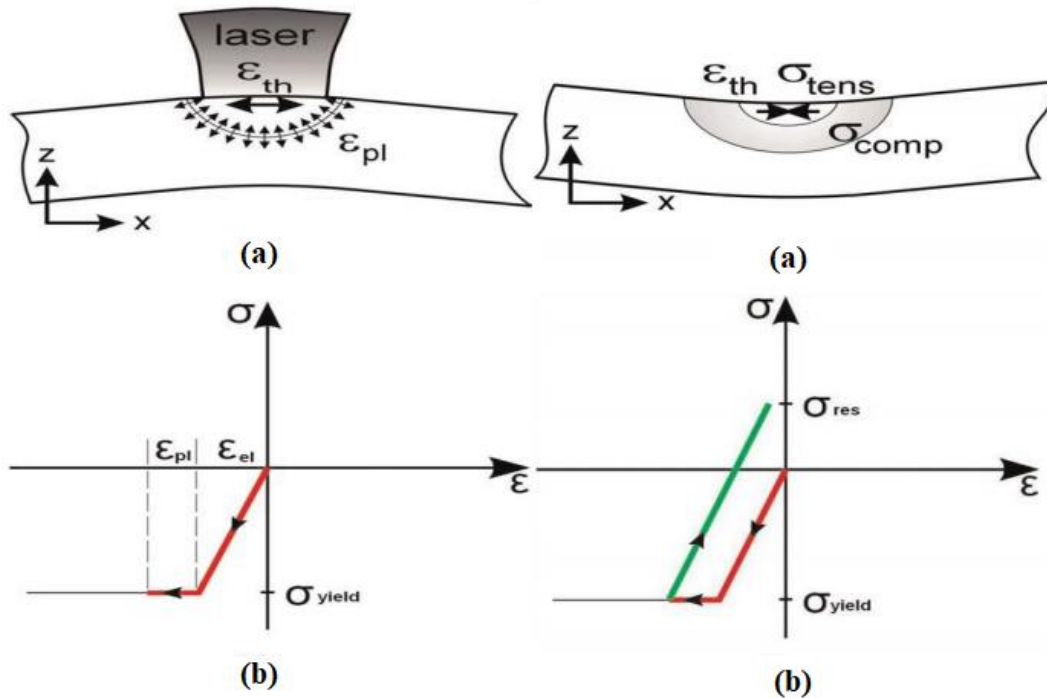
Fig. 17: Left (a) Induced stresses and deformation (strain) during laser beam heating. (b) Simplified representation of the formation of thermal stress and strains in the irradiated zone [59].
Fig. 17: Right (a) Occurring stresses and deformation (strain) when the part cools down. (b) Simplified representation of the formation of residual stresses and strain in the irradiated zone [59].

2.4.2 Consequences of residual stress in SLM

Residual stresses unmanaged, have the immediate consequence of causing failure during manufacture, as shown in Fig. 18. Unlike laser sintering and to some extent EBM systems, parts produced by SLM require additional support structures to prevent build failure. Support structures constrain the part to restrict `curling' or distortion during the build to prevent collisions with the

powder re-coating mechanism. In extreme cases, high residual stresses cause the material to fail and rupture, allowing the part to freely deform and again collide with the re-coating mechanism.
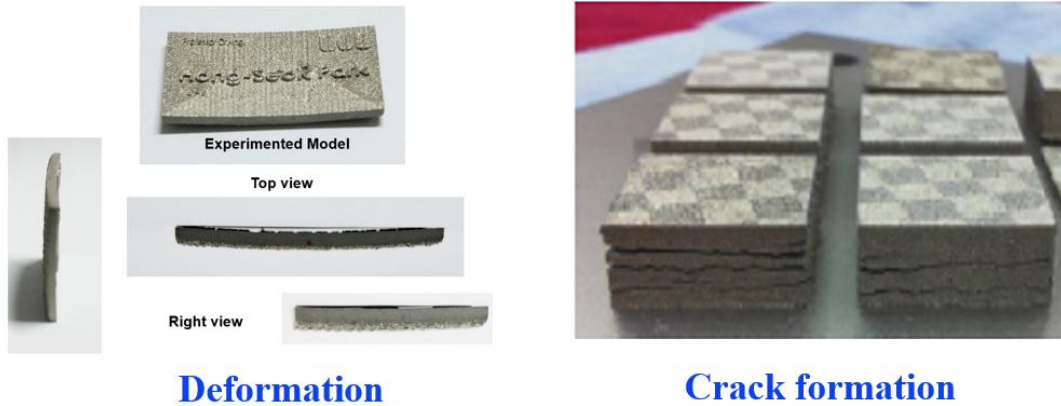
Fig. 18: Deformation and crack formation during manufacturing of a Ti-6Al-4V component caused by the build-up of residual stress.

2.4.3 Influence of process parameters

The scan speed and laser power, and by extension the layer thickness and hatch spacing, cannot be varied independently, as a high final part density always needs to be achieved. It is therefore difficult to distinguish the influence of the individual process parameters on the development of residual stresses during the process. One solution is the use of thermomechanical models that neglect the influence of the parameters on the formation of a stable melt pool but are none the less detailed enough to allow variation of the process parameters. Another is to explore the limits of the experimental process window to find upper and lower values for the parameters to compare. The list below summarizes the influence of the scan speed, laser power, hatch spacing and layer thickness, as reported in literature.

- **Scan speed:** Lowering the scan speed reduces the residual stresses in the one track model [61]. It also reduced deformation of bridge shaped specimens [62]. Reducing scan speed

leads to lower temperature gradients [63], lower cooling rates [64], lower residual stresses and reduced deformation, while higher scan speeds produce increased cooling rate and leads to increased cracking [61]. These are all similar conclusions.

- **Laser power:** First consequence of lowering the laser power is that the maximum temperature of the melt pool is reduced and this also reduces the melt pool size but increases the cooling rates [64]. Like a lower scan speed, a higher laser power lowers the deformation [65]. High laser power results in lower deformation due to residual stress [65], while Alimardani et al. [66] reported lower residual stresses for lower laser power.

- **Hatch spacing:** In Ref. [67], the deflection of a steel sheet, onto which a couple of layers of pure iron were sintered measuring 60mm by 14mm, was measured. The laser passed over the powder in the long direction. Increasing the hatch spacing from 100μm to 300μm reduced the deflection by more than half. The author associated this to more localized heating if lower hatch spacings were used, creating larger temperature gradients and thus larger deflections. The study failed to consider that tripling the hatch spacing also greatly reduces the number of tracks that are deposited, and no mention was made of the densities of the sintered layers. The influence of the hatch spacing is therefore not known.

- **Layer thickness:** The deformation of bridge shaped specimens [68], thin plates onto which layers were deposited [69] and cantilever specimens [70] were all reduced by increasing the layer thickness, all citing decreased cooling rates due to the increased energy input when working with thicker layers.

Furthermore, a parametric experimental study was performed by Vrancken to study the effect of laser speed, laser power, and layer thickness on the residual stress generated using X-ray diffraction (XRD) measurements [71]. Their results indicated that an increase in the layer thickness increased residual stress and was attributed to less thermal accumulation using larger layer thicknesses.

2.5 State-of-art overview of Thermo-mechanical modelling of selective laser melting

The transient temperature history of powder bed and solidified layers is crucial for calculating the thermal stress distribution and final residual stress in the built part. For weak coupled thermo-mechanical finite element analysis, after the temperature history has been obtained, a transient stress analysis will be executed. The obtained temperature history is applied as the thermal load for the mechanical analysis. Followed the above-mentioned method in section 2, many FE models have been developed to estimate the temperature field and thermal stress field during the PBF process. Shuai et al. presented a mathematical model and established an FE method for determining the dynamic temperature distributions during the SLS process [72]. Song et al. performed a numerical analysis to predict the temperature field as well as experimental work to determine the relationship between the density, porosity, and laser scanning speed to identify better process parameters for the SLM process [4]. Fischer et al. conducted an experimental investigation to measure the peak temperature for the continuous wave and pulsed sintering process using an infrared camera [73]. Dai and Shaw presented an FE model to determine the effect of volume shrinkage associated with phase change during laser forming, and experimental work was performed to verify the presented model [74]. Yadroitsev et al. used a CCD camera for determining the highest temperature and the melt pool size of Ti6Al4V and also investigated the microstructure

41

of SLM printed parts [13]. Huang et al. provided a detailed model of the temperature distribution and melt pool size that considered the volume shrinkage and linear energy density; this model was verified by comparing with published experimental results [8]. Dilip et al. experimentally measured the melt pool size and identified the relationship between porosity and energy density by changing the SLM process parameters [3]. Lee and Zhang presented a model of the macroscopic fluid and heat transfer incorporating Marangoni effects. They observed that Marangoni convection dramatically influenced the thermal behavior in the developed melt pool at the time of the SLM process [14]. Ali et al. presented a model that can predict the temperature distribution, melt pool width (with 14.5% error), melt pool depth (with 3% error), and the developed residual stress within the fabricated parts for various SLM process parameters [15]. Hwang et al. introduced a discrete element method to analyze the melting pool behavior of a randomly distributed powder bed with keyhole formation during SLM process [16]. Erdam et al. developed a finite element-based multi physics and multi-software platform thermal model which can predict the transient temperature and the molt pool geometry in the laser additive manufacturing process [17]. Ehsan et al. presented a FE model to predict the melt pool size during the SLM process and findings revealed that the melting pool size differs from the start of the track to its end [18]. Yang et al. applied DOE-FEM and RSM method to predict the time evolution of temperature field and the sizes of the melt pool of Ti6Al4v alloy during SLM process [19]. Yali and Dongdong performed numerical investigation to reveal the effect of laser power and scanning speed on the thermal behavior during the SLM process [20]. Ma and Bin [20] proposed an FE analysis to determine the effect of two different laser moving strategies on the temperature distribution, residual stresses, and deformation during the selective laser sintering (SLS) process. Hussein et al. developed an FE model that employed thermo-mechanical analysis for evaluating the development of temperature fields, melt pool size,

42

and residual stress at various points on a single layer fabricated by the SLM process [56]. Ali et al. analyzed the influence of layer thickness on the thermal stress and mechanical properties of the SLM process for Ti6Al4V products by changing the applied laser power [75]. Zhonghua et al. applied a FE analysis model based on coupled thermal-structural analysis to predict the variations of temperature, residual stress and deformation by using various scan lengths for thin-walled parts in the SLM process [76]. Parry et al. established a coupled thermo-mechanical model which capable to predict the developed residual stress within the SLM manufactured part by utilizing two different scanning patterns for single layer [77]. Fu and Guo developed a 3D FEM to simulate multilayer deposition of Ti-6Al-4V in SLM. The modeling process incorporates the layer accumulation approach and the moving heat source [59]. Childs et al. investigated the influence of laser power and scanning speed on the scanning track in the powder bed and found a proportional relationship between scanning speed and the mass of melted metal [28]. Bugeda and lombera developed a FEM to simulate the 3D sintering process of a single track during SLS process. The coupled model obtains useful results such as the temperature field, solid fraction and density distribution, and sintering depth [78]. Gusarov et al. proposed a model which combined the heat radiation to stabilize the SLM process to study a single track on a layer of the loose powder bed. The results show that the maximum temperature is slightly shifted away from the center of the laser beam and the melt pool is highly stretched along the scanning direction [54]. Denlinger et al. model the insitu thermo-mechanical stress and distortion of a Ti-6Al-4V part by a 3D thermal-elasto-plastic analysis. The simulation results show that the computed thermal history and computed distortion history displays 7.7% and 7.4% error with the measurement from experiment respectively [79]. Zaeh and Branner presented a model to simulate the transient physical effects in AM and identifies the heat impact on residual stress and deformations through a coupled thermo-

mechanical model [70]. Vasinonta et al.presented a thermo-mechanical model which involving a moving heat source to build thin-walled structures [63]. Jiang et al. presented a thermo-mechanical model to investigate the residual stress and deformation in direct laser sintering of stainless steel. The thermal model considers the nonlinear heat conduction with a moving Gaussian heat source and latent heat and temperature-dependent material properties [80].

From the review of existing studies, FE analysis of temperature distribution during SLM process is the most widely studied. In addition, the investigation of residual stress and deformation in final part usually does not include the fluid dynamic of melt pool because of the small size of melt pool compared to that of the part being built and complicated phenomena happened in melt pool. Therefore, the simulation of temperature and thermal stress fields are also only limited to single track, one layer, or several layers due to the limitation of computational cost.

2.6 Summary of literature and identified gaps in the literature

In order to understand the factors affecting temperature distribution, melt pool size and residual stress and its prediction requires the creation of a thermo-mechanical model. Coupled thermo-mechanical analyses of SLM have been reported by several researchers, as discussed in Section 2.5, yet the underlying mechanisms for the generation of temperature distribution and residual stress remain less understood. Most of the developed thermo-mechanical models of SLM in the literature tend to be line based (either single tracks or thin walls).

Following the literature review into numerical approaches of modelling SLM, the identified gaps in research are outlined below:

1. The micro-scale behaviour is experimentally very difficult to capture due to the random nature of powder, and the complex thermo-physical phenomena at this scale. Therefore,

highly detailed micro-models, require very high spatial and time resolution, which is computationally very expensive. As a result, this area of modelling remains challenging.

2. Understanding of the development of temperature distribution and build-up of residual stress is limited by the performance and resolution of thermo-mechanical models. Suitable strategies have been suggested but have not reported any meaningful results with respect to the temperature distribution, residual stress and deformation.

3. There is interest towards developing multi-scale methods to couple the analysis scales together from different simulation types, especially for part scale prediction of residual stress and distortion. These strategies remain undeveloped and their underlying assumptions require further investigation

Chapter 3

Thermo-Mechanical Finite Element Modelling

The general flow chart for the modeling of temperature and thermal stress fields has been shown in Fig. 19. The major steps in the FE formulation and analysis of a typical problem include pre-processing, processing (thermal analysis and mechanical analysis), and post-processing. Next, the main procedures and techniques used in this figure will be explained in detail.
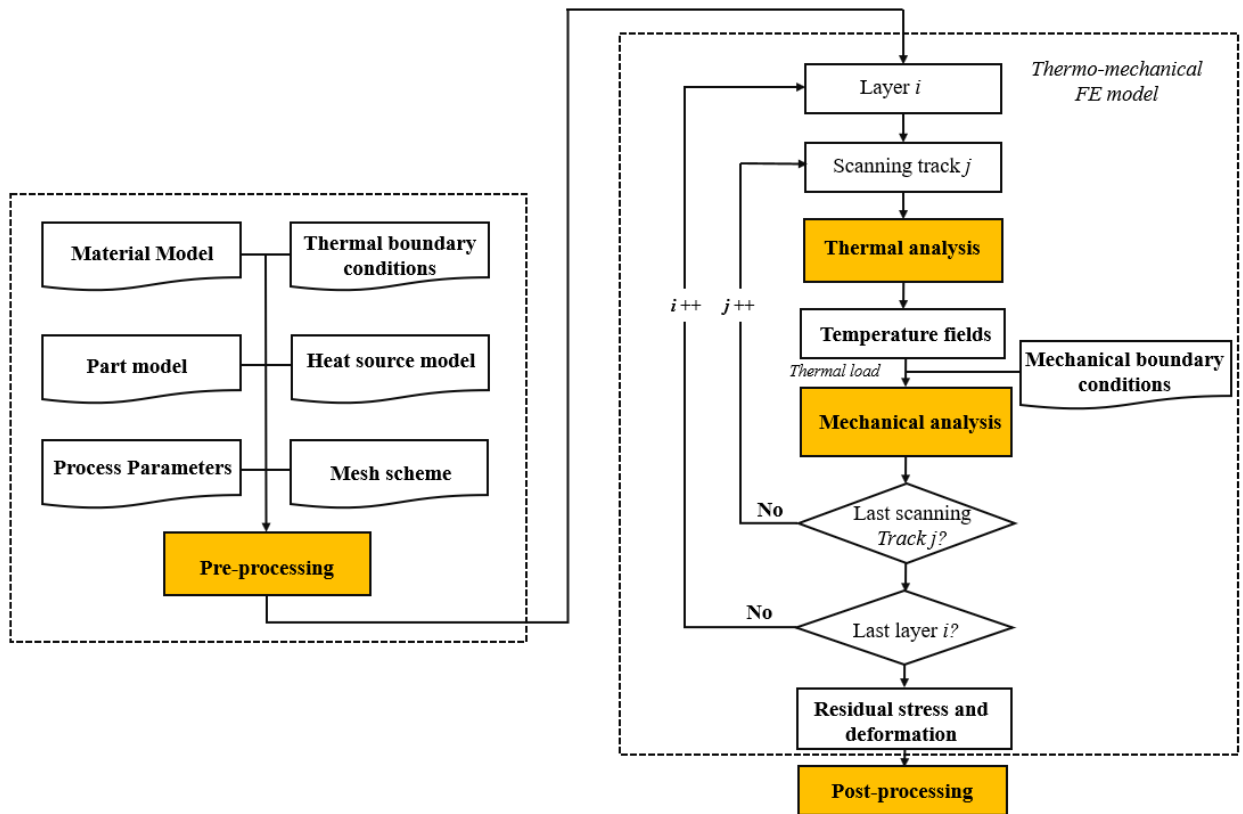
Fig. 19: Flowchart of thermo-mechanical FE model.

3.1 Pre-processing

3.1.1 Part Geometry

Geometric model of a part defines the domain for the generation of finite element (FE) mesh and the subsequent FE analysis. The basic idea of the FE mesh is to view a given domain as an assemblage of simple finite elements such as triangular element and rectangular element in 2D or tetrahedral elements and hexahedral element in 3D. In this work, A 3D thermal analysis model was developed using COMSOL Multiphysics Modeling Software (Version 5.4, COMSOL Ltd., Cambridge, UK) to predict the global temperature fields, melt pool size, residual stress and deformation.

The 3D numerical model, mesh structure, and the SLM scanning patterns are shown in Fig. 20. The dimensions of the modeled powder bed were a length of 20 mm, a width of 10 mm, and a thickness of 0.1 mm. To acquire the finest calculating efficiency within the smallest computational time, an extremely fine mesh was used for the powder bed, while a comparatively fine mesh has been used for the substrate. The numerical model consists of 211689 total domain elements, 96262 boundary elements, and 1204 edge elements. The total computational time required for this presented simulation is about 15-16 hours when using a workstation with an Intel Xeon CPU E5-2620 v2 @2.10GHz, RAM 32 GB (Intel, Santa Clara, USA). The heat source moved in a bidirectional scanning direction. The entire Ti6Al4V powder bed was presumed as a continuous and homogenous ambience. The coefficient of convective heat transfer among the powder bed and the circumstances were presumed to be a constant.
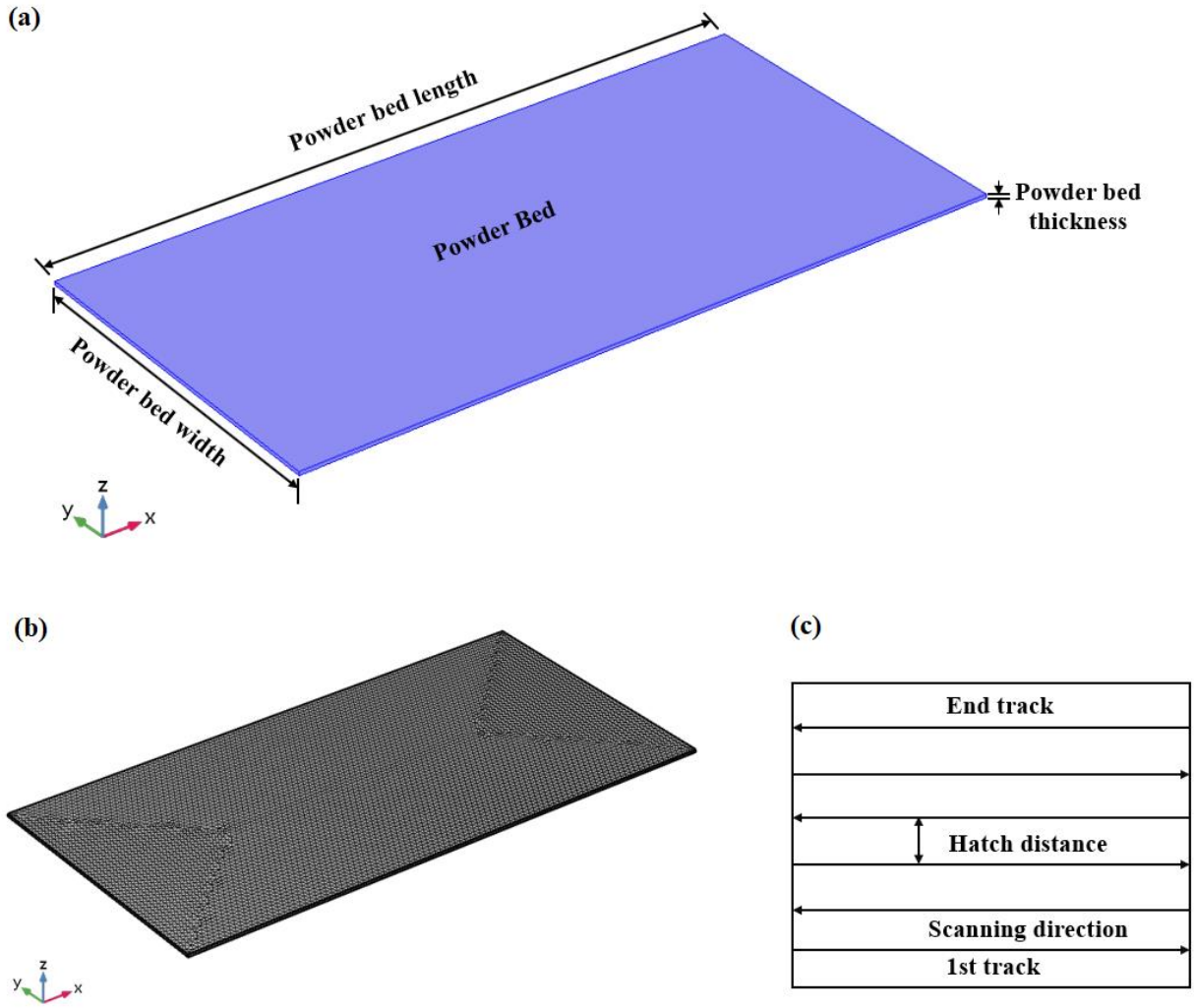
Fig. 20: 3D FE model of multi-track laser scanning throughout the SLM process. (a) Schematic of the designed geometry containing the substrate and powder bed, (b) 3D finite element mesh, and (c) scanning strategy.

3.1.2 Process Parameters

The primary purpose of FE model for PBF process is to investigate the relationship between different process parameters and the quality off the final printed part. The evolution of temperature gradient and thermal stress within thepart are closely correlated with scanning speed, scanning

48

pattern, laser power, spot size, etc. Table 2 lists the necessary process parameters used in the finite element simulation.

Table 2. Process parameters used in the finite element simulation.

Name	Description	Value
x_0	Path center X-Coordinate (mm)	0
y_0	Path center Y-Coordinate (mm)	0
P	Total laser power (W)	150,120
u	Laser velocity (mm/s)	1000,750
a_f	Length of x-semi axis in the front part of ellipsoid (µm)	100 [81]
a_r	Length of x-semi axis in the rear part of ellipsoid (µm)	200 [81]
b	Length of y-semi axis of ellipsoid (µm)	100 [81]
c	Length of z-semi axis of ellipsoid (µm)	80 [73]
ε	Emissivity	0.35 [56]
σ	Stefan–Boltzmann constant (W/ (mm^2.K))	5.67×10^{-14} [56]
T_∞	Ambient temperature (K)	293.15 [56]

3.1.3 Temperature dependent material properties of Ti-6Al-4V

An effective material model which considers the variation of properties during the cycle of heating and cooling processes is fundamental. Since the temperature varies from tens of Celsius degrees to thousands of Celsius degrees during PBF processes, most of the physical properties change drastically. The temperature-dependent thermal and mechanical properties of Ti-6Al-4V used in the analysis for powder bed are shown in Table 3 and Table 4, respectively

Table 3. Temperature dependent thermal properties of Ti6Al4V [59].

Temperature ($^\circ C$)	Density (kg/m^3)	Specific Heat (J/kg-K)	Thermal conductivity (W/m-K)
25	4420	546	7
100	4406	562	7.45
300	4381	584	8.75
900	4294	734	20.2
1100	4267	660	21
1500	4205	732	25.8
1600	4198	750	27
1700	3886	831	83.5
1800	3818	831	83.5

Table 4. Temperature dependent mechanical properties of Ti6Al4V [76].

Temperature ($^\circ C$)	Thermal expansion, α_e ($1^\circ C^{-1} x10^{-6}$)	Elastic modulus, E (GP_a)	Poisson's ratio, μ	Yield strength, σ_y (GP_a)	Shear modulus, τ (MP_a)
25	2.9	114.7	0.32	11.47	887
200	3.4	105.3	0.33	10.53	847
500	4.4	89	0.34	8.9	778
800	5.7	75	0.35	7.5	334
995	6.9	72.3	0.38	72.3	38
1200	7.65	64.6	0.39	64.6	27
1400	7.9	56.8	0.40	56.8	17
1650	8.6	45.4	0.41	45.4	3.8
1900	9	0	0.5	0	0.38

3.1.4 Heat source model

The heat source model is critical to simulate the heat input in the PBF processes. Throughout the SLM process, the heat from the laser beam experiences numerous absorption and reflections across the Ti_6Al_4V powders. The applied laser energy is separated into three portions, including reflection, absorption, and transmission of power. Only the absorbed energy was used to melt the powders. The laser energy can travel a certain depth through the powder bed. Therefore, the heat transfer through the depth direction on the powder bed was also considered in this presented model. As presented by Li et al [76], the Beer-Lambert attenuation law can be used to define the laser penetration in the depth direction, which is given as

$$Q(x,y,z) = \frac{Q_0(x,y)}{\delta} \exp(-\frac{|z|}{\delta})$$

(2)

Here, Q_0 is the heat flux on the upper surface (W/m^2), δ is the optical penetration depth for used material [82], $/z/$ is the absolute value of the z-coordinate.

The distribution of surface heat flux Q_0 across the powder bed is presumed to be a Gaussian relationship, which can be mathematically represented as [73]

$$Q_0(x,y) = \frac{2AP}{\pi R^2} \exp(-\frac{2((x-ut)^2+y^2)}{R^2})$$

(3)

where P is the laser power, A is the laser energy absorption coefficient, and R is the resulting heat source radius at which the energy density is minimized to $1/e^2$ at the center of the laser spot. The laser scanning direction is included by replacing x with (x-ut). By replacing Equation (3) into Equation (2), the volumetric heat source is given as:

$$Q(x,y,z) = \frac{2AP}{\pi\delta R^2} \exp(-\frac{2((x-ut)^2+y^2)}{R^2}) \exp(-\frac{|z|}{\delta})$$

(4)

Nowadays the double ellipsoid heat source model is one of the most widely employed in the simulations of the laser-based manufacturing due to its relative simplicity and accessibility. In this work, the spatial distribution of the heat input is calculated using double ellipsoid model offered by Goldak et al. [83]. This model considers a combined heat source composed of two ellipsoidal sources (Fig. 21). For a point (x, y, z) inside the front semi-ellipsoid, the heat flux is defined as [83]

$$Q(x,\ y,\ z,\ t) = \frac{6\sqrt{3}f_f P}{a_f bc\pi\sqrt{\pi}} \exp(-\frac{3x^2}{a_f^2} - \frac{3y^2}{b^2} - \frac{3z^2}{c^2}),\ \ z \geq 0. \tag{5}$$

For a point (x, y, z) inside the rear semi-ellipsoid, the heat flux is defined as [83]

$$Q(x,\ y,\ z,\ t) = \frac{6\sqrt{3}f_r P}{a_r bc\pi\sqrt{\pi}} \exp(-\frac{3x^2}{a_r^2} - \frac{3y^2}{b^2} - \frac{3z^2}{c^2}),\ \ z < 0. \tag{6}$$

Here, the heat flux Q *(x, y, z, t)* in this formulation is divided into two parts, *x, y,* and *z* are the local coordinates of a point with respect to the moving heat source, a_f, a_r, *b* and *c* are the set of lengths defining the front and rear semi-ellipsoids, respectively, *P* is the power of the laser beam. The parameter f_f is the correspondent front heat fraction and the rear part is represented by, f_r both 0.6 and 1.4 respectively [83].
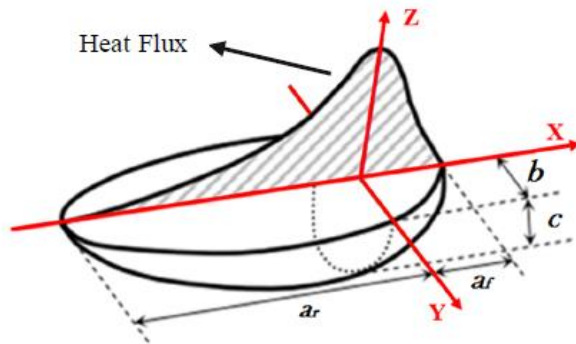
Fig. 21: Double ellipsoid heat source model (heat source moving through X-axis) [83].

3.1.5 Initial and Boundary Conditions

Heat transfer mechanisms during the PBF process are presented in Fig. 22. Boundary conditions mainly include heat convection, conduction and radiation and they are summarized in the follows. The initial conditions of the finite element model include a uniform temperature field all over the powder bed before applying the heat source, which can be described as,

$$T\ (x,\ y,\ z,\ 0) = T_0\ (x,\ y,\ z)\ \text{for the whole domain at } t = 0 \tag{7}$$

where $T_0\ (x,\ y,\ z)$ is the surrounding temperature and generally assumed as 293.15 K.

At the top surface of the developed model, heat transfer occurs among the powder bed, substrate, and their surroundings.

$$-k\frac{\partial T}{\partial n} = h_c(T - T_0) + \varepsilon\sigma(T^4 - T_0^4) \tag{8}$$

Here, the terms on the right side of the equation denote the heat loss owing to convection and radiation, successively. Furthermore, n denotes the normal direction of the surface, h_c is the convective heat transfer coefficient, ε is the surface emissivity, and σ is the Stefan–Boltzmann constant.
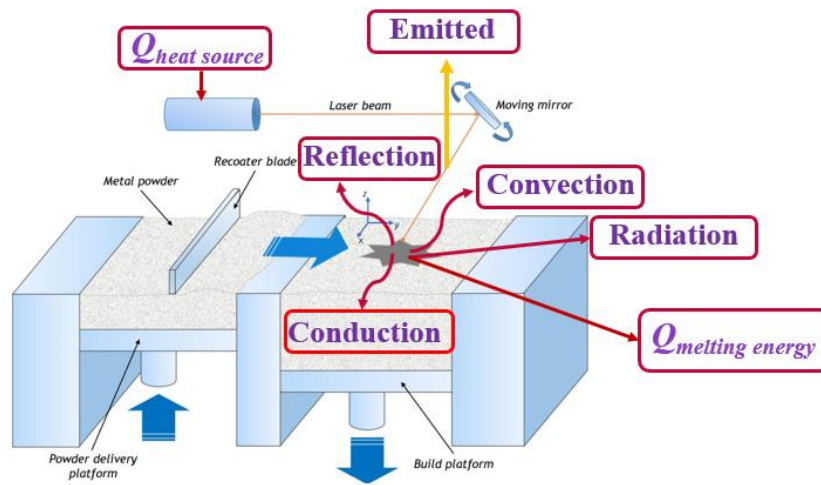
Fig. 22: Heat transfer mechanism in laser melting process

3.2 Thermal analysis

The heat transfer process in laser heating is a very complicated problem. During the laser heating process, the energy source mainly comes from the radiation of laser beam, latent heat of phase change, and deformation heat. When the metal material is melted or solidified, latent heat will be released, which will influence the heat transfer process. In addition, the plastic deformation of the material will generate deformation heat. Usually, this portion of heat is very small compared to the other two heat sources. Therefore, it is not considered in the heat transfer process.

3.2.1 Governing equations for heat transfer

The thermal equilibrium is achieved based on the following transient 3D heat conduction equation, which can be expressed as [84]

$$\rho C_p \frac{\partial x}{\partial y} + \rho C_p u \nabla T = \nabla (k \nabla T) + Q \tag{9}$$

in which T is the temperature, ρ is the density, Cp is the specific heat capacity, k is the thermal conductivity, Q is the absorbed heat, and u is the laser scanning speed.

The phase change behavior among the solid and liquid stages of a material can be input into Equation (9) with the following relationships [85]:

$$\rho = \theta \rho_{solid} + (1-\theta) \rho_{liquid} \tag{10}$$

$$C_p = \frac{1}{\rho} (\theta \rho_{solid} C_{p,solid} + (1-\theta) \rho_{liquid} C_{p,liquid}) + L \frac{da}{dT} \tag{11}$$

$$k = \theta k_{solid} + (1-\theta) k_{phase2} \tag{12}$$

$$a = \frac{(1-\theta)\rho_{liquid} - \theta\rho_{solid}}{\theta\rho_{solid} + (1-\theta)\rho_{liquid}} \tag{13}$$

$$\theta = \begin{cases} 0, & if\ T \leq T_S \\ \dfrac{T - T_L}{T_L - T_S}, & if\ T_S < T < T_L \\ 1, & if\ T \geq T_L \end{cases} \tag{14}$$

where θ is the phase fraction, L is the latent heat of the phase transfer from solid to liquid and a is the mass fraction, T_L is the liquidus temperature and T_S is the solidus temperature.

3.2.2 Fluid flow modelling

The large temperature gradient in the melting pool will cause a significant surface tension gradient, which creates Marangoni effects. These effects are also considered in this work and are given as [86]

$$F^{Marangoni} = \nabla_s \gamma \ \ where \ \ \gamma = \gamma_0 + \frac{d\gamma}{dT}\Delta T \tag{15}$$

where ∇_s denotes the surface gradient, γ is the surface tension, γ_0 is the surface tension at the liquidous point, $d\gamma/dT$ is the surface tension gradient, and ΔT is the temperature difference.

To consider the flow behavior in the molten pool, the Navier-Stokes equations were used to model the laminar flow in the melt pool and are given as [86]

$$\rho \frac{\partial u}{\partial t} + \rho(u.\nabla)u = \nabla.[-pI + \mu(\nabla u + (\nabla u)^T)] + \rho g + F \tag{16}$$

$$\rho \nabla.(u) = 0 \tag{17}$$

55

Where p is the pressure, μ is the dynamic viscosity, I is the three-dimensional unity tensor, ρg is the gravity force, and F represents the other body forces, which are surface tension gradient-driven Marangoni forces already described in this work.

3.3 Mechanical analysis

The finite element modeling of PBF process includes two different processes, which are the non-linear transient thermal analysis and the quasi-static elastoplastic mechanical analysis. After the temperature field obtained from the above thermal analysis, a mechanical analysis is performed to approximate the thermal stress and deformation. The temperature field is now applied as the thermal load for the mechanical analysis. The thermal-mechanical analysis has been performed in coupled way.

3.3.1 Governing equations for thermal stress and strain

The temperatures from the thermal analysis become the loads for the structural analysis. The same finite element mesh has used in the thermal analysis is employed in the thermal stress analysis and the boundary conditions. The relationship between the stress and the strain is defined as [76]:

$$\{\sigma\} = [D]\{\varepsilon^e\} \tag{18}$$

where $\{\sigma\}$ is the stress vector; $[D]$ is the elasticity matrix; $\{\varepsilon^e\}$ is the elastic strain vector and for the ideal elastic-plastic body,

$$\{\varepsilon^e\} = \{\varepsilon\} - \{\varepsilon^p\} - \{\varepsilon^t\} \tag{19}$$

Where $\{\varepsilon\}$, $\{\varepsilon^p\}$ and $\{\varepsilon^t\}$ are the total strain vector, the plastic strain vector, and the thermal strain vector, respectively.

Eq. (20) can also be written as:

$$\{\varepsilon\} = [D^{-1}]\{\sigma\} + \{\varepsilon^p\} + \{\varepsilon^t\} \tag{20}$$

since the material is assumed to be isotropic, the above stress-strain equation can be expressed in Cartesian coordinates as [76]:

$$\varepsilon_x = \frac{1}{E}[\sigma_x - \mu(\sigma_y + \sigma_z)] + \varepsilon_x^p + \varepsilon^t$$

$$\varepsilon_y = \frac{1}{E}[\sigma_y - \mu(\sigma_x + \sigma_z)] + \varepsilon_y^p + \varepsilon^t$$

$$\varepsilon_z = \frac{1}{E}[\sigma_z - \mu(\sigma_x + \sigma_y)] + \varepsilon_z^p + \varepsilon^t$$

$$\gamma_{xy} = \frac{\tau_{xy}}{2G} + \gamma_{xy}^p, \ \gamma_{xz} = \frac{\tau_{xz}}{2G} + \gamma_{xz}^p, \ \gamma_{yz} = \frac{\tau_{yz}}{2G} + \gamma_{yz}^p, \tag{21}$$

where E, G, μ are the elastic modulus, shear modulus and Poisson's ratio, respectively. A typical calculation method of thermal strain from Eq. (22) is [76]

$$\varepsilon^t = \alpha_e \Delta T = \alpha_e (T - T_\infty) \tag{22}$$

where α_e is the coefficient of thermal expansion; T is the temperature at time t, and T_∞ the reference temperature at $t = 0$.

When the stress exceeds yield limit of the material, plastic deformation will occur. According to Prandtl-Reuss equations in plasticity theory, the plastic strain increment is proportional to the instant deviator stress and shear stress as follows [76]:

$$\frac{d\varepsilon_x^p}{\sigma_x^{'}} = \frac{d\varepsilon_y^p}{\sigma_y^{'}} = \frac{d\varepsilon_z^p}{\sigma_z^{'}} = \frac{d\gamma_{xy}^p}{\tau_{xy}} = \frac{d\gamma_{yz}^p}{\tau_{yz}} = \frac{d\gamma_{zx}^p}{\tau_{zx}} = d\lambda$$

$$\sigma_x^{'} = \sigma_x - \sigma_m$$

$$\sigma_y^{'} = \sigma_y - \sigma_m \tag{23}$$

$$\sigma_z^{'} = \sigma_z - \sigma_m$$

Where $\sigma_x^{'}$, $\sigma_y^{'}$, $\sigma_z^{'}$ are the deviator stresses of x, y and z directions in Cartesian coordinates, respectively; $d\lambda$ is the instant positive constant of proportionality; σ_m is the mean value of stress and is defined as [76]:

$$\sigma_m = \frac{\sigma_x + \sigma_y + \sigma_z}{3} \tag{24}$$

Then Eq. (19) may be substituted by,

$$\varepsilon_x = \frac{1}{E}[\sigma_x - \mu(\sigma_y + \sigma_z)] + \int \sigma_x' d\lambda + \alpha_e \Delta T$$

$$\varepsilon_y = \frac{1}{E}[\sigma_y - \mu(\sigma_x + \sigma_z)] + \int \sigma_x' d\lambda + \alpha_e \Delta T \tag{25}$$

$$\varepsilon_z = \frac{1}{E}[\sigma_z - \mu(\sigma_x + \sigma_y)] + \int \sigma_x' d\lambda + \alpha_e \Delta T$$

$$\gamma_{xy} = \frac{\tau_{xy}}{2G} + \int \tau_{xy} d\lambda, \ \gamma_{xz} = \frac{\tau_{xz}}{2G} + \int \tau_{xz} d\lambda, \ \gamma_{yz} = \frac{\tau_{yz}}{2G} + \int \tau_{yz} d\lambda,$$

In the structural analysis, there will be a residual deformation after cooling when the yield point is met. Both the elastic and the plastic deformations affect the deformation zone. The COMSOL Multiphysics analyses the deformation of the material after cooling according to the elastic-plastic strain state.

To solve the mathematically derived problem, the FE method was developed by means of COMSOL Multiphysics in which thermo-mechanical coupling were established.

Chapter 4

Materials and Experimental Methods

SLM experiments were performed using a SLM printer (MetalSys150, Winforsys co., Ltd., Yongin-si, South Korea) with a YLP-200-AC-Y11 IPG Ytterbium Fiber Laser (Winforsys co., Ltd., Yongin-si, South Korea) (highest laser power of 200 W). The chamber was occupied with argon protection gas to keep the oxygen level below 0.1%.

In this study, a commercial Ti-alloy (Ti6Al4V) powder provided by the (SLM Solutions Group AG, Lübeck, Germany), was used as a raw material with the resulting nominal chemical composition (wt.%): Ti-balance, Al-(5.5–6.50), V-(3.50–4.50), Fe-0.25, C-0.08, N-0.03, O-0.13, H-0.0125. The average powder size was about 23–60 μm.

A TELOPS FAST-IR (M350) thermal camera (TELOPS, Quebec, Canada) with a spatial resolution of 640 pixels $\times$ 512 pixels, and a maximum frame rate of 4980 Hz was employed to determine the temperature profile on the melt pool and the powder bed. The built part has dimensions of $20 \times 10 \times 0.1$ mm (length $\times$ width $\times$ thickness) e.g., one layer. The camera was mounted on a tripod and fitted near to the view window, straightly focusing on the laser scanning area as presented in Fig. 23. The process parameters for experiments were chosen as follows: laser powers (P): 120 W, 150 W; scan speeds (u): 750 mm/s, 1000 mm/s.
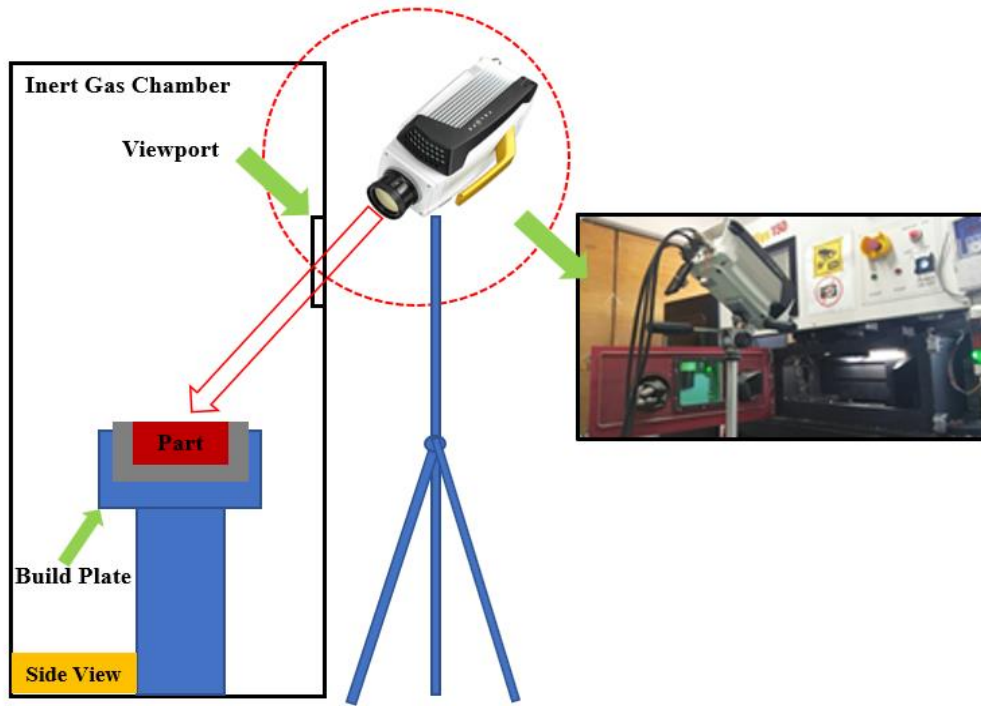
Fig. 23: Schematic plot for experimental set up.

Chapter 5

Results and Discussion

5.1 Determination of suitable heat source

To determine the most suitable heat source among the three heat sources used in the current study, the peak melt pool temperatures from the simulation results for the three heat sources are compared with the experimental data published [87]. The SLM simulations are carried out at constant laser power 30W, varying the scanning speed 50 mm/s, 100 mm/s, 200 mm/s, 300 mm/s as listed in [87]. The predicted melt temperature by using surface Gaussian heat source, volumetric Gaussian and Goldak heat source has been presented in Fig. 24, Fig. 25, and Fig. 26 respectively.
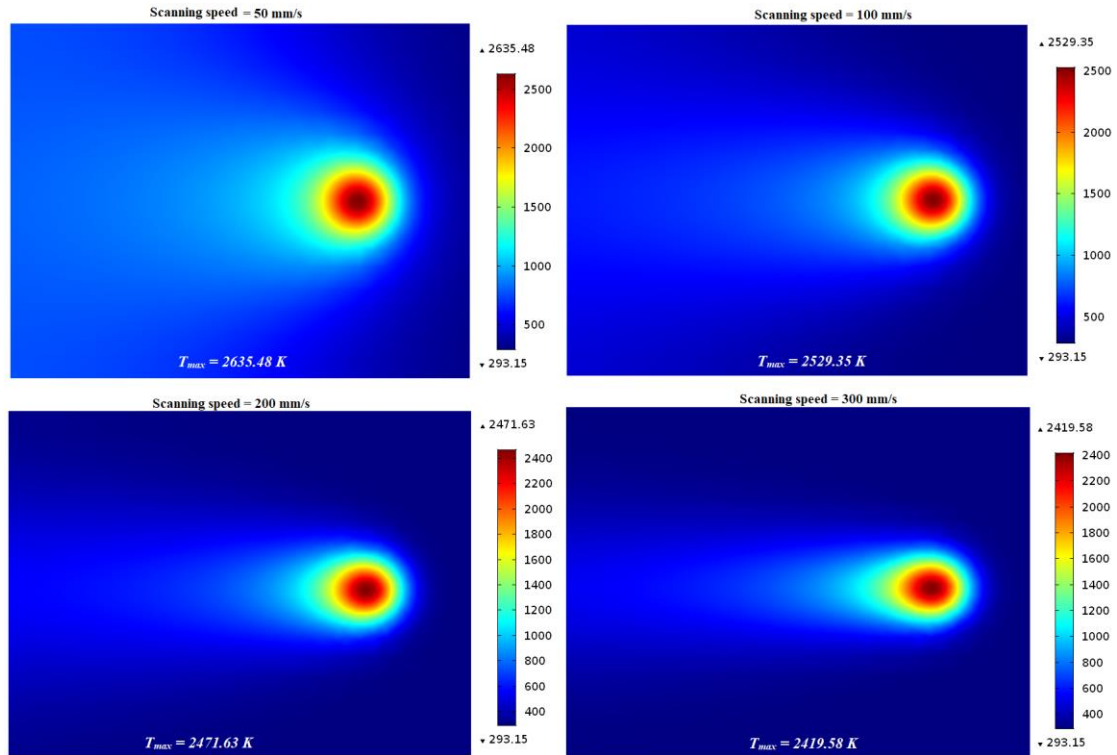
Fig. 24: Numerical simulation of temperature fields during laser scanning of Ti6Al4V substrate by using surface gaussian heat source.
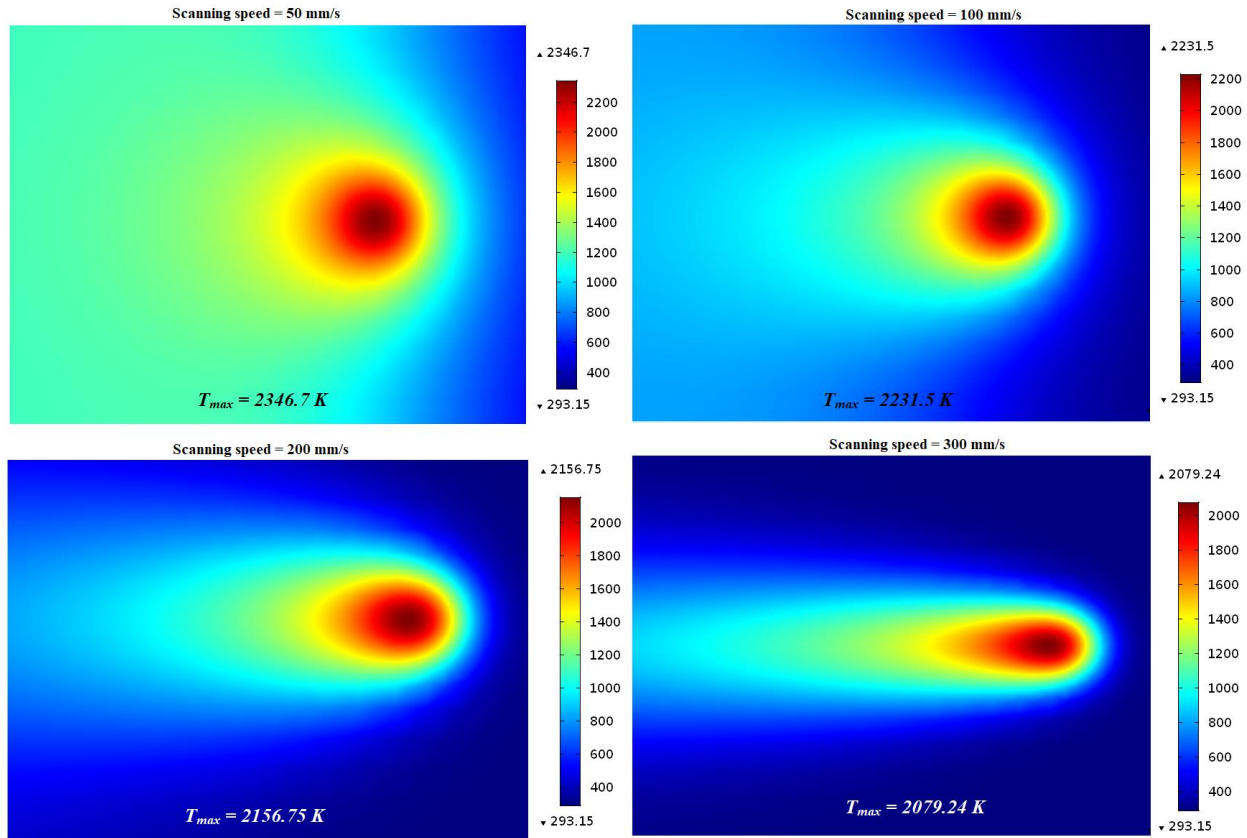
Fig. 25: Numerical simulation of temperature fields during laser scanning of Ti6Al4V substrate by using volumetric gaussian heat source.

The simulated melt pool temperatures are higher than the experimental results, irrespective of the heat source used as shown in Fig. 27. This difference may arise due to the possible difference in the thermo-physical properties and porosity used in the simulations and actual values during experiments. Among the three heat sources, the surface Gaussian heat source predicted the highest values of peak temperatures, much higher than the experimental data. This is expected as the whole energy absorption is limited to the top surface only, which raises the temperature to extremely high levels. Again, the closest matching results are provided by the Goldak volumetric heat source.
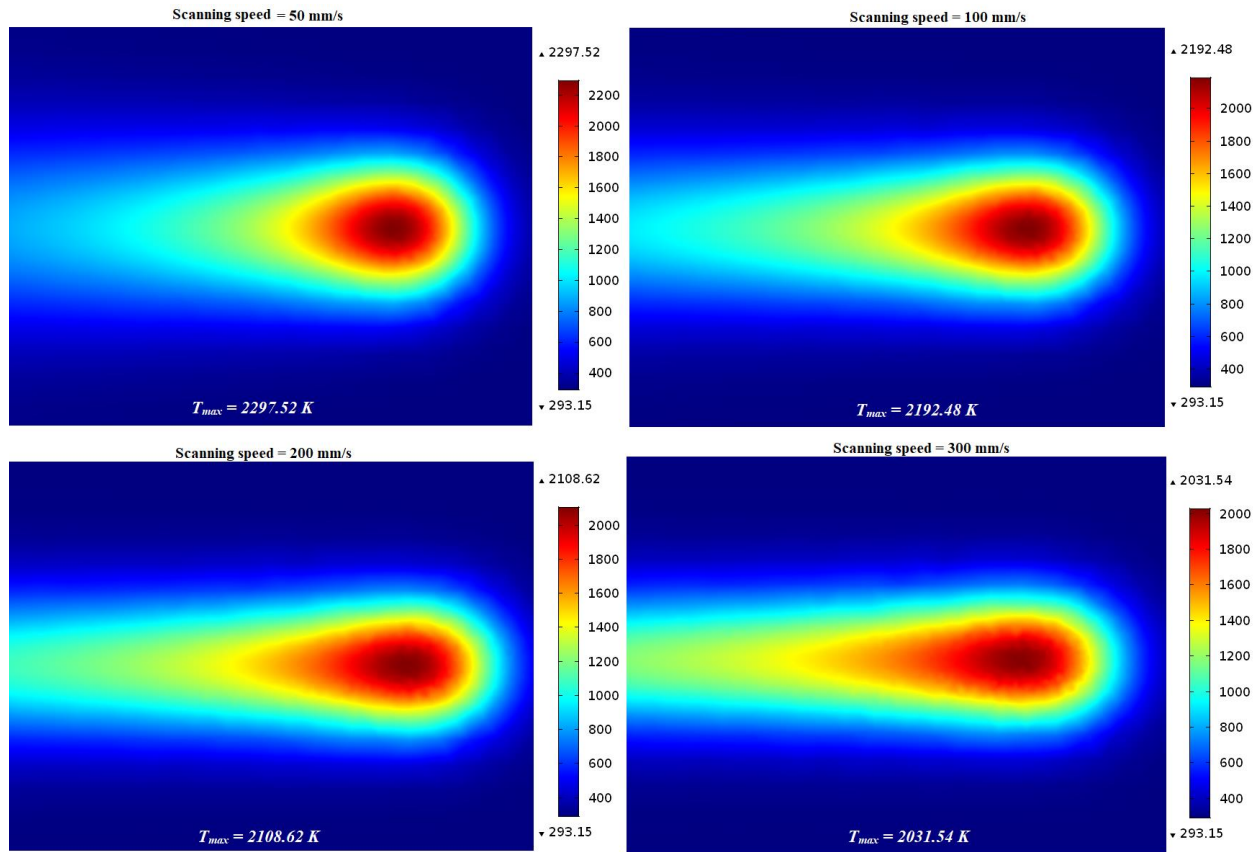
Fig. 26: Numerical simulation of temperature fields during laser scanning of Ti6Al4V substrate by using volumetric goldak heat source.
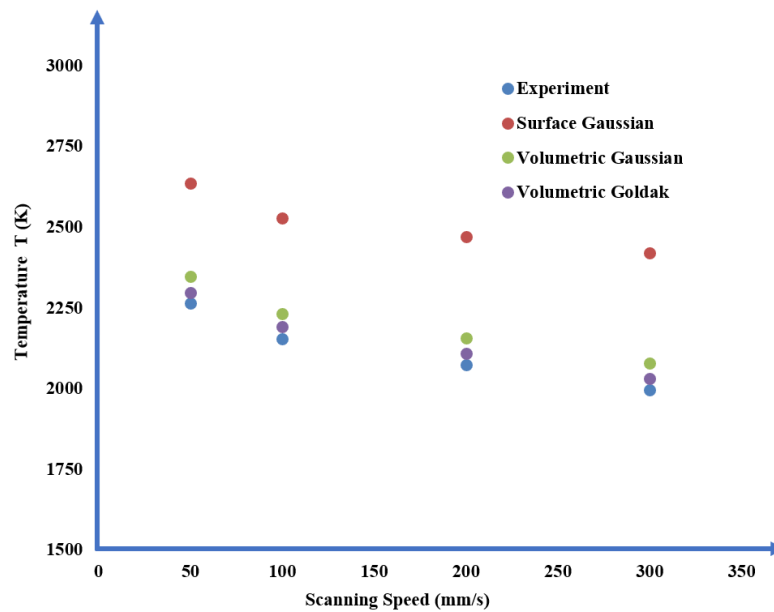
Fig. 27: Comparison of the predicted and the experimental [87] maximum temperature

From the validations, it is clear that the Goldak volumetric heat source is the suitable heat source to employ in modelling and simulation of SLM of Ti6Al4V powder. The simulation results have some differences with the experimental results; these can be attributed to many factors that are either not considered or are very difficult to consider in the model. Overall, this result shows the advantages of using the volumetric Goldak heat sources in modelling and simulation of the SLM of Ti6Al4V powder instead of the traditional surface Gaussian heat source.

5.2 Numerical model validation by published literature

To confirm the thermal model and numerical approaches presented in this research, the developed model by using Goldak heat source was initially compared with published experimental results.

Yadroitsev et al. [56] experimentally measured the brightness temperature of the melt pool by using a laser power of 50 W and a scanning speed of 100 mm/s for Ti_6Al_4V alloy. Fig. 28 (a) illustrates the contrast of the calculated temperature field in the *xy*-plane across the laser moving path (presented in Fig. 28 (b)) with the experimentally measured peak temperature for the SLM of Ti_6Al_4V. Based on this comparison, the calculated peak temperature across the laser scanning direction concedes well with the trends in the experimentally determined temperature profile.
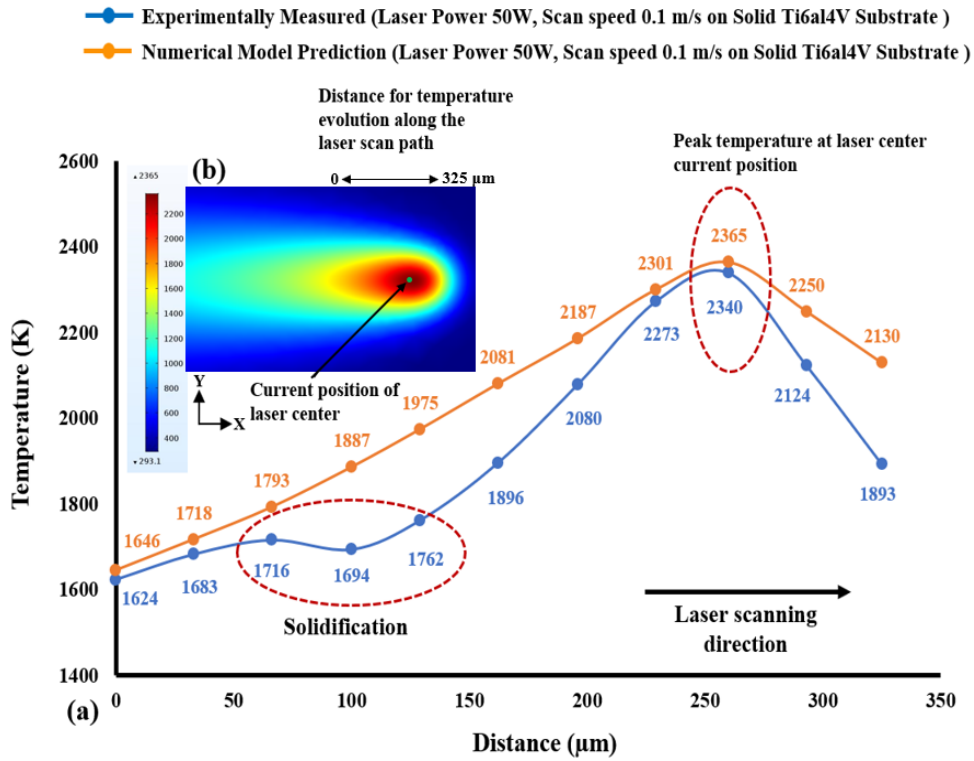
Fig. 28: (a) Comparison of the FE model calculated temperature in the xy-plane along the laser moving path with the experimentally measured peak temperature along the laser scanning direction adapted from reference [56] and (b) Numerically predicted temperature distribution along the xy-direction considering a 325 µm laser scan path.

Fischer et al. [73] used a Raytheon infrared camera for determining the temperature distribution by applying a laser power of 3 W and a scanning speed of 1 mm/s. Fig. 29 demonstrates the temperature profile measured by Fischer et al. [73] and the peak temperature scale was in the range of 2500 K to 3000 K. Numerical analysis was conducted applying process parameters similar to those used by Fischer et al. [73] during their experiments. As demonstrated in Fig. 30, the highest temperature after 0.75 s is about 2640.9 K which falls between the measured experimental values.
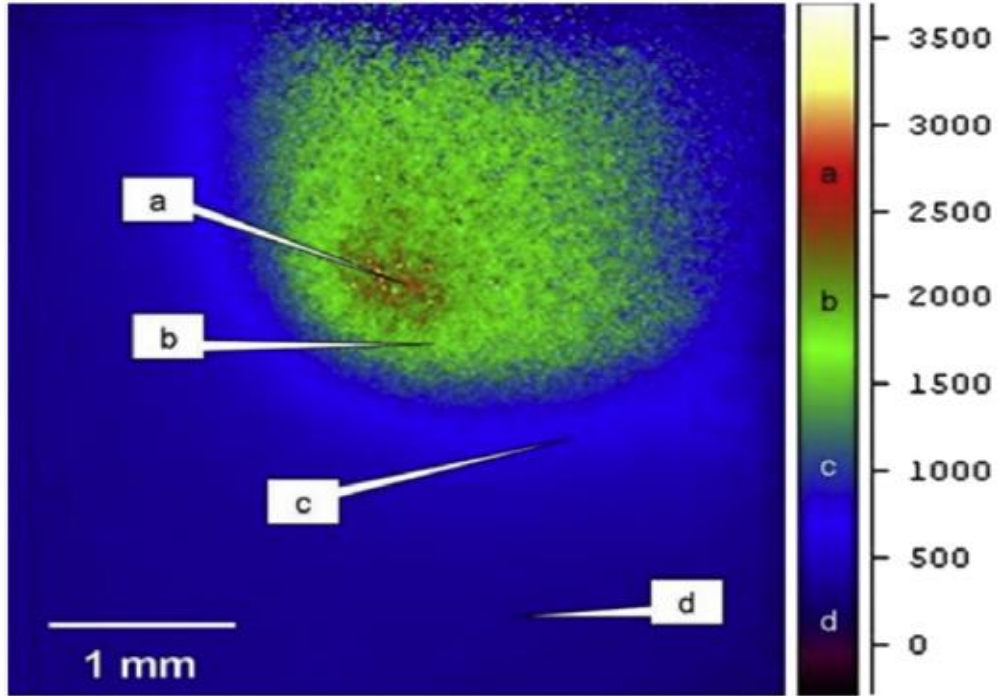
Fig. 29: Experimentally measured average temperature profile throughout the laser sintering process at $P = 3$ W and $u = 1$ mm/s.
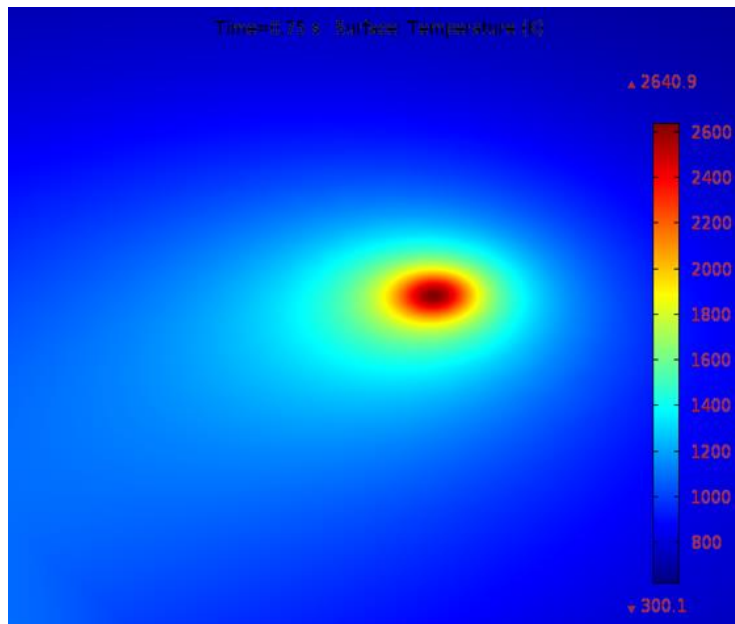
Fig. 30: Numerically predicted surface temperature contours at $P = 3$ W and $u = 1$ mm/s.

5.3 Temperature Distribution

During the SLM process, the temperature field on the powder bed deviates quickly with time and locations; these are critical issues for the printed product quality. The melting zone undergoes solidification in the wake of the heat source because of the moving laser beam and fast heat transmission from the melting zone to the surroundings. The solidification process starts once the temperature of the melt pool falls under the liquidus temperature. Afterwards it cools down to the ambient temperature for fabricating the complete products.

Fig. 31 illustrates the temperature contours at the start of laser moving, from which the peak temperature gradient in the laser spot region can be distinctly seen to the used 3D Gaussian heat source. The temperature of the powder bed rises quickly owing to the absorption of high energy irradiated from the heat source, initiating a melting pool in the powder bed once the temperature surpasses the liquidus point of Ti_6Al_4V (1928 K). Fig. 32 illustrates the predicted temperature profiles and melt pool formation as the heat source reached various locations throughout the SLM process for P = 120 W and u = 1000 mm/s. Fig. 32a demonstrates the temperature profiles at the final point of the first scanning track (at t = 0.02 s). At this point, the predicted highest temperature on the melt pool was about 2108.2 K, which exceeded the liquidus temperature of Ti_6Al_4V. Besides, the lowest temperature was only 293.15 K in most of the area of the powder bed and the substrate. The corresponding temperature contours and the melt pool region is presented in Fig. 32b starting with the isothermal contours at 1900 K and going to the highest temperature of the melt pool. The melt pool size, as presented by the isothermal contours, provides a visual idea of the spatial energy distribution for a consistent heat source. The calculated temperature in the isothermal contours was larger than the liquidus temperature of Ti_6Al_4V. As a result, a little melt pool developed within this region. The length and width of the melt pool were approximately 237.6

μm and 90.7 μm, respectively. As the heat source arrived at the middle of the powder bed at $t =$ 2.015 s, the maximum temperature of the melt pool increased to 2193.6 K in the center of the melt pool, as presented in Fig. 32c. The melt pool length and width improved by approximately 356.4 μm and 110.2 μm, at a time of 1.015 s, as shown in Fig. 32d. The heat source moved to its final position, and after that the heat source was no longer specified. Thus, only heat loss happens at this end position. At the ending of the final scanning track at $t = 4.02$ s, the predicted lowest and highest temperature of the powder bed raised to approximately 528.7 K and 2315.5 K, respectively, as presented in Fig. 32e. Fig. 32f represents the resulting melt pool length and width (approximately 512.2 μm and 137.8 μm) at a time of $t = 4.02$ s, which are larger than those at 0.02 s and 2.015 s. Therefore, the length of the melting pool increased more than the width of the melting pool as the laser irradiating time increased on the powder bed. For the specified numerical circumstances, the width of the melt pool at various positions was larger than the hatch distance (30 μm), which led to smooth melt tracks due to the development of a large enough melt pool between the adjacent tracks.
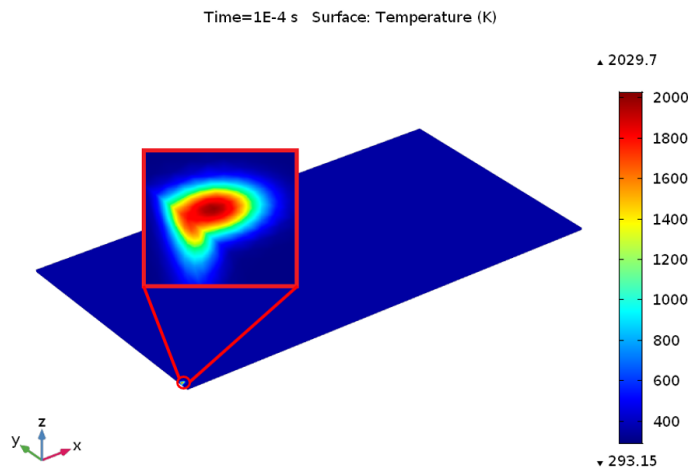
Fig. 31: Temperature distribution at the start of laser scanning.
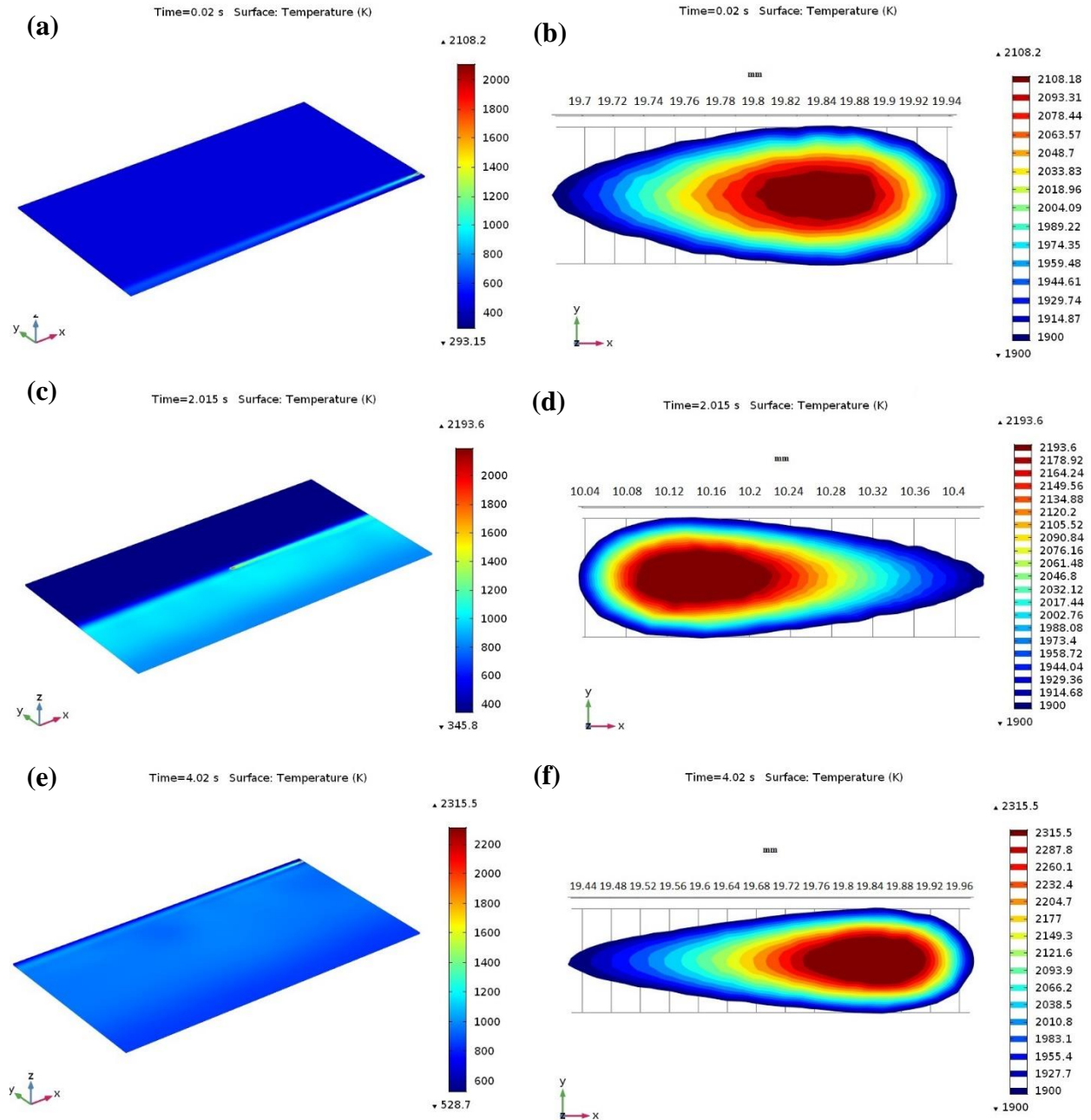
Fig. 32: Temperature contours during the SLM process at $P = 120$ W and $u = 1000$ mm/s: (**a**) on the Ti6Al4V powder bed at the ending of the first scanning track at $t = 0.02$s and (**b**) isothermal contours around the melt pool at $t = 0.02$ s; (**c**) on the middle of Ti6Al4V powder bed at $t = 2.015$ s and (**d**) isothermal contours around the melt pool at $t = 2.015$ s;

(**e**) on the Ti6Al4V powder bed at the ending of the last scanning track (after scanning a total of 201 tracks) at $t = 4.02$ s and (**f**) isothermal contours around the melt pool at $t = 4.02$ s.

5.3.1 Variation of Temperature Distribution with Different Process Parameter

The development of peak temperature with respect to time for different process parameters during the SLM process is presented in Fig. 33 and Fig. 34. Once the laser scan speed decreased from 1000 mm/s to 750 mm/s (at $P = 120$ W), a maximum temperature of 2306.4 K was predicted at a time of 0.0266 s, which is larger than the liquidus temperature of Ti$_6$Al$_4$V, as presented in Fig. 33a. When the heat source reached at the final scanning track (at $t = 5.36$ s), the observed temperature was 2624.7 K (Fig. 33b), which was also over the liquidus temperature of Ti$_6$Al$_4$V. Once the laser power was further raised to 150 W (at $u = 1000$ mm/s), the predicted peak temperature was 2271.2 K (at $t = 0.02$ s), and it increased to 2530.1 K at the ending of the final scanning track (at $t = 4.02$ s), as demonstrated in Fig. 34a,b, respectively.

Throughout the SLM process, an elevated temperature gradient can be found among the melt pool when applying higher laser power (150 W) with a comparative lower scanning speed (750 mm/s) and this phenomenon happens owing to absorption of adequate laser energy by the supplied material powders. Furthermore, an excessive heat growth phenomenon can happen which can remelt the previously built scanning path. In this situation, a higher temperature gradient of 2509.6 K (at $t = 0.0266$ s) was obtained in the melt pool which was further raised to 2891.2 K at the final point of the scanning process (at $t = 5.36$ s), as presented in Fig. 34c,d, respectively.

The numerical findings indicated that the applied laser power directly impacted the temperature fields of the powder bed throughout the SLM process; however, the laser scanning

speed changed the temperature distribution by varying the laser exposure time among the applied

heat source and the powder bed
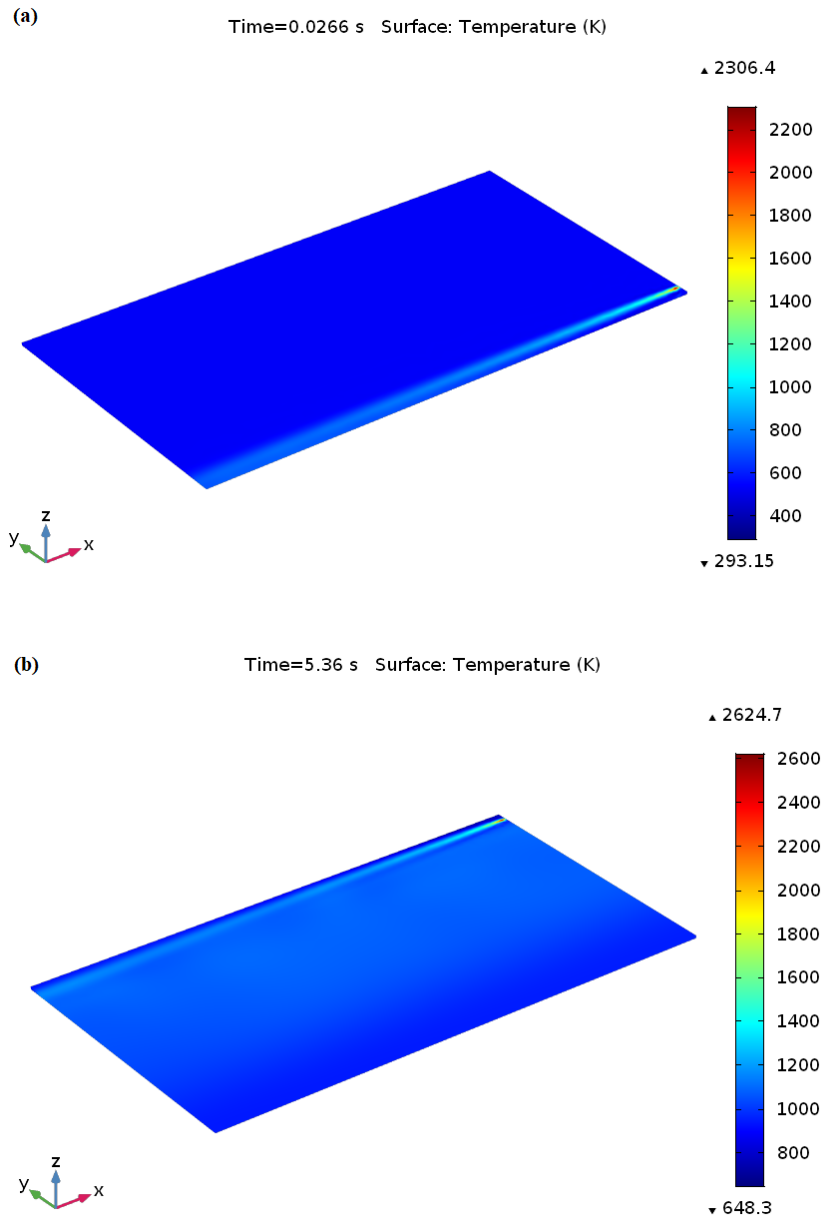
Fig. 33: Temperature profiles throughout the SLM process at P =120 W and u = 750

mm/s. On the Ti6Al4V powder bed (**a**) at the ending of the first scanning track at t =

0.0266s and (**b**) at the ending of the final scanning track (after scanning a total of 201

tracks) at t = 5.36s.
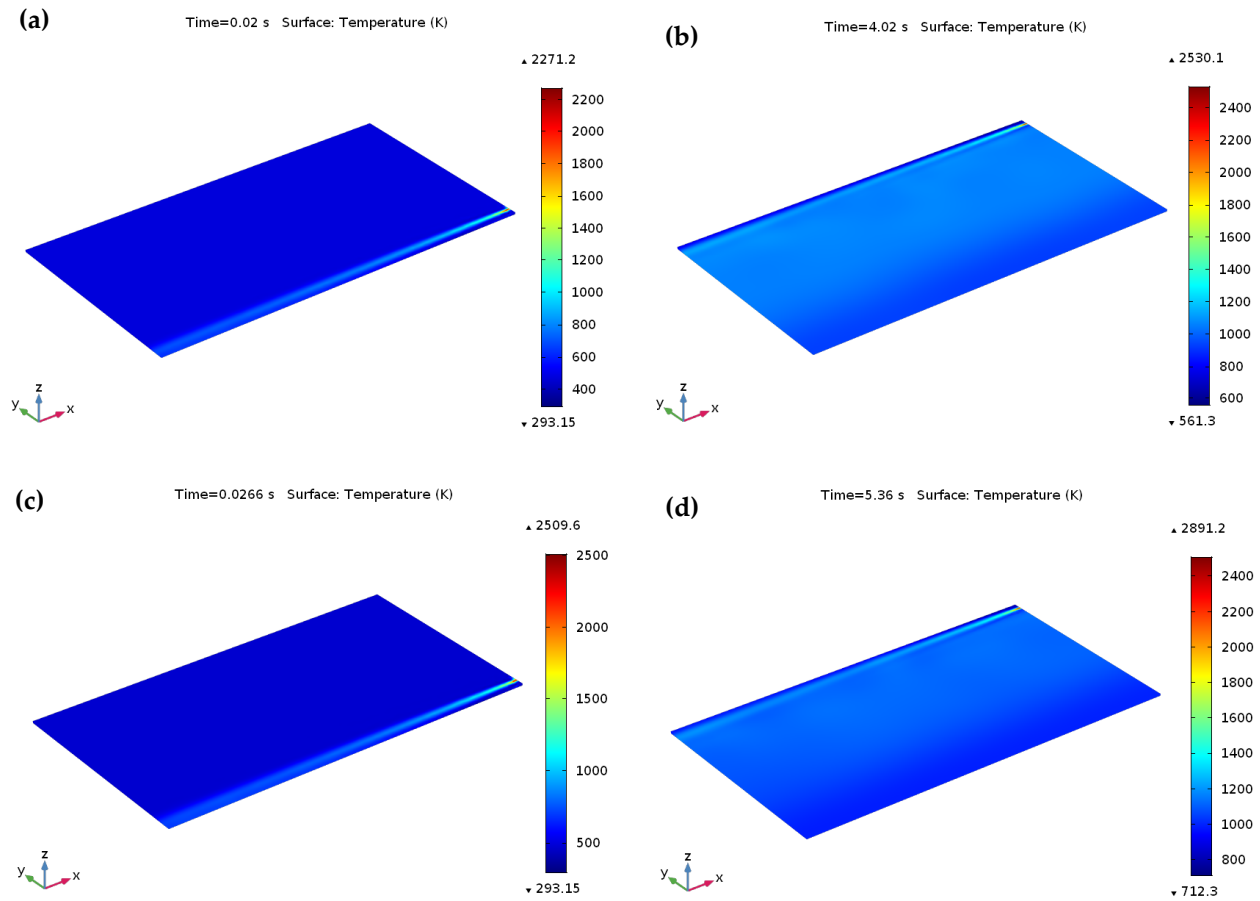
Fig. 34: Temperature profiles throughout the SLM process at P =150 W and u = 1000 mm/s, 750 mm/s. On the Ti6Al4V powder bed (**a**) at the ending of the first scanning track at t = 0.02 s, (**b**) at the ending of the final scanning track (after scanning a total of 201 tracks) at t = 4.02 s, (**c**) at the ending of the first scanning track at t = 0.0266s, (**d**) at the ending of the final scanning track (after scanning a total of 201 tracks) at t = 5.36s.

5.3.2 Molten Pool Dimensions

Throughout the SLM process, it is a significant challenge to analyze the melting pool length and depth using experiments. Dilip et al. [3] experimentally determined the single-track melt pool width and depth by varying the SLM process parameters. It was reported that single-track with the

process parameter sets of 150 W-750 mm/s, and 150 W-1000 mm/s had a modest energy input and produced a regular melt pool size with enough depth of penetration. The experimentally measured melt pool width and depth were approximately 134 μm and 72 μm, respectively, for the combination of 150 W-750 mm/s, and approximately 116 μm and 54 μm, respectively, for the combination of 150 W-1000 mm/s. Therefore, the calculated melt pool width and depth are comparable with the experimental findings for the single-track result. Fig. 35 describes the calculated melt pool dimensions using laser powers of 120 W, and 150 W, and scanning speeds of 750 mm/s, and 1000 mm/s for the single-track laser scanning. The melting pool size (length, width, and depth) were observed from the single-track temperature distribution results considered from the melting point (1928 K) to the peak temperature along the scanning direction. At a low scanning speed, the heat source can melt the irradiated zone for a longer time rather than the high scanning speed, resulting in a large melt pool size for the high temperature in the melting zone. However, the heat source can melt the irradiated zone for a shorter time at a high scanning speed, resulting in a small melt pool for the low temperature gradient in the melting zone. Fig. 35 a, b clearly illustrates the calculated melt pool size for the combination of 120 W-1000 mm/s and 120 W-750 mm/s. At the same laser power of 120 W, the calculated melt pool width and depth was approximately 90.7 μm and 34.2 μm at $u = 1000$ mm/s, while the calculated melt pool depth and width was approximately 114.6 μm and 53.1 μm at $u = 750$ mm/s. Fig. 35c represents the calculated melt pool size for the combination of 150 W-1000 mm/s. The calculated melt pool width was approximately 110.8 μm, which agrees with the reported experimental results with 5% error. The predicted melt pool depth was approximately 50.9 μm, which coincides with the reported experimental results with 6% error. The melt pool size is also predicted by decreasing the scanning speed to 750 mm/s at the same laser power, which is demonstrated in Fig. 35d. The predicted melt

pool width was approximately 130.9 μm, which was 2% less than the experimental findings, and

the predicted melt pool depth was approximately 68.1 μm, which was 5% less than the reported

experimental results.
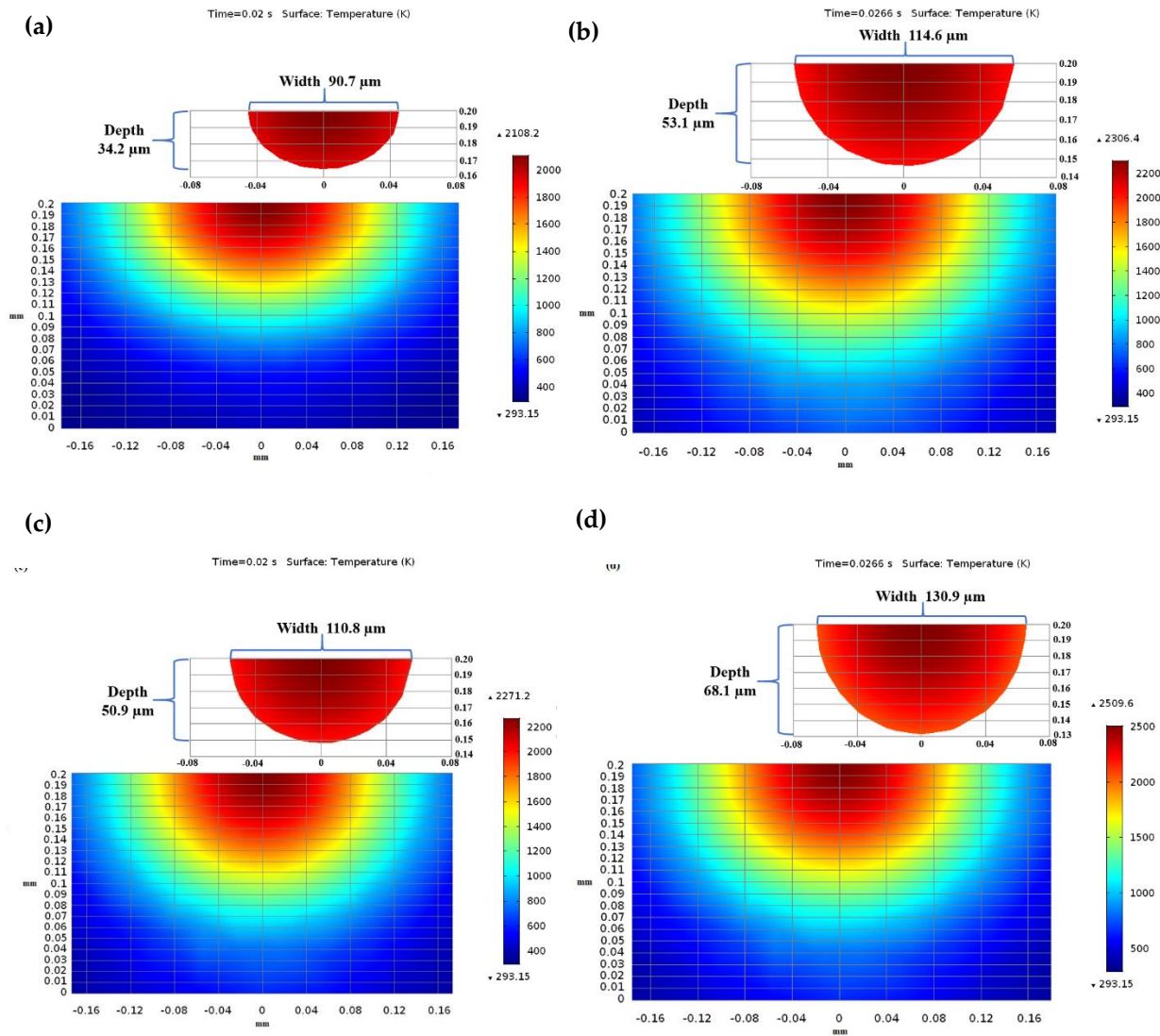
Fig. 35: Variation in the melt pool geometry at various laser powers and scan speeds. Predicted melt pool width and depth at (**a**) 120 W-1000 mm/s, (**b**) 120 W-750 mm/s, (**c**) 150 W-1000 mm/s, (**d**) 150 W-750 mm/s, respectively.

Fig. 36 was presented to analyze the variation of melt pool length by applying the different SLM process parameters. For each specific laser power, the melting pool length was predicted by varying the scanning speed. At a laser power of 120 W, a clear increasing tendency was determined for the melt pool length from 237.5 μm (at $u = 1000$ mm/s) to 350.7 μm (at $u = 750$ mm/s). Once the applied laser power was raised from 120 W to 150 W, the length of the melt pool improved to 450.7 μm (at $u = 1000$ mm/s) and 520.2 μm (at $u = 750$ mm/s). Therefore, the simulation findings exhibited that the melt pool size (length, width, and depth) raised linearly with the applied laser power. As can be seen from the evaluations made based on the literature, the presented numerical model can determine the melting pool width and depth in an acceptable range.
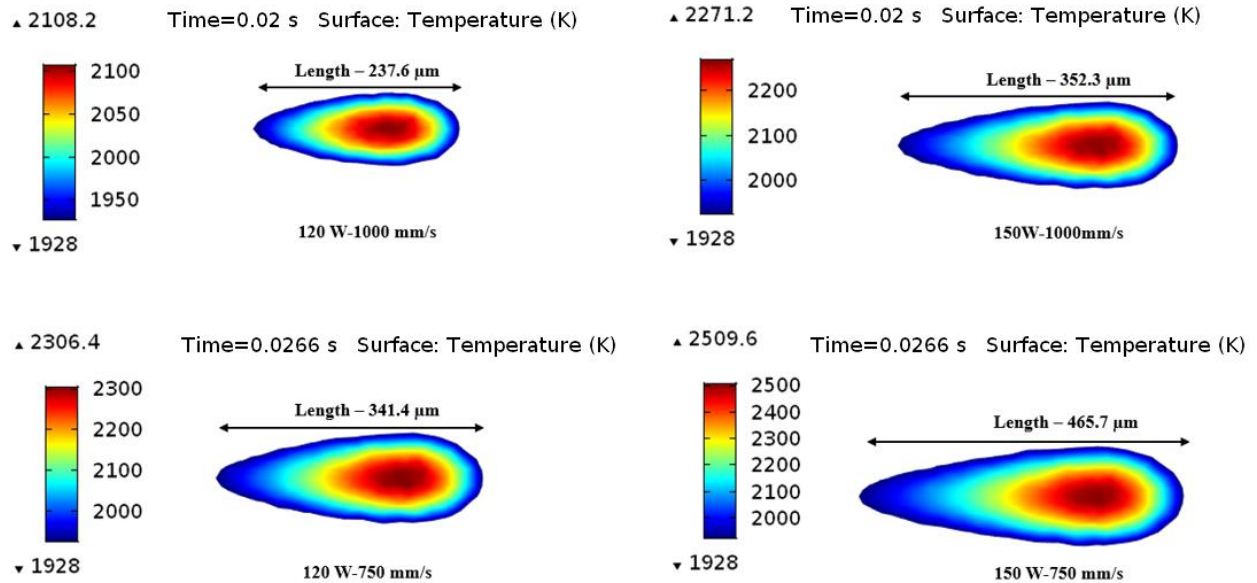
Fig. 36: Variation of the melt pool length at different process parameters in the scanning direction at the end of the first scanning track.

5.3.3 Experimental Validation

To confirm the reliability of the presented simulation model, experiments were carried out to determine the temperature distributing characteristics throughout the SLM process. By using the thermal imager, the developed temperature profiles in the melt pool were monitored, and the images were captured in real time. Fig. 37 displays the characteristics of temperature distributions and melt pools at various laser powers and scanning speeds. To measure the temperature, thermal camera emissivity was fixed to 0.35 with a transmission rate of 1.0. These thermal pictures represent the temperature profiles obtained by moving the heat source. A high-temperature region was found close to the laser spot center and progressively cooled down behind the melting pool as the heat source moved away. Fig. 37a presents the temperature profiles for the first scanning track at $P = 120$ W and $u = 1000$ mm/s. By means of the heat source moved through the powder bed in the first scanning track, the temperature increased rapidly and exceeded the melting point, leading to powder melting. The temperature progressively decreased as the laser beam moved away. Taking the emissivity as $\varepsilon \sim 0.35$, the highest temperature of the melt pool at the time of 0.02s was about 2132.3 K (1859.2 °C) (white color) which surpassed the melting temperature of Ti_6Al_4V. For multi-track scanning, the hatch distance influences the highest temperature in the present scanning track due to the enduring heat provided by the previous tracks. Since the radius of the laser beam is larger than the hatch distance of 30 μm, some areas of the former track remelted, which led to the rise of the peak temperature at the ending of the SLM process. As a result, the temperature increased to 2353.7 K (2080.6 °C) at the end point of the final track, and the total scanning time was 4.02 s, as presented in Fig. 37(b). In case of low scanning speed of 750 mm/s (at the same $P = 120$ W), the temperature increased to 2329.5 K (2056.4 °C) at a time of 0.0266 s, and 2657.3 K (2384.2 °C) at a time of 5.36 s, as presented in Fig. 37c,d, respectively.

Another set of experiments was carried out at the process parameter sets of 150 W-1000 mm/s and 150 W-750 mm/s. Fig. 37e describes the temperature contours at the end of the first scanning track for $P = 150$ W and $u = 1000$ mm/s. The peak temperature in the melt pool was determined approximately 2296.8 K (2023.7 °C) at 0.02 s. The temperature increases in the second track leading to the end track were attributed to reheating induced by the heat source due to hatch spacing, and the peak temperature was reached to 2571.7 K (2298.6 °C) at the end of final scanning track, as shown in Fig. 37f. Fig. 37g further demonstrates that the highest temperature of the melt pool increased to 2527.4 K (2257.8 °C) at the time of 0.0266 s, as the scanning speed decreases to 750 mm/s (at the same $P = 150$ W). The reason behind this peak temperature is the tremendous energy density provided by the heat source. Furthermore, the highest temperature measured by the thermal imager was about 2891.2 K (2648.5 °C) at a time of 5.36 s.
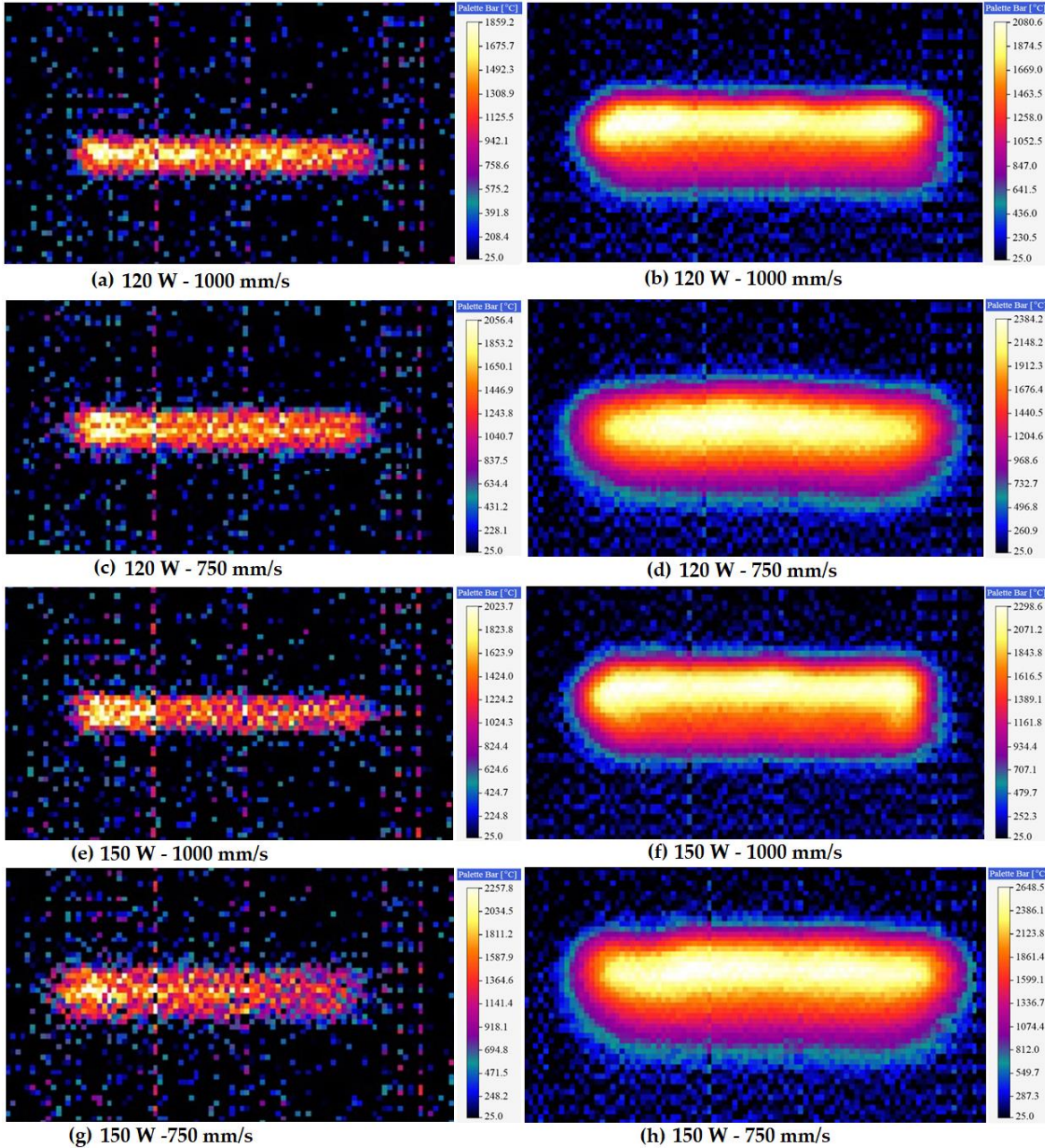
Fig. 37: Typical thermal images for different laser powers and scanning speeds along the scanning direction. (**a**) Temperature gradient at a time of 0.02s for 120 W-1000 mm/s. (**b**) Temperature profiles at a time of 4.02s (after scanning a total of 201 tracks) for 120 W-1000 mm/s. (**c**) Temperature profiles at the time of 0.0266s for 120 W-750 mm/s. (**d**) Temperature profiles at a time of 5.36s (after scanning a total of 201 tracks) for 120 W-750 mm/s. (**e**) Temperature profiles at a time of 0.02s for 150 W-1000 mm/s. (**f**) Temperature profiles at a time of 4.02s (after scanning a total of 201 tracks) for 150 W-

1000 mm/s. (**g**) Temperature profiles at a time of 0.0266s for 150 W-750 mm/s. (**h**) Temperature profiles at a time of 5.36s (after scanning a total of 201 tracks) for 150 W-750 mm/s.

Fig. 38 demonstrates a comparison of the numerically predicted and experimentally measured peak temperature distribution results. The developed numerical model presented a reasonably precise prediction based on a comparison with the experimentally measured peak temperature.
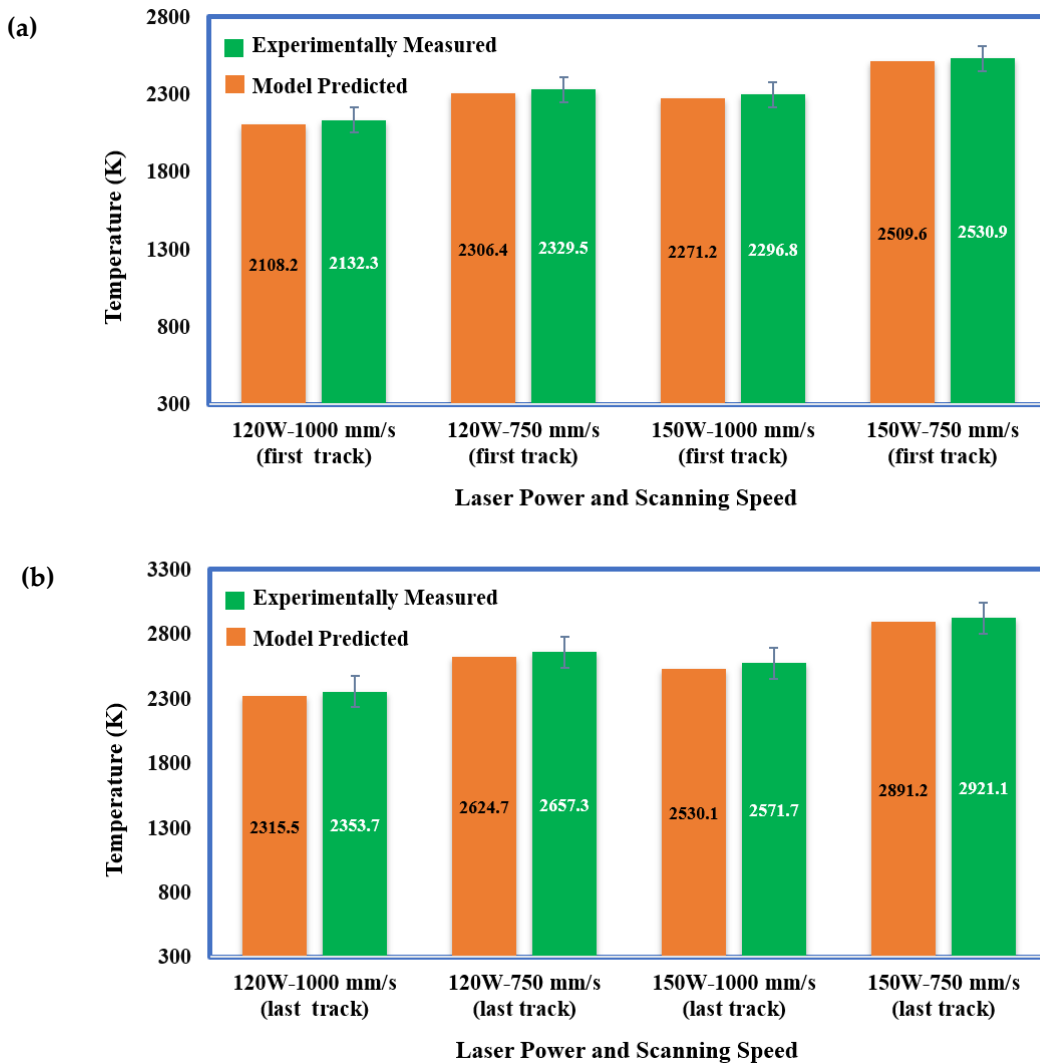
Fig. 38: Comparison of experimental and model-predicted peak temperature distribution results: (**a**) at the ending of the first track and (**b**) at the ending of the final scanning track.

For the temperature measurement, the predicted errors among the simulation and experimental results are in a range of 21–40 K. These errors can occur because of the scattering in the experimental results and probable differences between the thermo-physical properties used for the numerical analysis and real properties in the experiments. Overall, the developed model is appropriate to employ in the thermal modeling and numerical analysis for the SLM process of Ti$_6$Al$_4$V powder.

5.3.4 Temperature Distribution at Multi Layers

Fig. 39 shows how the temperature evolves at P =120 W and u = 1000 mm/s during the building of layers, and the temperature distribution at the end of each layer has been plotted. The temperature increases slightly with the addition of layers from at the second layer approximately 2334.7 K, to 2449.2 K at the last layer. The increasing of laser spot temperature is due to insufficient heat dissipation. Since the previous built layers have higher temperatures, which influence the temperature distribution of the second layers to the final layers. As a result, the temperature of final layer has been increased slightly rather than the first layer. Similar phenomenon has been reported from experimental work by Peyre et al. [88], where the maximum temperature increases with the increasing of printing layers.

By keeping the scanning speed constant and increasing the laser power to 150 W, the maximum temperature during the building of layers has been predicted and plotted in Fig. 40. It has been shown that the peak temperature at the end of second layers approximately 2553.4 K, which has been further raised to approximately 2685.4 K at the end of fifth layers.
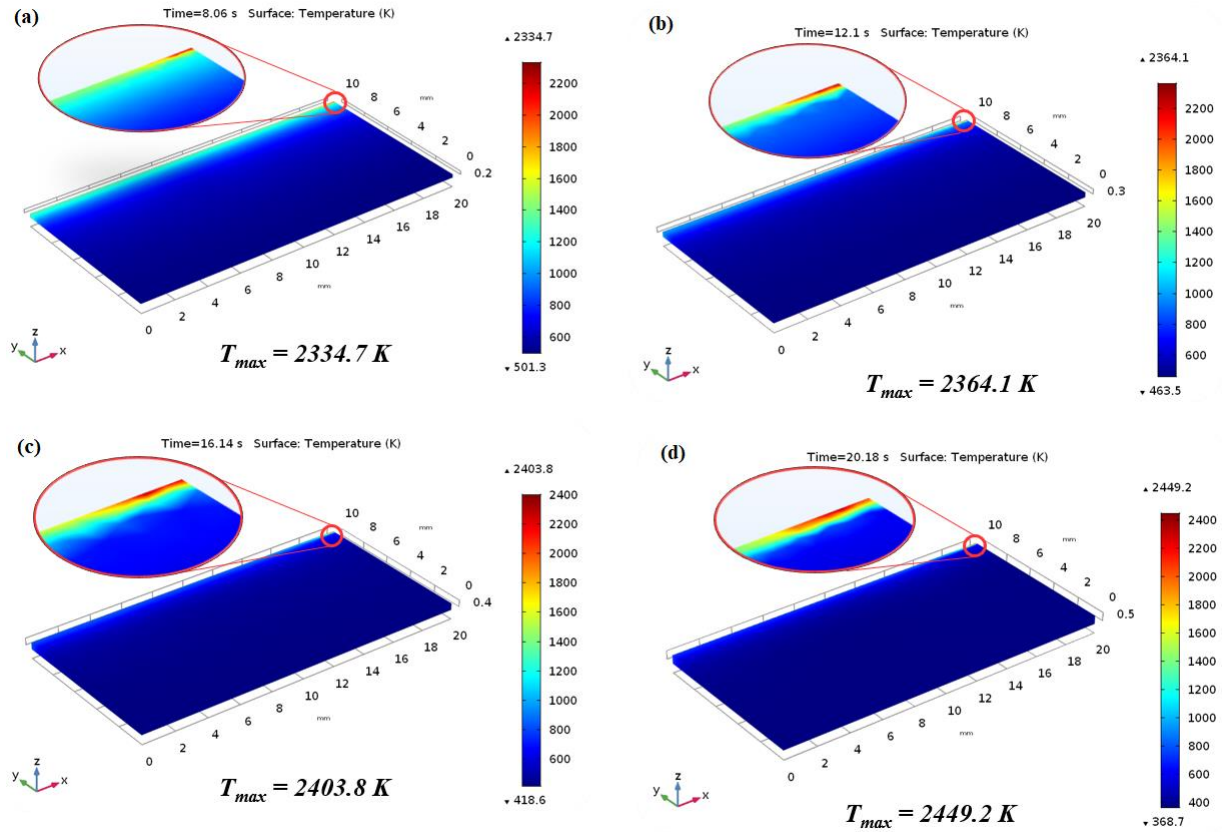
Fig. 39: Temperature profiles throughout the SLM process at P =120 W and u = 1000 mm/s. On the Ti6Al4V powder bed (a) at the ending of the second layers at t = 8.06 s, (b) at the ending of the third layers at t = 12.1 s, (c) at the ending of the forth layers at t = 16.14 s, (d) at the ending of the fifth layers at t = 20.18 s.
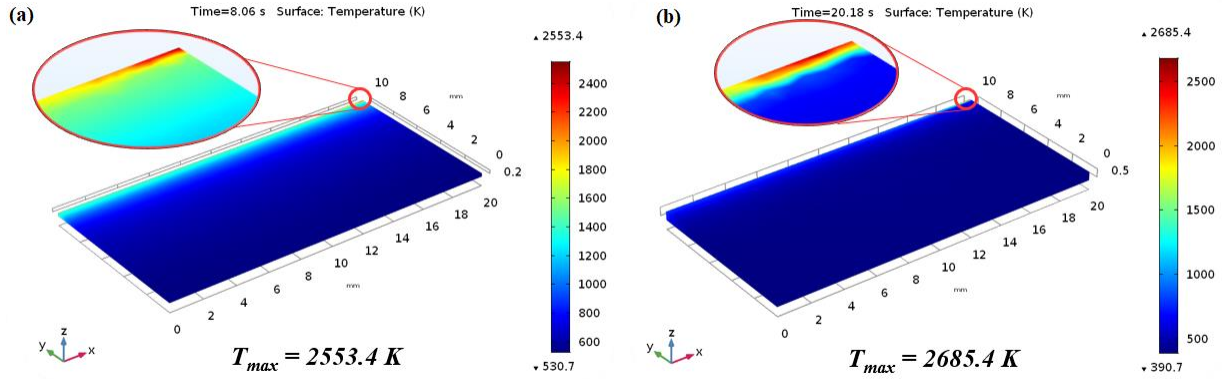
Fig. 40: Temperature profiles throughout the SLM process at P =150 W and u = 1000 mm/s. On the Ti6Al4V powder bed (a) at the ending of the second layers at t = 8.06 s, (b) at the ending of the fifth layers at t = 20.18 s.

Further investigation has been carried out at the constant scanning speed 750 mm/s with different laser power 120 W and 150 W. Due to increasing of laser power the predicted maximum temperature has been increased to 2795.3 K (P =120 W and u = 750 mm/s) and 3078.3 K (P =150 W and u = 750 mm/s) at the end of fifth layer, as presented in Fig. 41a and Fig.41b, respectively. From this investigation, it has been found that laser power has higher impact on increasing the peak temperature rather than the scanning speed.
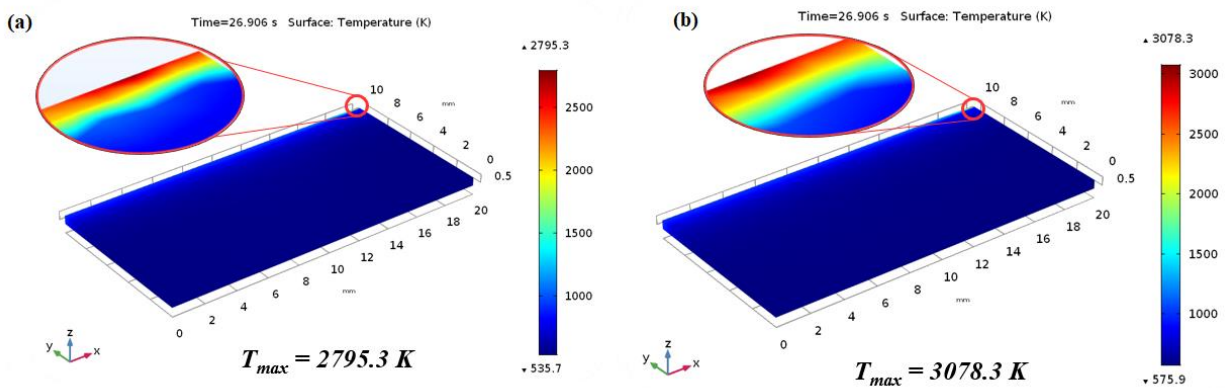
Fig. 41: Temperature profiles throughout the SLM process at the ending of the fifth layers at t = 26.906 s, (a) at P =120 W and u = 750 mm/s, (b) at P =150 W and u = 750 mm/s.

82

5.4 Prediction of Residual Stress and Deformation

In the solid mechanical model, the temperature history is used as thermal boundary condition. Since the surrounding powders have negligible effects on the deformation, the powder elements are omitted in the calculations.

Local uneven heating is the main reason for stress and deformation in the SLM process. Because the rapid scanning speed of laser causes the short interaction between laser and material, the region irradiated by laser undergoes rapid heating, melting, rapid cooling, and solidification. This part of the material is inflated by heat, but the low-temperature region limits the expansion of the material, which leads to thermal stress. In the meantime, the yield limit of the material in the laser area is decreased with the increase of temperature. As a result, the thermal stress of partial region is greater than the yield limit of the material, and the plastic thermal compression deformation occurs. Under the constraint by cooling in surrounding area, residual stress occurs. Fig. 42 shows the residual stress distribution at laser power 150W and scanning speed 750 mm/s as the layers are built up. In our study, the maximum von Mises stress keeps increasing during the scan of each layer and the von Mises stresses at the end of each layer are considered as the maximum. As shown in Fig. 42a, after first layer is printed, the interface shows small stresses with a value of 450.51 MPa. With the addition of layer 2, thermal stress suddenly increases and reaches to 542 MPa as shown in Fig. 42b. With further addition of layer 3, the stress at interface raises to about 658.61 MPa (Fig. 42c). Furthermore, with the addition of fifth layer, the maximum residual stresses rapidly increase to 981.23 MPa (Fig. 42d).

Fig. 43 presents the residual stress distribution at laser power 120W and scanning speed 750 mm/s as the layers are built up on the powder bed successively. As illustrated in Fig. 43a, after

first layer was printed, the predicted maximum residual stresses with a value of 417.52 MPa, which further increased to 952.24 MPa after printed the fifth layer, as shown in Fig. 43b.
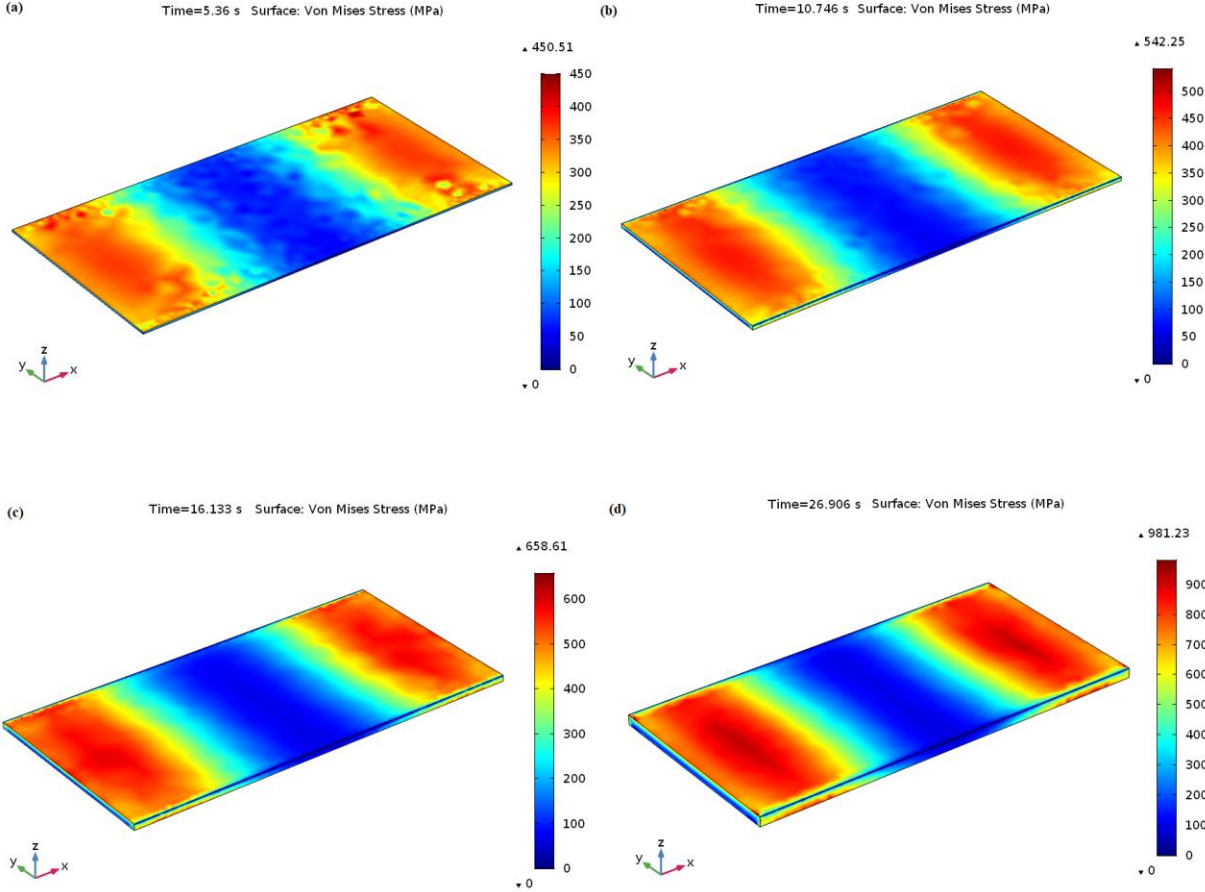
Fig. 42: Maximum von Mises stress at laser power 150W and scanning speed 750 mm/s (a) at the end of first layer (b) at the end of second layer (c) at the end of third layer (d) at the end of fifth layer.
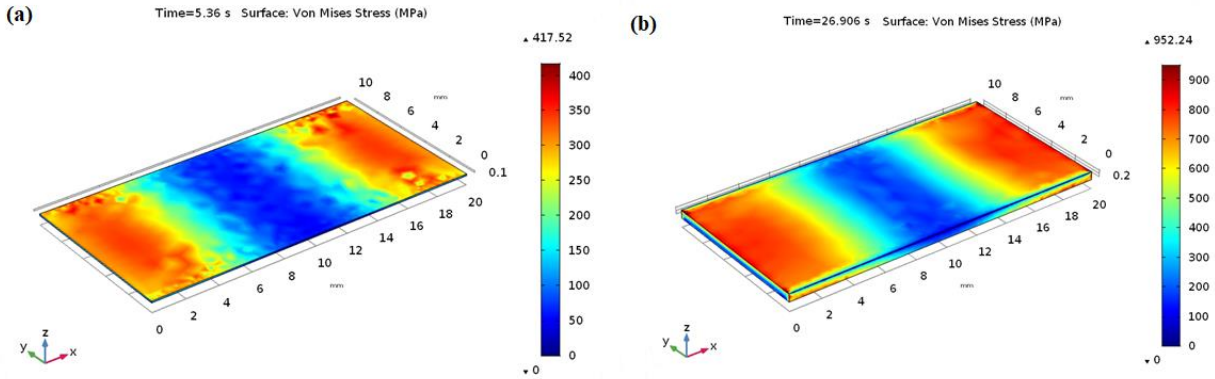
Fig. 43: Maximum von Mises stress at laser power 120W and scanning speed 750 mm/s (a) at the end of first layer (b) at the end of fifth layer.

By using different laser power 120 W and 150 W at constant scanning speed 750 mm/s, the developed residual stress on the printed part has been predicted and presented in Fig. 44. As presented in Fig. 44a, the the development of residual stress on the fabricated parts at the end of fifth layer was 894.35 MPa (P = 120W, u = 750 mm/s). The predicted residual stress on the manufactured part at the end of fifth layer was 935.72 MPa (P = 150W, u = 750 mm/s), as shown in Fig. 44b.

From the investigation, it has been found that the developed of residual stress on the fabricated parts are gradually increased with the successively adding product layers.
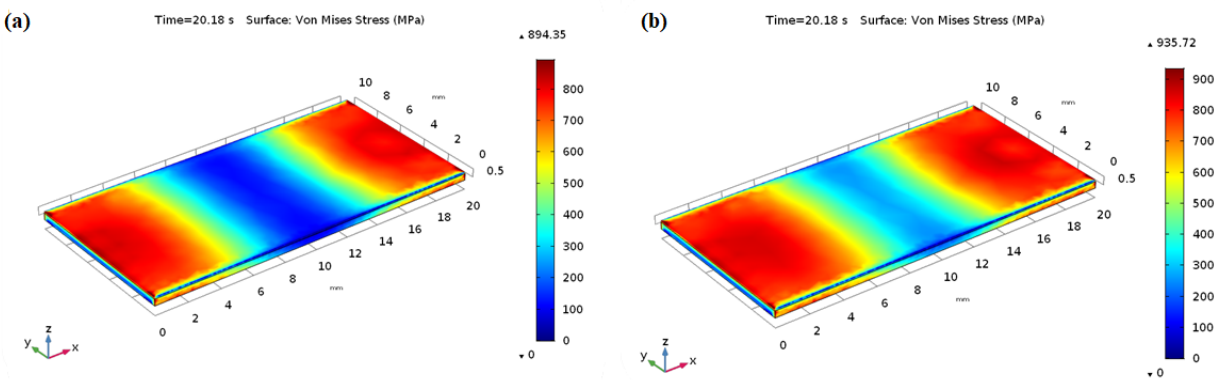
Fig. 44: Maximum von Mises stress at the end of fifth layer (a) at P = 120W, u = 750 mm/s (b) at P = 150W, u = 750 mm/s.

The predicted distortion in printed component for different laser power and scanning speed has been presented in Fig. 45, Fig. 46, and Fig. 47, respectively. At laser power 120 W and scanning speed 1000 mm/s, the predicted top four corner deformation from the numerical investigate was 205.2 µm, 213.4 µm, 263.5 µm, 233.6 µm, as presented in Fig. 45.
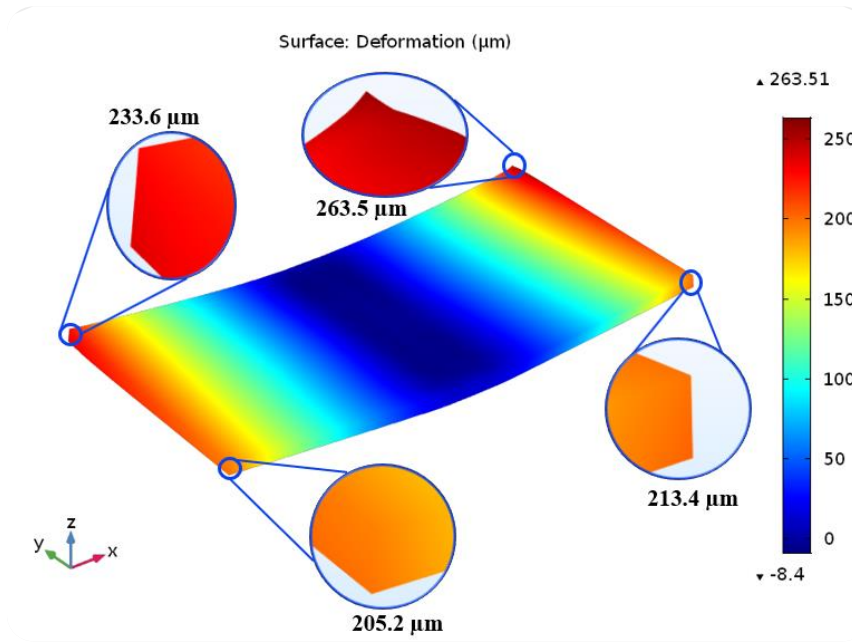
Fig. 45: Predicted deformation results for laser power 120 W and 1000 mm/s.
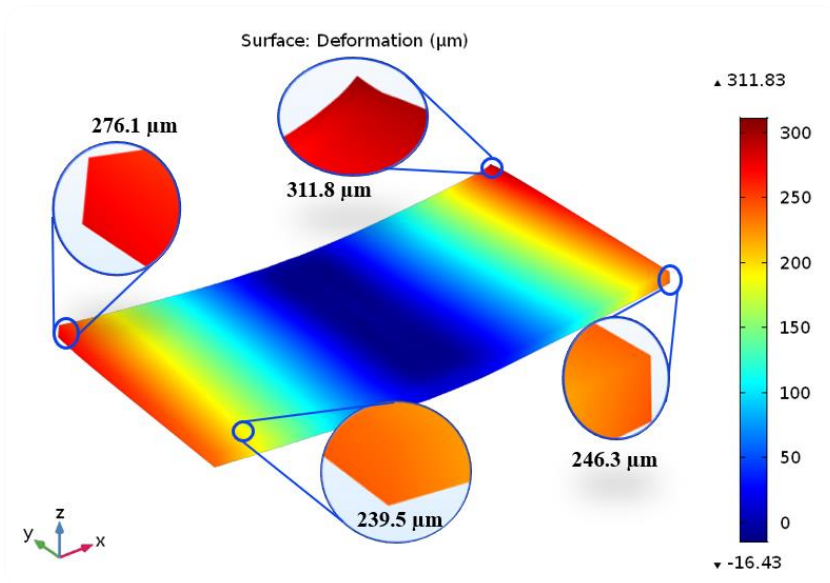
Fig. 46: Predicted deformation results for laser power 120 W and 750 mm/s
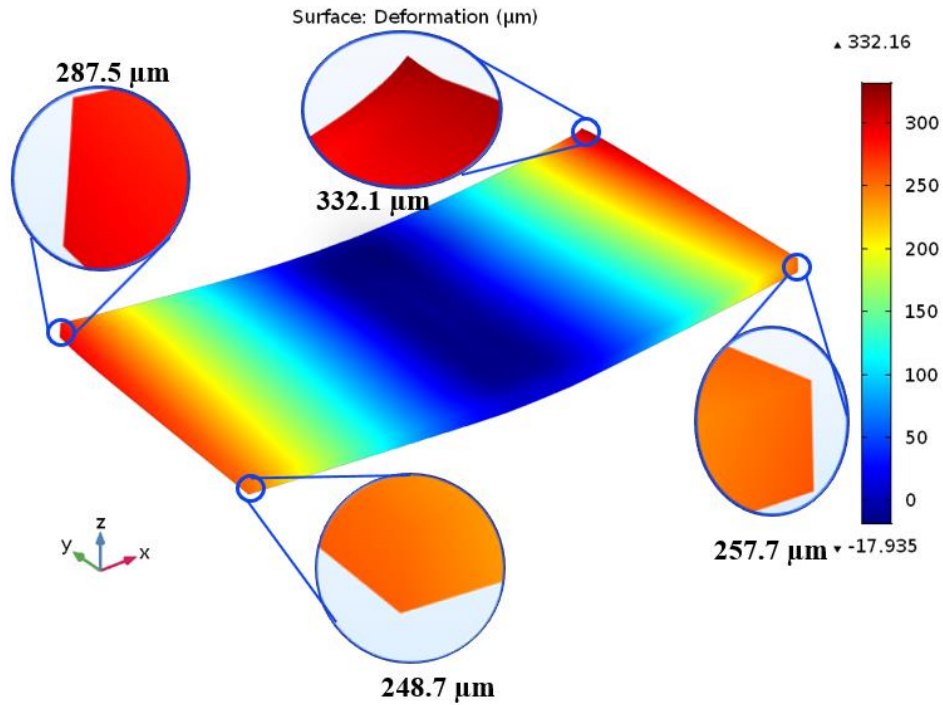
Fig. 47: Predicted deformation results for laser power 150 W and 750 mm/s.

By keeping the same laser power 120 W and decreasing the scanning speed to 750 mm/s, the predicted top four corner deformation has been increased to 239.5 µm, 246.3 µm, 311.8 µm, 276.1 µm, as illustrated in Fig. 46.

Fig. 47 presented the top four corner deformation behavior of numerical at laser power 150 W and scanning speed 750 mm/s and the predicted results was 248.7 µm, 257.7 µm, 332.1 µm, 287.5 µm. In order to validate the numerical investigation, experimental investigation has been carried out. Fig 48 (b) presented the experimental 3D printed part to measure the deformation of top four corner. Table 5 has been presented to show the comparison of predicted deformation results and experimental results. The overall shape distortion comparison shows a good agreement. As shown in Fig. 48b, the distortion is measured at the bottom right of the support material.
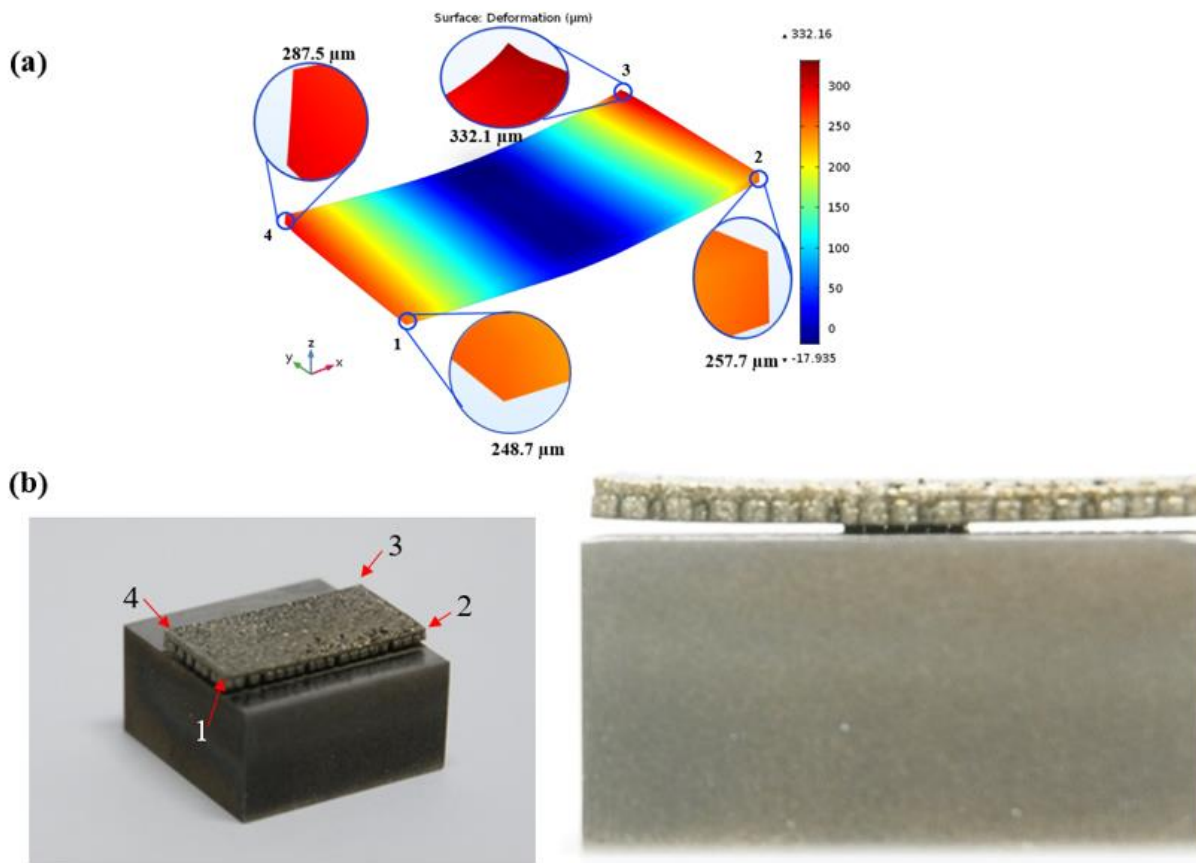
Fig. 48: Top four corner (a) predicted deformation results (b) experimental deformation

behavior.

The predicted top four corner deformation from the model are 248.7, 257.7, 332.1, 287.5 µm, which is in good agreement with the experimental measurement with the highest 74.2 µm deviation. The difference between the prediction and experiment can be attributed to model simplification, including deformation relaxation in the experiment.

Table 5: Comparison of simulation predicted distortion with experimental result.

Point	Simulation result(μm)	Experimental result(μm)	Deviation(μm) (*)
1	248.7	197.2	51.5
2	257.7	201.6	56.1
3	332.1	257.9	74.2
4	287.5	218.7	68.8

From the investigation, it has been proved that the developed can predict the deformation behavior of 3D printed part with reasonable accuracy level.

Chapter 6

Conclusion and Future Work Direction

6.1 Conclusions

In this study, a 3D FE model was established to evaluate and predict the temperature distribution, the melt pool size, residual stress, and deformation during the SLM process. Furthermore, a thermal imager was used to determine the temperature gradients of the Ti_6Al_4V material employing the same process parameters as those used in the numerical investigation. The major conclusions of this study can be summarized as follows:

1. The thermal imager was able to capture the temperature profiles at various laser powers and scanning speeds under the same camera setting, e.g., emissivity = 0.35 and transmission rate = 1.0. Besides, the developed model correctly determined the temperature distribution along the laser scanning direction with good correlation to the experimentally measured temperature for both the single-track and multi-track scanning. The predicting error of the established model is in the range of 21–40 K.

2. At a laser power of 150 W, the predicted melt pool width and depth were approximately 130.9 μm and 68.1 μm, respectively for the 750 mm/s scanning speed; while the length and width would be 114.6 μm and 53.1 μm, respectively for a scanning speed of 1000 mm/s. The developed model can predict the melt pool width (with 2–5% error) and melt pool depth (with 5–6% error).

3. Therefore, the presented fluid flow model that includes the heat flow behavior among the melt pool owing to Marangoni convection is an effective technique for modeling theTi_6Al_4V

powder melting behavior. Furthermore, the peak temperature, and the length, width, depth of the melt pool all rises as the laser power rises and the scanning speed decreases.

4. The calculation of peak temperature and melt pool size for the single-track depositions would be an important method for exploring the optimal process parameters for the SLM process. From the above investigation, SLM process parameters with the sets of 150 W-750 mm/s result in enough temperature to melt the powder, provide a well-defined melt pool size and create a uniform single track. Therefore, this set of process parameters would be suggested for manufacturing 3D printed parts by using the SLM process for the Ti6Al4V alloy.

5. In case of multi-track temperature distribution at laser power 120W and 1000 mm/s, the maximum temperature increases slightly with the addition of layers from at the first layer 2315.5 K, to 2449.2 K at the last layer. The maximum temperature has been predicted by varying the laser power and scanning speed where the predicted temperature at the end of fifth layers was 2685.4 K (P =150 W and u = 1000 mm/s), 2795.3 K (P =120 W and u = 750 mm/s), and 3078.3 K (P =150 W and u = 750 mm/s).

6. At laser power 150W and scanning speed 750 mm/s, the predicted maximum residual stress at the end of first layer was 450.51 MPa, with the addition of fifth layer, the maximum residual stresses rapidly increase to 981.23 MPa.

7. The predicted top four corner deformation from the model are 248.7, 257.7, 332.1, 287.5 µm, which is in good agreement with the experimental measurement with the highest 74.2 µm deviation.

In summary, it is suggested that the developed thermo-mechanical analyses are provided a significant increase in the ability to predict the temperature distribution, residual stress and distortion generated in real parts produced by selective laser melting.

6.2 Future work direction

All studies performed using the thermo-mechanical model were limited to single layer, by the adaptive mesh refinement scheme chosen developed, as discussed in section 2.5. The ability to investigate the process across multiple layers, including the intra-layer interactions of temperature and residual stress is still challenging. In future, this could be achieved by storing the previous state variable, stress fields and plastic strain fields for a scanned layer, and then incorporating these into a subsequent analysis.

Other methods for improving simulation throughput such as the use of global local analysis, super elements and background meshes could be explored, to extend the method across multiple layers.

Applying the multi-scale methodology to more complex geometries, encountered in AM, remains a challenge. Further work is needed to provide a satisfactory method for mapping between the laser scan geometry and the meso-scale regions, which do not rely on the bounding box approach implement. This should account for a library of meso-scale cases, to better represent the overall layer geometry. Additionally, the 3D test cases used were simple geometries, and complex geometries will result in overhang and supported regions being present requiring attention. Further work is needed to incorporate the findings from thermo-mechanical studies on the effect of support material and modelling more complex geometries in 3D models.

6.3 Publications

1. **Md Jonaet Ansari**, Dinh-Son Nguyen, and Hong Seok Park, " Investigation of SLM Process in Terms of Temperature Distribution and Melting Pool Size: Modeling and Experimental Approaches" Materials 2019, 12(8), 1272; DOI: 10.3390/ma12081272.

2. Hong Seok Park, **Md Jonaet Ansari**, "Numerical investigation and an effective predicting system on the Selective Laser Melting (SLM) process with Ti6Al4V alloy", IOP Conf. Ser.: Mater. Sci. Eng.400 042046, DOI: 10.1088/1757-899X/400/4/042046.

3. Hong Seok Park, Ngoc-Hien Tran, **Ansari Md Jonaet**, "Prediction of Temperature Distribution and Residual Stress in SLM Printed Parts", Proceedings of the ASME 2018 13th International Manufacturing Science and Engineering Conference MSEC2018, DOI: 10.1115/MSEC2018-6440.

References

1. Levy, G.N.; Schindel, R.; Kruth, J.P. RAPID MANUFACTURING AND RAPID TOOLING WITH LAYER MANUFACTURING (LM) TECHNOLOGIES, STATE OF THE ART AND FUTURE PERSPECTIVES. *CIRP Ann. - Manuf. Technol.* **2003**, *52*, 589–609.
2. Masoomi, M.; Thompson, S.M.; Shamsaei, N. Laser powder bed fusion of Ti-6Al-4V parts: Thermal modeling and mechanical implications. *Int. J. Mach. Tools Manuf.* **2017**, *118–119*, 73–90.
3. Dilip, J.J.S.; Zhang, S.; Teng, C.; Zeng, K.; Robinson, C.; Pal, D.; Stucker, B. Influence of processing parameters on the evolution of melt pool, porosity, and microstructures in Ti-6Al-4V alloy parts fabricated by selective laser melting. *Prog. Addit. Manuf.* **2017**, *2*, 157–167.
4. Song, B.; Dong, S.; Liao, H.; Coddet, C. Process parameter selection for selective laser melting of Ti6Al4V based on temperature distribution simulation and experimental sintering. *Int. J. Adv. Manuf. Technol.* **2012**, *61*, 967–974.
5. Li, Z.; Li, B.-Q.; Bai, P.; Liu, B.; Wang, Y. Research on the Thermal Behaviour of a Selectively Laser Melted Aluminium Alloy: Simulation and Experiment. *Materials* **2018**, *11*, 1172.
6. Li, R.; Shi, Y.; Wang, Z.; Wang, L.; Liu, J.; Jiang, W. Densification behavior of gas and water atomized 316L stainless steel powder during selective laser melting. *Appl. Surf. Sci.* **2010**, *256*, 4350–4356.
7. Bertrand, P.; Yadroitsev, I.; Yadroitsava, I.; Smurov, I. Factor analysis of selective laser melting process parameters and geometrical characteristics of synthesized single tracks. *Rapid Prototyp. J.* **2012**, *18*, 201–208.
8. Huang, Y.; Yang, L.J.; Du, X.Z.; Yang, Y.P. Finite element analysis of thermal behavior of metal powder during selective laser melting. *Int. J. Therm. Sci.* **2016**, *C*, 146–157.
9. Hussein, A.; Hao, L.; Yan, C.; Everson, R. Finite element simulation of the temperature and stress fields in single layers built without-support in selective laser melting. *Mater. Des. 1980-2015* **2013**, *52*, 638–647.
10. Beaman, J.J.; Barlow, J.W.; Bourell, D.L.; Crawford, R.H.; Marcus, H.L.; McAlea, K.P. *Solid Freeform Fabrication: A New Direction in Manufacturing*; Springer US: Boston, MA, 1997; ISBN 978-0-7923-9834-9.
11. Lü, L.; Fuh, J.Y.H.; Wong, Y.S. *Laser-induced materials and processes for rapid prototyping*; Kluwer Academic Publishers: Boston, 2001; ISBN 978-0-7923-7400-8.
12. Hague *, R.; Mansour, S.; Saleh, N. Material and design considerations for rapid manufacturing. *Int. J. Prod. Res.* **2004**, *42*, 4691–4708.
13. Burns, M. *Automated fabrication: improving productivity in manufacturing*; PTR Prentice Hall: Englewood Cliffs, N.J, 1993; ISBN 978-0-13-119462-5.
14. Bjørke, Ø. How to Make Stereolithography into a Practical Tool for Tool Production. *CIRP Ann.* **1991**, *40*, 175–177.
15. Ro\vsker, P.; Shellabear, M. E-manufacturing with laser-sintering - to series production and beyond.; 2004.
16. Kruth, J.-P.; Leu, M.C.; Nakagawa, T. Progress in Additive Manufacturing and Rapid Prototyping. *CIRP Ann.* **1998**, *47*, 525–540.
17. Wohlers Associates *Wohlers report 2019: 3D printing and additive manufacturing state of the industry*; 2019; ISBN 978-0-9913332-5-7.

18. *Rapid manufacturing: an industrial revolution for the digital age*; Hopkinson, N., Hague, R.J.M., Dickens, P.M., Eds.; John Wiley: Chichester, England, 2006; ISBN 978-0-470-01613-8.
19. Gebhardt, A. *Rapid Prototyping*; Carl Hanser Verlag GmbH & Co. KG: München, 2003; ISBN 978-3-446-21259-6.
20. Hu, Y.; Fadel, G.M.; Blouin, V.Y.; White, D.R. Optimal design for additive manufacturing of heterogeneous objects using ultrasonic consolidation. *Virtual Phys. Prototyp.* **2006**, *1*, 53–62.
21. Kong, C.Y.; Soar, R.C.; Dickens, P.M. Optimum process parameters for ultrasonic consolidation of 3003 aluminium. *J. Mater. Process. Technol.* **2004**, *146*, 181–187.
22. Griffith, M.L.; Schlienger, M.E.; Harwell, L.D.; Oliver, M.S.; Baldwin, M.D.; Ensz, M.T.; Essien, M.; Brooks, J.; Robino, C.V.; Smugeresky, J.E.; et al. Understanding thermal behavior in the LENS process. *Mater. Des.* **1999**, *20*, 107–113.
23. Griffith, M.L.; Ensz, M.T.; Puskar, J.D.; Robino, C.V.; Brooks, J.A.; Philliber, J.A.; Smugeresky, J.E.; Hofmeister, W.H. Understanding the Microstructure and Properties of Components Fabricated by Laser Engineered Net Shaping (LENS). *MRS Proc.* **2000**, *625*, 9.
24. Sexton, L.; Lavin, S.; Byrne, G.; Kennedy, A. Laser cladding of aerospace materials. *J. Mater. Process. Technol.* **2002**, *122*, 63–68.
25. Deckard, C.; Beaman, J.J. Process and control issues in selective laser sintering.; 1988.
26. Tolochko, N.; Mozzharov, S.; Laoui, T.; Froyen, L. Selective laser sintering of single- and two-component metal powders. *Rapid Prototyp. J.* **2003**, *9*, 68–78.
27. Murr, L.E.; Gaytan, S.M.; Ramirez, D.A.; Martinez, E.; Hernandez, J.; Amato, K.N.; Shindo, P.W.; Medina, F.R.; Wicker, R.B. Metal Fabrication by Additive Manufacturing Using Laser and Electron Beam Melting Technologies. *J. Mater. Sci. Technol.* **2012**, *28*, 1–14.
28. Hauser, C.; Childs, T.H.C.; Dalgarno, K.W.; Eane, R.B. Atmospheric Control during Direct Selective Laser Sintering of Stainless Steel 314S Powder.; 1999.
29. Kruth, J.-P.; Levy, G.; Klocke, F.; al, et Consolidation phenomena in laser and powder-bed based layered manufacturing. In Proceedings of the 57th General assembly of CIRP; 2007; pp. 730–759.
30. Thijs, L.; Van Humbeeck, J.; Kempen, K.; Yasa, E.; Kruth, J.-P.; Rombouts, M. Investigation on the inclusions in maraging steel produced by selective laser melting. In Proceedings of the Innovative Developments in Virtual and Physical Prototyping; CRC Press/Balkema; POBox 447 AK Leiden, The Netherlands, 20120101; pp. 297–304.
31. Jhabvala, J.; Boillat, E.; Antignac, T.; Glardon, R. On the effect of scanning strategies in the selective laser melting process. *Virtual Phys. Prototyp.* **2010**, *5*, 99–109.
32. Ansari, M.J.; Nguyen, D.-S.; Park, H.S. Investigation of SLM Process in Terms of Temperature Distribution and Melting Pool Size: Modeling and Experimental Approaches. *Materials* **2019**, *12*, 1272.
33. Park, H.-S.; Tran, N.-H.; Jonaet, A.M. Prediction of Temperature Distribution and Residual Stress in SLM Printed Parts. In Proceedings of the Volume 1: Additive Manufacturing; Bio and Sustainable Manufacturing; American Society of Mechanical Engineers: College Station, Texas, USA, 2018; p. V001T01A036.
34. Kurzynowski, T.; Chlebus, E.; Kuźnicka, B.; Reiner, J. Parameters in selective laser melting for processing metallic powders.; Beyer, E., Morris, T., Eds.; San Francisco, California, USA, 2012; p. 823914.

35. Agarwala, M.; Bourell, D.; Beaman, J.; Marcus, H.; Barlow, J. Direct selective laser sintering of metals. *Rapid Prototyp. J.* **1995**, *1*, 26–36.

36. Guo, N.; Leu, M.C. Additive manufacturing: technology, applications and research needs. *Front. Mech. Eng.* **2013**, *8*, 215–243.

37. Zhu, H.H.; Fuh, J.Y.H.; Lu, L. The influence of powder apparent density on the density in direct laser-sintered metallic parts. *Int. J. Mach. Tools Manuf.* **2007**, *47*, 294–298.

38. Mazumder, J.; Dutta, D.; Kikuchi, N.; Ghosh, A. Closed loop direct metal deposition: art to part. *Opt. Lasers Eng.* **2000**, *34*, 397–414.

39. Tolochko, N.K.; Khlopkov, Y.V.; Mozzharov, S.E.; Ignatiev, M.B.; Laoui, T.; Titov, V.I. Absorptance of powder materials suitable for laser sintering. *Rapid Prototyp. J.* **2000**, *6*, 155–161.

40. Gusarov, A.V.; Smurov, I. Modeling the interaction of laser radiation with powder bed at selective laser melting. *Phys. Procedia* **2010**, *5*, 381–394.

41. Wang, X.C.; Laoui, T.; Bonse, J.; Kruth, J.P.; Lauwers, B.; Froyen, L. Direct Selective Laser Sintering of Hard Metal Powders: Experimental Study and Simulation. *Int. J. Adv. Manuf. Technol.* **2002**, *19*, 351–357.

42. Yadroitsev, I.; Gusarov, A.; Yadroitsava, I.; Smurov, I. Single track formation in selective laser melting of metal powders. *J. Mater. Process. Technol.* **2010**, *210*, 1624–1631.

43. Gusarov, A.V.; Kovalev, E.P. Model of thermal conductivity in powder beds. *Phys. Rev. B* **2009**, *80*, 024202.

44. Tolochko, N.K.; Mozzharov, S.E.; Yadroitsev, I.A.; Laoui, T.; Froyen, L.; Titov, V.I.; Ignatiev, M.B. Balling processes during selective laser treatment of powders. *Rapid Prototyp. J.* **2004**, *10*, 78–87.

45. Zhao, C.X.; Kwakernaak, C.; Pan, Y.; Richardson, I.M.; Saldi, Z.; Kenjeres, S.; Kleijn, C.R. The effect of oxygen on transitional Marangoni flow in laser spot welding. *Acta Mater.* **2010**, *58*, 6345–6357.

46. Rai, R.; Elmer, J.W.; Palmer, T.A.; DebRoy, T. Heat transfer and fluid flow during keyhole mode laser welding of tantalum, Ti–6Al–4V, 304L stainless steel and vanadium. *J. Phys. Appl. Phys.* **2007**, *40*, 5753–5766.

47. Qiu, C.; Panwisawas, C.; Ward, M.; Basoalto, H.C.; Brooks, J.W.; Attallah, M.M. On the role of melt flow into the surface structure and porosity development during selective laser melting. *Acta Mater.* **2015**, *96*, 72–79.

48. Simonelli, M.; Tuck, C.; Aboulkhair, N.T.; Maskery, I.; Ashcroft, I.; Wildman, R.D.; Hague, R. A Study on the Laser Spatter and the Oxidation Reactions During Selective Laser Melting of 316L Stainless Steel, Al-Si10-Mg, and Ti-6Al-4V. *Metall. Mater. Trans. A* **2015**, *46*, 3842–3851.

49. Aboulkhair, N.T.; Everitt, N.M.; Ashcroft, I.; Tuck, C. Reducing porosity in AlSi10Mg parts processed by selective laser melting. *Addit. Manuf.* **2014**, *1–4*, 77–86.

50. Yadroitsev, I.; Smurov, I. Selective laser melting technology: From the single laser melted track stability to 3D parts of complex shape. *Phys. Procedia* **2010**, *5*, 551–560.

51. Tsopanos, S.; Mines, R.A.W.; McKown, S.; Shen, Y.; Cantwell, W.J.; Brooks, W.; Sutcliffe, C.J. The Influence of Processing Parameters on the Mechanical Properties of Selectively Laser Melted Stainless Steel Microlattice Structures. *J. Manuf. Sci. Eng.* **2010**, *132*, 041011.

52. Wang, D.; Yang, Y.; Yi, Z.; Su, X. Research on the fabricating quality optimization of the overhanging surface in SLM process. *Int. J. Adv. Manuf. Technol.* **2013**, *65*, 1471–1484.

53. Zhang Jian; Li Deying; Zhao Longzhi; Zhao Mingjuan Simulation of temperature field in selective laser sintering of copper powder. In Proceedings of the 2010 International Conference on Mechanic Automation and Control Engineering; IEEE: Wuhan, China, 2010; pp. 3282–3285.
54. Gusarov, A.V.; Yadroitsev, I.; Bertrand, Ph.; Smurov, I. Heat transfer modelling and stability analysis of selective laser melting. *Appl. Surf. Sci.* **2007**, *254*, 975–979.
55. King, W.; Anderson, A.T.; Ferencz, R.M.; Hodge, N.E.; Kamath, C.; Khairallah, S.A. Overview of modelling and simulation of metal powder bed fusion process at Lawrence Livermore National Laboratory. *Mater. Sci. Technol.* **2015**, *31*, 957–968.
56. Yadroitsev, I.; Krakhmalev, P.; Yadroitsava, I. Selective laser melting of Ti6Al4V alloy for biomedical applications: Temperature monitoring and microstructural evolution. *J. Alloys Compd.* **2014**, *583*, 404–409.
57. Li, X.P.; Kang, C.W.; Huang, H.; Sercombe, T.B. The role of a low-energy–density re-scan in fabricating crack-free Al85Ni5Y6Co2Fe2 bulk metallic glass composites via selective laser melting. *Mater. Des.* **2014**, *63*, 407–411.
58. Li, Y.; Gu, D. Parametric analysis of thermal behavior during selective laser melting additive manufacturing of aluminum alloy powder. *Mater. Des.* **2014**, *63*, 856–867.
59. Fu, C.H.; Guo, Y.B. Three-Dimensional Temperature Gradient Mechanism in Selective Laser Melting of Ti-6Al-4V. *J. Manuf. Sci. Eng.* **2014**, *136*.
60. Loh, L.-E.; Chua, C.-K.; Yeong, W.-Y.; Song, J.; Mapar, M.; Sing, S.-L.; Liu, Z.-H.; Zhang, D.-Q. Numerical investigation and an effective modelling on the Selective Laser Melting (SLM) process with aluminium alloy 6061. *Int. J. Heat Mass Transf.* **2015**, *80*, 288–300.
61. Brückner, F.; Lepski, D.; Beyer, E. Modeling the Influence of Process Parameters and Additional Heat Sources on Residual Stresses in Laser Cladding. *J. Therm. Spray Technol.* **2007**, *16*, 355–373.
62. Buchbinder, D.; Meiners, W.; Pirch, N.; Wissenbach, K.; Schrage, J. Investigation on reducing distortion by preheating during manufacture of aluminum components using selective laser melting. *J. Laser Appl.* **2013**, *26*, 012004.
63. Vasinonta, A.; Beuth, J.L.; Griffith, M. Process Maps for Predicting Residual Stress and Melt Pool Size in the Laser-Based Fabrication of Thin-Walled Structures. *J. Manuf. Sci. Eng.* **2007**, *129*, 101–109.
64. Manvatkar, V.; De, A.; DebRoy, T. Spatial variation of melt pool geometry, peak temperature and solidification parameters during laser assisted additive manufacturing process. *Mater. Sci. Technol.* **2015**, *31*, 924–930.
65. Wu, A.S.; Brown, D.W.; Kumar, M.; Gallegos, G.; King, W.E. An Experimental Investigation into Additive Manufacturing Induced Residual Stresses in 316L Stainless Steel. *Metall. Mater. Trans. Vol 45 No 13 Sept. 16 2014 Pp 6260-6270* **2014**.
66. Alimardani, M.; Toyserkani, E.; Huissoon, J.P.; Paul, C.P. On the delamination and crack formation in a thin wall fabricated using laser solid freeform fabrication process: An experimental–numerical investigation. *Opt. Lasers Eng.* **2009**, *47*, 1160–1168.
67. Pohl, H.; Simchi, A.; Issa, M.; Dias, H.C. Thermal Stresses in Direct Metal Laser Sintering. 7.
68. Kruth, J.-P.; Deckers, J.; Yasa, E.; Wauthlé, R. Assessing and comparing influencing factors of residual stresses in selective laser melting using a novel analysis method. *Proc. Inst. Mech. Eng. Part B J. Eng. Manuf.* **2012**, *226*, 980–991.

69. van Belle, L.; Vansteenkiste, G.; Boyer, J.C. Investigation of Residual Stresses Induced during the Selective Laser Melting Process Available online: https://www.scientific.net/KEM.554-557.1828 (accessed on Nov 1, 2019).

70. Zaeh, M.F.; Branner, G. Investigations on residual stresses and deformations in selective laser melting. *Prod. Eng.* **2010**, *4*, 35–45.

71. Vrancken, B. Study of Residual Stresses in Selective Laser Melting. 300.

72. Shuai, C.; Feng, P.; Gao, C.; Zhou, Y.; Peng, S. Simulation of dynamic temperature field during selective laser sintering of ceramic powder. *Math. Comput. Model. Dyn. Syst.* **2013**, *19*, 1–11.

73. Fischer, P.; Locher, M.; Romano, V.; Weber, H.P.; Kolossov, S.; Glardon, R. Temperature measurements during selective laser sintering of titanium powder. *Int. J. Mach. Tools Manuf.* **2004**, *12–13*, 1293–1296.

74. Dai, K.; Shaw, L. Finite element analysis of the effect of volume shrinkage during laser densification. *Acta Mater.* **2005**, *53*, 4743–4754.

75. Ali, H.; Ghadbeigi, H.; Mumtaz, K. Residual stress development in selective laser-melted Ti6Al4V: a parametric thermal modelling approach. *Int. J. Adv. Manuf. Technol.* **2018**, *97*, 2621–2633.

76. Li, Z.; Xu, R.; Zhang, Z.; Kucukkoc, I. The influence of scan length on fabricating thin-walled components in selective laser melting. *Int. J. Mach. Tools Manuf.* **2018**, *126*, 1–12.

77. Parry, L.; Ashcroft, I.A.; Wildman, R.D. Understanding the effect of laser scan strategy on residual stress in selective laser melting through thermo-mechanical simulation. *Addit. Manuf.* **2016**, *12*, 1–15.

78. Bugeda Miguel Cervera, G.; Lombera, G. Numerical prediction of temperature and density distributions in selective laser sintering processes. *Rapid Prototyp. J.* **1999**, *5*, 21–26.

79. Denlinger, E.R.; Heigel, J.C.; Michaleris, P. Residual stress and distortion modeling of electron beam direct manufacturing Ti-6Al-4V. *Proc. Inst. Mech. Eng. Part B J. Eng. Manuf.* **2015**, *229*, 1803–1813.

80. Jiang, W.; Dalgarno, K.W.; Childs, T.H.C. Finite Element Analysis of Residual Stresses and Deformations in Direct Metal SLS Process. 9.

81. Yang, Y.P.; Jamshidinia, M.; Boulware, P.; Kelly, S.M. Prediction of microstructure, residual stress, and deformation in laser powder bed fusion process. *Comput. Mech.* **2018**, *61*, 599–615.

82. Fischer, P.; Romano, V.; Weber, H.P.; Karapatis, N.P.; Boillat, E.; Glardon, R. Sintering of commercially pure titanium powder with a Nd:YAG laser source. *Acta Mater.* **2003**, *51*, 1651–1662.

83. Goldak, J.; Chakravarti, A.; Bibby, M. A new finite element model for welding heat sources. *Metall. Trans. B* **1984**, *15*, 299–305.

84. Gürtler, F.-J.; Karg, M.; Leitz, K.-H.; Schmidt, M. Simulation of Laser Beam Melting of Steel Powders using the Three-Dimensional Volume of Fluid Method. *Phys. Procedia* **2013**, *41*, 881–886.

85. Kundakcıoğlu, E.; Lazoglu, I.; Poyraz, Ö.; Yasa, E.; Cizicioğlu, N. Thermal and molten pool model in selective laser melting process of Inconel 625. *Int. J. Adv. Manuf. Technol.* **2018**, *95*, 3977–3984.

86. Lee, Y.S.; Zhang, W. Modeling of heat transfer, fluid flow and solidification microstructure of nickel-base superalloy fabricated by laser powder bed fusion. *Addit. Manuf.* **2016**, *12*, 178–188.

87. Zhirnov, I.; Yadroitsava, I.; Yadroitsev, I. Optical Monitoring and Numerical Simulation of Temperature Distribution at Selective Laser Melting of Ti6Al4V Alloy Available online: https://www.scientific.net/MSF.828-829.474 (accessed on Nov 2, 2019).

88. Peyre, P.; Aubry, P.; Fabbro, R.; Neveu, R.; Longuet, A. Analytical and numerical modelling of the direct metal deposition laser process. *J. Phys. Appl. Phys.* **2008**, *41*, 025403.